ABSTRACT

Title of Dissertation: The AC Hall Effect in Single Crystal $Bi_2Sr_2CaCu_2O_{8+\delta}$

Donald Cronin Schmadel, Jr., Doctor of Philosophy, 2002

Dissertation directed by: Professor H. Dennis Drew
Department of Physics

A novel heterodyne detection system determines the frequency and temperature dependence of the Hall transport in single crystal, optimally doped $Bi_2Sr_2CaCu_2O_{8+\delta}$. The frequencies measured are in the mid-infrared and correspond to the spectral lines of a CO_2 laser between 900 and 1110 cm^{-1}. The measured temperature range is continuous and extends from 35 to 330K. The sample is an approximately 200 nm thick film peeled from a bulk crystal grown by G. D. Gu of the Department of Physics, Brookhaven National Laboratory, Upton, NY. Infrared conductivity data from measurements performed by J. J. Tu (also of the Department of Physics, Brookhaven National Laboratory) on other bulk crystals from this batch supplied the real and imaginary parts of σ_{xx} which were used in the analysis to isolate the Hall angle, σ_{xy}, R_H.

The experimental system uses a photoelastic modulator (PEM) to phase modulate the y polarization channel of the beam transmitted by the sample. A mercury cadmium telluride optical detector then mixes the modulated polarization of the y channel with the unmodulated polarization of the x channel, forming sidebands, whose amplitudes are proportional to the real and imaginary parts of the Faraday angle. Maxwell's equations and the contributed values of σ_{xx} are used to convert the complex Faraday angle to the Hall angle.

The results for 2212 BSCCO show a significant disconnect from the behavior of the Hall angle in the existing data for YBCO in the far-infrared. The existing far-infrared data indicate a negative value for the real part of the Hall angle above 250 cm^{-1}. That of the current work is positive. The current work when analyzed using an extended Drude formalism results in a Hall frequency and scattering rate almost constant in frequency. The scattering increases linearly with temperature from ~100 cm^{-1} at 100 K to 560 cm^{-1} at 330 K. Sum rules when evaluated using extrapolations of the data do not indicate a significant difference between the *f*-sum, the sum for $\mathrm{Re}(\theta_H)$, and the sum for $\omega\,\mathrm{Im}(\sigma_{xy})$.

THE AC HALL EFFECT IN SINGLE CRYSTAL

$Bi_2Sr_2CaCu_2O_{8+\delta}$

by

Donald Cronin Schmadel, Jr

Dissertation submitted to the Faculty of the Graduate School of the
University of Maryland, College Park in partial fulfillment
of the requirements for the degree of
Doctor of Philosophy
2002

Advisory committee:

Professor H. Dennis Drew, Chairman/Advisor
Professor Christopher C. Davis
Professor Richard L. Greene
Professor Frederick C. Wellstood
Professor Victor Yakovenko

ACKNOWLEDGEMENT

My greatest thanks goes to Professor H. Dennis Drew, my advisor, whose knowledge and ingenuity in Physics along with his divine-like patience funneled my efforts into the completion of this work.

Additionally, I should like to thank

Christopher Homes and G. D. Gu for providing the Bulk Crystal used in the current work

Jiufeng Tu for providing the excellent data for the complex infrared conductivity

Danilo Romero for his expertise in preparing, peeling, and mounting the sample

John Cerne, Mathew Grayson, Laurent Rigal, Greg Jenkins, and Jeff Simpson for their help in the design, construction, and analysis of various aspect of the experimental system

Professor Frederick Wellstood and my brother Kevin Schmadel for their help and patience in correcting the manuscript

and most important Yuri Kubota, my wife, who has stood by my side with encouragement and support.

DEDICATION

To my brother, Kevin Cronin Schmadel,

and

to my father, Donald Cronin Schmadel, Sr.

TABLE OF CONTENTS

LIST OF FIGURES

LIST OF PLATES

1 Introduction

No shippe could saile on Seas,
her course to runne aright,
Nor Compasse shewe the readie waie,
were Magnes not of might.

Robert Norman "The Magnes or Lodestones Challenge"

A new and unique perspective for charge transport in the high temperature superconductors emerges from observations of the Hall effect at the very high frequencies of the optical region. These experiments involve analyzing light transmitted by a thin film of the material while subjected to an intense magnetic field of typically ±8 Tesla. The transmitted beam experiences a complex Faraday rotation. The real part of this rotation corresponds to a simple geometric rotation of the initial polarization vector about the propagation vector. The imaginary part corresponds to the ellipticity of the transmitted beam and results from the preferential absorption of one circular polarization state over the other. Values for the material properties σ_{xy} , θ_H , and R_H follow from an analysis of this complex Faraday angle.

The current work explores these values at mid-infrared frequencies corresponding to the optical frequencies of the lines of a CO_2 laser. The results demonstrate a rather different behavior compared to that indicated by DC and far-infrared Hall experiments. The results of the current work suggest an almost Drude behavior with a relaxation rate linear in temperature. Additionally, they suggest the existence of a broad but strong feature around 30 to 50 meV, a frequency region which lies midway between the far- and mid-infrared measurements. The effort to apprehend the nature of these high temperature superconductors, which has now spanned fifteen years, has produced no theory, model, nor phenomenology that accommodates these results. Therefore, to establish a context for the results of the current work let us next

review the history of the more general matter of charge transport in the high temperature superconductors.

1.1 Background

The history of the high temperature superconductors begins with the oft quoted discovery by Bednorz and Müller [1] of superconductivity at 30 K in polycrystalline samples of $Ba_x La_{5-x} Cu_5 O_{5(3-y)}$ for $x \sim .75$. Recognizing the importance of the bivalence of the copper constituent, the rush was on to find other representatives of these cuprates. By the next year Gurvitch and Fiory [2] in an effort to explore the electron-phonon interaction measured the temperature dependence of the resistivity in the cuprates $La_{2-x} Sr_x CuO_4$ and $YBa_2 Cu_3 O_7$. Like copper, the resistance was linear to very high temperatures. However, the high temperature resistance of ~4 mΩ-cm for the cuprates versus ~5 μΩ-cm for copper was inexplicable. The dilemma involves a, the Cu-O bond length, compared to the very short mean free path ℓ calculated from the resistivity data using an effective-medium model and band theory. Simply put, $\ell \approx 1 - 2$ Å for high temperatures and seems too small compared to the interatomic spacing, $a \approx 2$ Å, to explain a linear temperature dependence which shows no sign of saturation.

The DC resistance data was soon augmented by data from optical spectra, first, by Tajima *et al.* [3] and then by Orenstein *et al.* [4]. Both studies established non-Drude behavior with only a small free carrier contribution to the infrared oscillator strength. These first measurements were on ceramic samples and, therefore, did not admit to a resolution of the conductivity along the a and b crystal axes.

Numerous studies on single crystal samples followed. Among the most relevant to the current work are Quijada [5], Tu *et al.* [6] and the yet unpublished data collected by J. J. Tu on crystals which were grown in the same batch as the sample of the current work. This last mentioned data is used in our analysis and is presented in

Figs. 7 and 8 in section 4.1 below.

Quijada presents optical conductivity results for $La_2CuO_{4+\delta}$, $YBa_2Cu_3O_{7-\delta}$, and $Bi_2Sr_2Ca_1Cu_2O_8$ single crystals separately resolved along the a and b axes. The real part of the conductivity σ_1 for $Bi_2Sr_2Ca_1Cu_2O_8$ reveals very little anisotropy, particularly around 1000 cm^{-1}, the wavelength region of the current work. This is in contrast to $YBa_2Cu_3O_{7-\delta}$, which is complicated by the additive conductivity of the chains shown in Fig. (1).

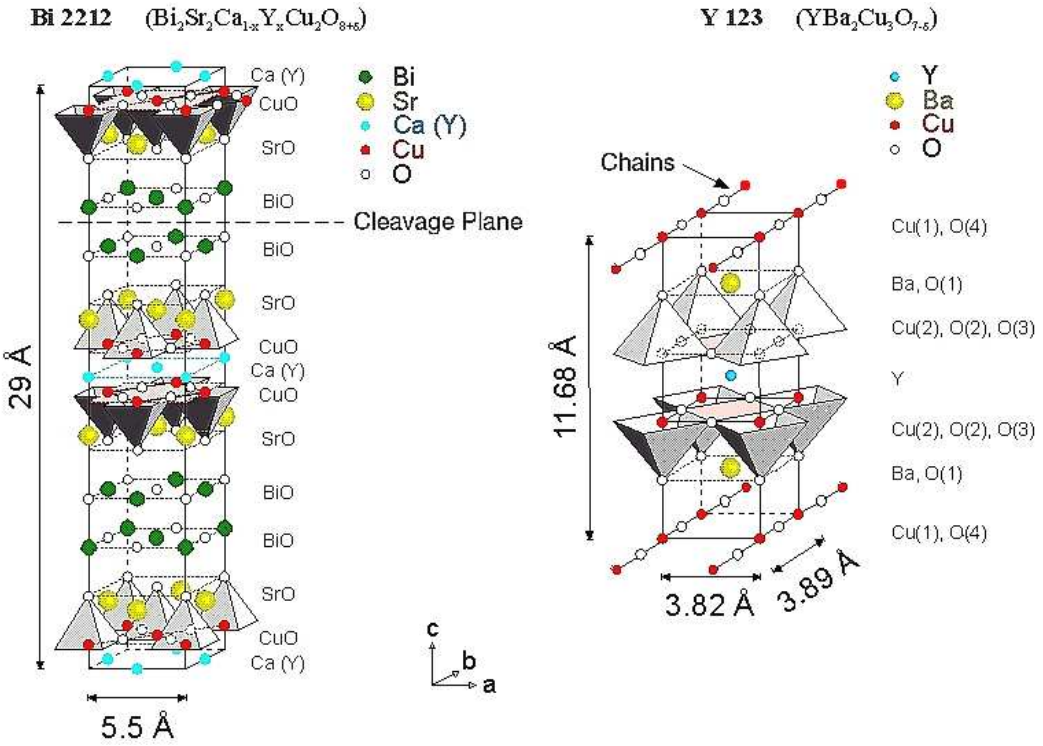

FIG. 1 The crystal structure of BSCCO and YBCO. Figure adapted from a presentation at Augsberg by Matthias Opel, Walther-Meissner Institute for Low Temperature Research of the Bavarian Academy of Sciences 2000.

The conductivity σ_1 for BSCCO also demonstrates non-Drude behavior by its slow decrease with frequency in the range of 400-8000 cm^{-1}:

$$\sigma_1 \propto \omega^{-.56\pm0.02} \qquad \text{versus} \quad \omega^{-2} \text{ for a Drude metal.}$$

Quijada also integrates the *f*-sum to 8000 cm^{-1} and identifies the result as 0.25 carriers per CuO_2 plane per unit cell.

Quijada analyses the conductivity for each axis separately using first a one component extended Drude model and then a multi-component extended Drude model. Using the values for the a axis of $\omega_p = 16200\,cm^{-1}$ and $\epsilon_\infty = 4.6$ and for the b axis of $\omega_p = 16240\,cm^{-1}$ and $\epsilon_\infty = 4.8$ the one component model produces for 300 K an isotropic mass renormalization factor of 2 at around 200 cm^{-1} which appears to decrease to 1 around 4000 cm^{-1}. The scattering rate increases linearly with frequency and is somewhat anisotropic from $\sim$700 cm^{-1} and upwards.

The multi-component analysis, referred to as "two component", assumes the transport to include the conductivity from a free carrier Drude, one or more infrared Lorenztians, and finally interband transitions. A self-consistent method of Romero *et al.* [7] removes the free carrier Drude contribution from the data for separate consideration. The resulting Drude term has an oscillator strength which is nearly temperature independent and a relaxation rate which in the normal state increases linearly in temperature. The calculated plasma frequencies are 9300 cm^{-1} for the a axis and 8900 cm^{-1} for the b axis. Finally, the DC extrapolation of the data agrees well with DC resistivity measurements.

The conductivity remaining after removing the free carriers includes the mid-infrared and interband transitions. The real part of this conductivity, somewhat anisotropic, is zero until $\sim$200 - 250 cm^{-1} above which it rises reaching a maximum at 1000 cm^{-1} then falling very slowly. Further, it shows almost no temperature dependence. The two different temperature dependences of this analysis is intriguing and perhaps bears some relationship to the behaviors seen in the high and low frequency AC Hall effect to be described later.

J. J. Tu *et al.* [6] presents certainly the cleanest data for σ_1 to date. It clearly resolves the optic phonons at 477 and 630 cm^{-1}. When analyzed with the extended

Drude formalism the scattering rate for 1000 cm^{-1} is 1450 cm^{-1} at 100 K and 1670 cm^{-1} at 300 K and increases with increasing frequency. They report a plasma frequency determined from the sum rule at 295K of 16000 cm^{-1}. They use this data to empirically determine the associated spectral function

$$W(\omega) = \frac{1}{2\pi} \frac{d^2}{d\omega^2} \left(\frac{\omega}{\tau(\omega)} \right).$$

The issue of all this is a value for the superconducting gap of 33 ± 3 meV at 6 K and (employing those theoretical models propounding spin-charge coupling) a value for the spin resonance of 41 ± 3 meV. Further, it appears that there may be a signature of the spin resonance above T_c for the BSCCO sample. Finally, they report that a cursory look at $La_{2-x}Sr_xCuO_4$ revealed no spin resonance, which is consistent with neutron scattering results. This would suggest that a simple AC Hall measurement on $La_{2-x}Sr_xCuO_4$ would help determine the relevance of spin resonance to the feature confirmed in the current work occurring around 30 to 60 meV.

While the DC and infrared conductivities reveal the overall response of the system to an electric field, the Hall effect reveals the sign of the carriers as well as some information as to the path taken by them. It essentially probes the ability of the carriers to veer or bend their course The quantities frequently used to represent the effect are θ_H, the Hall angle; R_H, the Hall constant; and σ_{xy}, the conductivity transverse to the externally applied magnetic and electric fields. We may relate these quantities beginning with a generalization of the notation of Ashcroft and Mermin [8] for the Hall constant:

$$\vec{E}_H = R_H \vec{H} \times \vec{J} \qquad (1)$$

where $\vec{J}$ is the current resulting from an externally applied electric field, $\vec{H}$ is the applied magnetic field, and $\vec{E}_H$ is the electric field which results from the charge redistribution caused by the Lorentz force. The simplest example of the effect involves a conductor possessing cubic symmetry and having a magnetic permeability of $\mu = 1$.

The material is subjected to an external magnetic field along the z axis. An external electric field applied in the positive x direction will cause a current flow whose constituents will experience a Lorentz force in the negative y direction regardless of the sign of their charge. When the steady state emerges, i. e., the DC result, the redistribution of charge will produce an electric field whose force on the charge carriers within the current will on the average cancel the Lorentz force. If the current is electron-like then this electric field will point in the negative y direction. If the current is hole-like then this electric field will point in the positive y direction. If $\vec{H} = H\,\hat{z}$, then

$$E_j = R_{\mathrm{H}}\, H\, J_i\, \epsilon_{3,i,j}\,. \tag{2}$$

The relation between the current and the externally applied electric field is

$$E_i = \rho_{i,i}\, J_i\,. \tag{3}$$

We may combine these into one equation:

$$\begin{pmatrix} \rho_{\mathrm{xx}} & -H\,R_{\mathrm{H}} \\ H\,R_{\mathrm{H}} & \rho_{\mathrm{xx}} \end{pmatrix} \begin{pmatrix} J_x \\ J_y \end{pmatrix} = \begin{pmatrix} E_x \\ E_y \end{pmatrix}. \tag{4}$$

Where the use of $\rho_{\mathrm{yy}} = \rho_{\mathrm{xx}}$ follows from the cubic symmetry. The conductivity matrix is obtained by inverting equation (4). Because our current concerns lie in the weak field limit, $|H\,R_{\mathrm{H}}| \ll |\rho_{\mathrm{xx}}|$; the inverse simplifies to:

$$\begin{pmatrix} \sigma_{\mathrm{xx}} & H\,R_{\mathrm{H}}\,{\sigma_{\mathrm{xx}}}^2 \\ -H\,R_{\mathrm{H}}\,{\sigma_{\mathrm{xx}}}^2 & \sigma_{\mathrm{xx}} \end{pmatrix} \begin{pmatrix} E_x \\ E_y \end{pmatrix} = \begin{pmatrix} J_x \\ J_y \end{pmatrix}. \tag{5}$$

Therefore, we see that

$$R_{\mathrm{H}} = \frac{1}{H}\,\frac{\sigma_{\mathrm{xy}}}{{\sigma_{\mathrm{xx}}}^2}\,. \tag{6}$$

Next, consider the Hall angle θ_{H}, which E. H. Putley [9] defines as

$$\tan\theta_{\mathrm{H}} = \frac{E_y}{E_x} \quad \text{for } J_y = 0. \tag{7}$$

Clearly, from equation (5):

$$\tan\theta_{\mathrm{H}} = \frac{\sigma_{\mathrm{xy}}}{\sigma_{\mathrm{xx}}}\,. \tag{8}$$

For a simple DC Drude model these quantities assume quite simple forms, which may be deduced from the conductivity matrix derived in Appendix 6.5 by setting $\omega = 0$:

$$\begin{aligned} \sigma_{xx} &= \frac{n q^2}{m} \tau \\ \sigma_{xy} &= \frac{n q^2}{m} \tau^2 \omega_c \\ R_H &= \frac{1}{H} \frac{\sigma_{xy}}{\sigma_{xx}{}^2} = \frac{1}{n q c} \\ \tan \theta_H &= \frac{\sigma_{xy}}{\sigma_{xx}} = \tau \omega_c \end{aligned} \tag{9}$$

where q is the carrier charge,

m is the carrier mass

τ is the mean time between scattering events

c is the speed of light,

$\omega_c = q H / m c$ is the cyclotron frequency,

and n is the carrier density.

These results serve as simple point of departure when considering the results for the cuprates below.

N.P. Ong [10], reported values for the Hall constant R_H in the normal state for different dopings of $La_{2-x} Sr_x CuO_4$. The data indicated positive (or hole) conduction. Then, collaborating with others for T. R. Chien *et al.* [11] and later for J. M. Harris *et al.* [12], he published data on impurity doped $YBa_2 Cu_3 O_7$ bringing to view the apparent T^2 dependence of the cotangent of the Hall angle θ_H. The behavior of R_H and θ_H is remarkable because in Boltzmann theory an increasing temperature changes the $\vec{k}$ dependence of $\tau(\vec{k})$ only for temperatures up to 0.2 to 0.4 times the Debye temperature T_D, which being about 400 K for the cuprates would limit the strong temperature dependence to ~200 K. In contrast R_H measured perpendicular to the planes is essentially independent of temperature up to the Debye temperature.

Additionally, they determined that oxygen reduction only scales R_H and $\cot\theta_H$. Therefore, a robust T^2 dependency even for different chain populations along with the temperature independent R_H in the direction of the c axis implies that the chains are one dimensional or in the very least do not contribute a significant Hall current. Their ultimate result is

$$\cot\theta_H = \alpha T^2 + \beta$$

where β is proportional to the zinc impurity concentration. They established the accuracy of this relation up to 500 K.

Among the latest published works for the DC Hall effect, Z. Konstantinovic *et al.* [13] from a systematic study of both single layer $Bi_2Sr_{1.6}La_{0.4}CuO_y$ and bilayer $Bi_2Sr_2CaCu_2O_y$ report

$$\cot\theta_H = B + C T^{\alpha}$$

where here α represents the temperature exponent, which for underdoped $Bi_2Sr_2CaCu_2O_y$ is 2, decreases to ~1.7 for overdoped, and is ~1.8 for optimally doped. The doping level was inferred from the phenomenological relation

$$T_c = T_{c\max}[1 - 82.6\,(p - 0.16)]$$

where p is the number of holes per copper atom in the planes.

Measurements of the Hall angle at the high frequencies of the infrared optical region is the natural extension to the foregoing. The quantities σ_{xx}, σ_{xy}, θ_H, and R_H all generalize easily to AC usually becoming complex quantities as we have already seen for σ_{xx}. As previously mentioned these experiments involve analyzing light transmitted by a thin film of the material which is subjected to an intense magnetic field of typically ±8 Tesla. The transmitted beam experiences a complex Faraday rotation. The real part of this rotation corresponds to a simple geometric rotation of the initial polarization vector about the propagation vector. The imaginary part corresponds to the

ellipticity of the transmitted beam and results from the preferential absorption of one circular polarization state over the other. Chapter 3 presents a detailed derivation of the relation between the transmitted polarization state, the complex Faraday angle, and finally the material properties σ_{xy}, θ_H, and R_H, which are our real concern. At this point it is sufficient to note that the polarization of the transmitted beam, when compared to that of the incident beam, is rotated and somewhat elliptical and that these data after some analysis will yield the material properties including σ_{xy}, θ_H, and R_H.

The Drude model results of equations (9) are also easily extended to AC using

$$\gamma \longrightarrow \gamma - i\omega$$

where $\gamma = 1/\tau$ is the scattering rate. The results are

$$\begin{aligned} \sigma_{xx} &= \frac{nq^2}{m}\,\frac{1}{\gamma - i\omega} \\ \sigma_{xy} &= \frac{nq^2}{m}\,\frac{\omega_c}{(\gamma - i\omega)^2} \\ R_H &= \frac{1}{H}\,\frac{\sigma_{xy}}{{\sigma_{xx}}^2} = \frac{1}{nqc} \\ \tan\theta_H &= \frac{\sigma_{xy}}{\sigma_{xx}} = \frac{\omega_c}{\gamma - i\omega} \end{aligned} \qquad (10)$$

When the Hall data for a particular material are analyzed against the above Drude model, the DC Hall effect potentially probes the sign, charge density, and mean free path of the participating carriers, whereas the AC Hall effect probes the Hall mass and the Hall scattering rate. This difference and its importance become clear in the examination of the normal state Hall effect in $YBa_2Cu_3O_7$ reported by Kaplan *et al.* [14]. This work accommodated the results of far-infrared AC Hall measurements by extending Anderson's model using the following substitutions:

$$\tau_{tr} \longrightarrow \frac{\tau_{tr}}{1 - i\omega\tau_{tr}} \qquad \text{and} \qquad \tau_H \longrightarrow \frac{\tau_H}{1 - i\omega\tau_H}$$

where τ_{tr} refers to the longitudinal transport scattering time and τ_H refers to the transverse or Hall scattering time. This leads to

$$\sigma_{\pm} = \frac{n q^2 \tau_{tr}}{m_{tr}} \frac{1}{1 - i\omega\tau_{tr}} \left(1 \pm \frac{i\omega_H \tau_H}{1 - i\omega\tau_H}\right)$$

where

$$\sigma_{\pm} = \sigma_{xx} \pm i\sigma_{xy};$$

ω_H is the Hall frequency:

$$\omega_H = \frac{qH}{m_H c},$$

which is analogous to the cyclotron frequency for a true Drude material; m_{tr} is the longitudinal transport mass; and m_H is the transverse or Hall mass. These equations for a Drude-type material produce

$$\mathrm{Re}[\cot\theta_H] = \frac{1}{\omega\tau_H} \quad \text{and} \quad \mathrm{Im}[\cot\theta_H] = \frac{-\omega}{\omega_H}.$$

Fitting their longitudinal and transverse data to the above equations, they determined that at 95 K

$$\tau_{tr}^{-1} = 127\,\mathrm{cm}^{-1} \qquad m_H = (5.2 \pm 0.7)\,m_e \qquad \tau_H^{-1} = 68 \pm 10\,\mathrm{cm}^{-1}$$

for the sample film grown on $LaAlO_3$ and

$$\tau_{tr}^{-1} = 190\,\mathrm{cm}^{-1} \qquad m_H = (6.6 \pm 0.8)\,m_e \qquad \tau_H^{-1} = 52 \pm 10\,\mathrm{cm}^{-1}$$

for the sample film grown on Si. Thus, the Hall mass and scattering time are considerably larger than those of the transport values.

In 2000, J. Cerne *et al.* [15] published data for the temperature and frequency dependence for the high-frequency Hall effect in YBCO. These data were obtained using the different spectral lines of a CO_2 laser and a very sensitive heterodyne detection system all of which form the basis of the current work and are detailed below in Chapter 2. The Hall coefficient indicated positive (or hole) carriers. When fit to a Drude model the Hall mass and the Hall scattering rate, to within the accuracy of the

data, display no frequency dependence within the range from 949 to 1079 cm^{-1}. However, the Hall frequency displays a slight decrease with increasing temperature, whereas the Hall scattering rate increases linearly with temperature from near zero at T_c to over 300 cm^{-1} at 250 K. Even though these results are complicated by the chain contribution present in $YBa_2Cu_3O_7$ they agree well with those of the current work for $Bi_2Sr_2CaCu_2O_y$ which does not suffer from this complication. In a related work by Cerne *et al.* [16] the same apparatus was used to measure the mid-infrared Hall effect in gold and copper films. The results agree quite well with band calculations and, therefore, recommend the use of this system in the study of other complex materials.

Recently M. Grayson *et al.* [17] using a novel high speed rotating analyzer examined the temperature dependence of the normal state Hall effect in $YBa_2Cu_3O_7$ over the frequency range of 25 to $\sim$300 cm^{-1}. The low frequency data, although consistent with DC Hall results as well as Kaplan *et al.,* when analyzed with the extended Drude formalism imply that both the Hall mass and Hall scattering rate increase linearly with temperature. This would suggest that the squared temperature dependence of the cotangent of the DC Hall angle actually results from a linear dependence of the resulting Hall mass multiplied by a linear dependence of the Hall scattering rate. This certainly raises questions concerning the effect of impurity scattering which in Ong's DC data resulted in a constant added to a single temperature squared term. Further, and very surprising, the data for the real part of the Hall angle unlike the values reported by Cerne *et al.* [15] become negative above 250 cm^{-1}. Employing a squared Lorenztian inspired by the theory of Varma and Abrahams [18] Grayson fit the plunge in the Hall angle and also collapsed the temperature dependent Hall mass into a single value over the entire frequency range. Here the significance of the AC Hall effect emerges most clearly. Because of the importance of these data they are included in plots below along with those of the current work. Further discussion will be postponed until then.

In addition to transport results let us also consider the closely related work with Angle-Resolved Photoemission Spectra (ARPES). In the past several years ARPES has mapped the Fermi surface and identified the d-wave symmetry of the order parameter. Recently, with improved resolution (10 meV for energy and .005 Å^{-1} for momentum with 15 to 21 eV photons), it has provided temperature and frequency dependence for the parallel momentum width versus angle around the Fermi surface. In order to relate ARPES data to transport measurements, researchers usually either equate the inverse momentum width to a "mean free path" or multiply it by the Fermi velocities and equate the product to a scattering rate. From the results reported in T. Valla [19] and [20] one finds that

$$k_F = .446\ \text{Å}^{-1}$$
$$v_F = 1.8\ \text{eV Å} \quad \text{(normal state)}$$

And, for near zero frequency the scattering rate in the normal state is approximately linear in both temperature and angle measured in the a,b plane from the diagonal but saturating at approximately 0.25 eV:

$$\gamma_{ARPES} \approx 0.005\,\theta\ \frac{\text{eV}}{\text{degrees}} + .0005\,\text{T}\ \frac{\text{eV}}{\text{K}}$$

T. Valla [20] shows γ_{ARPES} decreasing linearly with decreasing frequency until the frequency drops to an equivalent energy of about $3\,k_B\,T$. To relate this to mid-infrared transport one would average over all carriers with energies below that of the input radiation. Fig. 4 of Valla implies that the result for scattering by 125 meV or 10 micron radiation will have a small linear temperature dependence with large positive intercept. This agrees qualitatively with the σ_{xx} data in the mid-infrared. But, as we shall see, it is at odds with the Hall data of the current work which in the extended Drude analysis produce a scattering rate which has a linear temperature dependence and slightly negative intercept as does the data for YBCO of Cerne [15].

One additional feature discovered by ARPES measurements and reported by

P. V. Bogdanov *et al.* [21] is a kink in the quasiparticle dispersion curve, which for $Bi_2Sr_2CaCu_2O_8$ occurs at about 50±15 meV. The change in slope results in a reduction in velocity of around a factor of two above the kink. Z. X. Shen *et al.* [22] also report this kink occurring in LSCO at around 70 meV. The possibilities discussed for the origin of the kink are electron-phonon interaction, the opening of a 50 meV superconducting gap, spin resonance, or some type of interaction with the theorized stripe phase. It should be noted that LSCO does not show a strong spin resonance in neutron scattering

1.2 Current Theories

In addition to new and more accurate experimental methods and equipment the race to understand the cuprates has also birthed a myriad of theories. Some conjure exotic new participants to the field of transport, such as Anderson's model [23] and P. A. Lee's model, which both posit the existence of spinons and holons. Other approaches, perhaps more cautious, seek to adapt existing theoretical or phenomenological machinery to the task. These include V. Yakovenko's model presented in A. T. Zheleznyak [24] and the Ioffe-Millis model [25], both of which adapt Fermi Liquid theory to include $\vec{k}$ dependent scattering, and also the model of Abrahams and Varma [18], which adapts Marginal Fermi Liquid to include $\vec{k}$ dependent scattering.

As mentioned Anderson's theory posits the existence of two additional particles—spinons, which are spin 1/2 Fermions without charge, and holons, which are spinless Bosons with a charge equal to one hole. The spinons form a Fermi surface of the same size proposed for electrons and mapped by ARPES. The holons carry the current against a backflow of spinons which cause scattering proportional to, $k_B T$, the spinon thermal excitations. Anderson further indicates that in the presence of a magnetic field spinon-spinon scattering enters the transport phenomenon with the characteristic T^2 / W_s dependence of Fermi statistics where W_s is the spinon bandwidth

expected to be equal to the magnetic exchange energy $J \sim 1400$ K. These two interactions may therefore be considered as two separate scattering rates: τ_{tr} for holon-spinon and τ_H from spinon-spinon. Thus, Hall conduction would be characterized by the product $\tau_{tr}\,\tau_H$. This indeed produces the T^2 behavior for the DC Hall angle. However, the resulting value for W_s calculated from Chien [11] using the Hall mass from Kaplan [14] is in substantial disagreement with that anticipated. Consider that

$$\frac{1}{\tau_H} = \frac{T^2}{W_s},$$

$$\cot\theta_H = \frac{1}{\omega_c\,\tau_H}$$

and $$\omega_c = \frac{qH}{m\,c}$$

But, from Chien [11] Fig. 2

$$\cot\left[\theta_H(T = 245\text{ K})\right] = \frac{1}{300}$$

and from Kaplan [14]

$$m_H \approx 6\,m_e\,.$$

Combining all of the above $W_s \approx 18$ K, not 1400 K. The implied Fermi energy which would be about $2\pi\,W_s \approx 100$ K (see Ashcroft and Mermin [8]) which would seem far to low to justify the use of Fermi Liquid Theory to explain phenomena at 300 K.

Application of Anderson's theory to the AC Hall angle requires the usual extension $\frac{1}{\tau} \rightarrow \frac{1}{\tau} - i\omega$ with the result

$$\theta_H^{-1} = \frac{1}{\omega_c\,\tau_H} - i\,\frac{\omega}{\omega_c}\,.$$

Because τ_H in this theory is the result of spinon-spinon scattering, one might expect that it would depend on frequency also as

$$\frac{1}{\tau_{\mathrm{H}}} = \frac{1}{\tau_{\mathrm{imp}}} + \frac{\mathrm{T}^2}{W_s} + a\,\omega^2 .$$

Therefore, at high frequencies the real part of the inverse Hall angle should increase as ω^2 whereas by Cerne [15] and the data of the current work it is essentially frequency independent.

The Yakovenko model as presented in [24] divides the Fermi surface into two types of regions—small corner segments which have a low scattering rate that increases as T^2 and the remaining flat sections which have a scattering rate about four times higher that increases linearly with T. The scattering rates are presumed independent of frequency which is taken to exclude the theory from application to high frequency phenomena. The ultimate result is a sum of two Drude forms with six adjustable parameters. The basic equations are

$$\begin{aligned} \sigma_{\mathrm{xx}} &= \frac{{\omega_p}^2}{4\pi}(a_1\,\tau_1 + a_2\,\tau_2), \\ \sigma_{\mathrm{xy}} &= \frac{\omega_{\mathrm{H}}\,{\omega_p}^2}{4\pi}(b_1\,{\tau_1}^2 + b_2\,{\tau_2}^2) \end{aligned} \tag{11}$$

where the τ's are to be extended as $1/\tau \rightarrow (1/\tau) - i\,\omega$.

The Ioffe-Millis model [25] instead chooses a smooth angle dependence for the scattering rate

$$\Gamma(\theta,\ \mathrm{T}) = \frac{1}{4}\,\Gamma_0\,(\mathrm{Sin}(2\,\theta))^2 + \frac{1}{\tau_{\mathrm{FL}}} \tag{12}$$

where $$\frac{1}{\tau_{\mathrm{FL}}} = \frac{1}{\tau_{imp}} + \frac{\mathrm{T}^2}{\mathrm{T}_0}.$$

The frequency dependence of τ_{FL} is presumed to be weak. Using photoemission data indicating an energy half width of 0.1 eV for $\mathrm{T} \ll \mathrm{T}_0$ implies $\Gamma_0 \approx 0.4\,\mathrm{eV}$. However, the authors use $\Gamma_0 = 0.6\,\mathrm{eV}$ because it fits the optical data. The resulting forms for σ_{xx} and σ_{xy} are:

$$\sigma_{xx} = \frac{e^2 v_F p_F}{\pi} \sqrt{\frac{\tau_{FL}}{\Gamma_0}} \frac{1}{\sqrt{1 - i\omega\tau_{FL}}} \qquad (13)$$

and $$\sigma_{xy} = \frac{\sigma_{xx}}{4} \frac{\omega_c \tau_{FL}}{1 - i\omega\tau_{FL}}.$$

At variance with these theories, the phase of the conductivity (the ratio of the imaginary part to the real part) as seen in Quijada [5] and also in the data of J.J. Tu, as shown below in Fig. 19 in section 4.2, show a curious peak around 400 cm^{-1} at low temperatures which is not predicted by the above forms. Further, the large angle variation of the scattering rate is questioned in Valla [19] although the connection between ARPES and transport is yet uncertain and the ARPES data is quite noisy. In section 4.2 we shall graph these forms along with the data of Grayson and that of the current work.

Very recently C. M. Varma and Elihu Abrahams [18] presented their theory to explain the Hall effect in the cuprates using Marginal Fermi Liquid theory MFL along with the hypothesis that the angle dependent scattering demonstrated by, for example, Valla [19] is caused by doping impurities between the Cu-O planes, which produces only small angle elastic scattering having little effect on σ_{xx}. Consider that the self-energy can be written as

$$\mathrm{Im}\Sigma(\vec{k}, T) = \Gamma(\vec{k}) + \lambda T$$

where the first, angle-dependent term is considered elastic (independent of temperature and/or frequency) and the second term is the inelastic MFL scattering. Solving the $\vec{k}$ dependent Boltzmann equation and forming σ_{xy}/σ_{xx} produces

$$\tan\theta_H = (\tan\theta_H)_0 + \left[\frac{\omega_H \tau_t^2}{\tau_p}\right]_{ave}$$

where the first term is the previous result without the assumption of small angle scattering and the second term, which is averaged over the Fermi surface, is the correction. The Hall angle predicted by the first term is a factor of five smaller than

measured values thus suggesting that the majority of the measured Hall angle perhaps follows from the second term. This line of reasoning, though presently controverted in the community, leads one to look to the second term for the leading frequency and temperature dependence. This second term indicates that the Hall angle follows the square of the transverse scattering rate. As mentioned earlier, Grayson [17], using the usual AC extension, fit his data to a squared Lorentzian with rather compelling results. Specifically, when using as the Hall angle expression

$$\theta_H \propto \frac{\omega_H}{(\Gamma_H - i\,\omega)^2}$$

the plots for ω_H collapsed into a single value, independent of frequency or temperature, and the scattering rate became linear in temperature, showing a slight, not unexpected, increase with frequency.

The real part of the above form generates negative values at low scattering rates (low temperatures) and frequencies above 250 cm^{-1} , which is consistent with the data of Grayson. However, as will be seen, the high frequency data of the current work demonstrates a positive Hall angle which this theory does not predict.

The Varma and Abrahams approach touches upon the real relevance of ARPES to transport and its dependence upon the Fermi-Liquid theory. The proper application of ARPES data requires a more complex approach , such as the Kubo formula, to calculate transport properties rather than the simple direct assignment of mean free paths or scattering rates. The latter approach can obviously lead to discrepancies if the some of the scattering processes determining the ARPES lengths have little effect on longitudinal transport, e.g., small angle scattering. If after applying the Kubo formula one obtains results which do not agree with transport data, then we might well conclude that Fermi liquid theory is not an appropriate description of the HTC cuprates. In short we should consider ARPES data not as a substitute for transport but rather as one party in this most useful comparison—the other party being actual transport data, which is the

concern of the current work.

The current work intends to expand the existing Hall transport data in the mid-infrared to single crystal 2212 BSCCO whose structure is shown along with that of YBCO in Fig. 1. This material does not possess the doping chains of YBCO nor the twinning which complicates the calculations of Cerne [15]. Additionally, the agreeable cleavage of BSCCO, has also made it the material of choice for ARPES and Scanning Tunneling Microscopy STM measurements. So transport data on BSCCO facilitates a more direct comparison with the results of these fields. The current work also reduces the noise or scatter in the temperature data of previous work by using a redesigned sample handling system which permits direct, fast temperature scans to reduce $1/f$ noise. This new apparatus along with a greater temperature range confirms the linearity of the effective scattering rate.

In the material which follows, we shall discuss the experimental system in terms of the apparatus in Chapter 2, derive the equations requisite to determining the material properties from the raw data in Chapter 3, present and discuss the results of the measurements on BSCCO in Chapter 4, and we shall conclude our discussion in Chapter 5.

2 Experimental System

An army of details in defiance arose
Without central command no serious foe,
Each member dispatched with decisive resolve
Embalmed, boxed and interred below.

2.1 Overview

The experimental system of the current work measures the very small Faraday angle imparted to CO_2 laser radiation traveling perpendicular to and transmitted by the sample film which is placed in a perpendicular magnetic field. During operation the experimental system performs four major tasks essentially simultaneously:

1) generating and directing a monochromatic, linearly polarized light beam normal to the sample
2) producing and controlling a magnetic field at the sample normal to its surface
3) setting and maintaining the temperature of the sample
4) analyzing the portion of the light beam transmitted by the sample to determine the complex Faraday angle.

Figure 2 schematically illustrates the optical path about which this portion of our discussion will mainly center. Additionally, plates 1 through 5 at the end of this chapter depict the actual hardware and equipment involved. Referring to Fig. 2 the light beam initially issues linearly polarized from the CO_2 laser and after enduring various steering and attenuation components not shown, it proceeds through lens 1 which focusses it to a point at the chopper. The chopper impresses onto the intensity of the beam a temporal squarewave of ~112 Hertz which will later facilitate the removal

of laser power variations using ratios. Lens 2 then refocuses the emerging beam so as to eventually produce a focussed diffraction spot on the surface of the sample. The intervening element, a film polarizer, "cleans up" the beam's polarization, removing

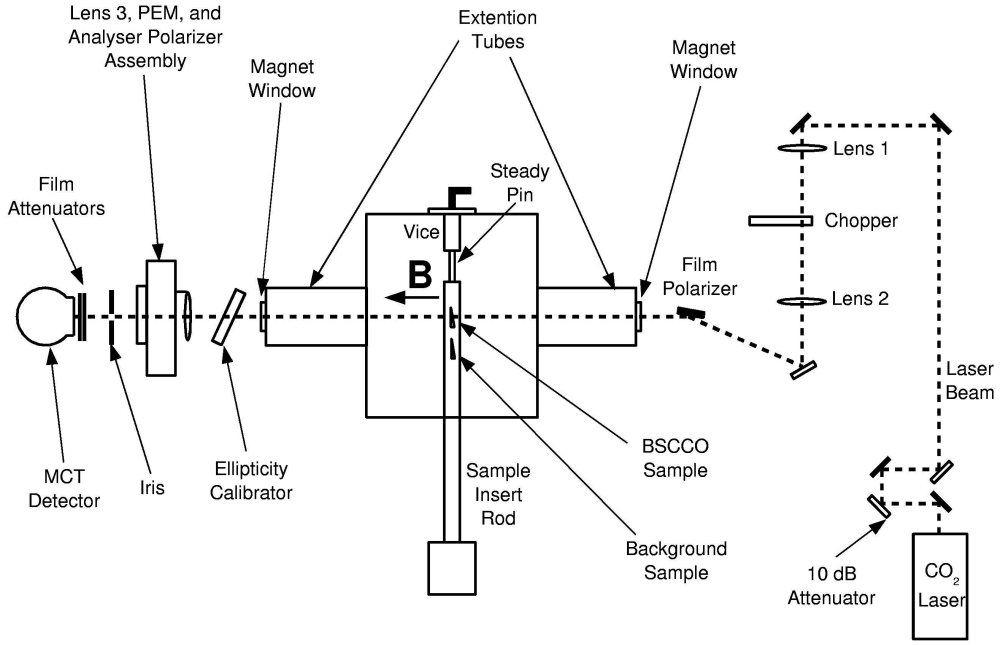

FIG. 2 Overall schematic of the optical path. The the dotted line represents the CO_2 laser beam. The CO_2 laser and the first four optic elements are actually located on a separate mount detached from the optical table.

any contamination caused by the chopper, attenuators, etc. It is this highly linearly polarized beam, which after passing through the ZnSe magnet housing window (not shown), encounters the sample as shown in Fig. 3. The sample reflects ~83% of this beam, absorbs ~16%, and transmits ~1%. The transmitted portion will have sustained a Faraday rotation proportional to the magnetic field and consistent with the physics peculiar to the cuprate-based, high temperature superconductors. We shall assign the x axis to the initial polarization direction and the z axis to the direction of propagation.

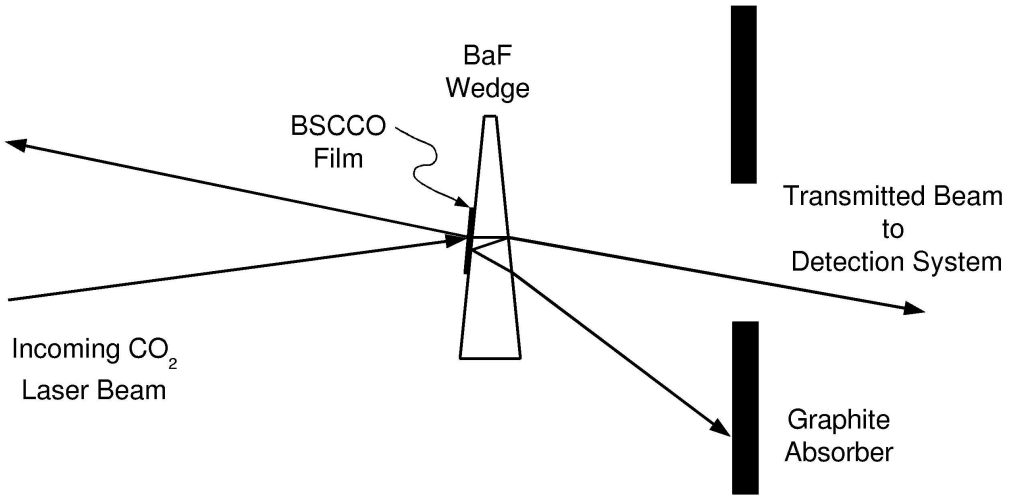

FIG. 3 Wedged sample and beam path. The paths of the reflected beams are sufficiently separated by the 2° wedge to prevent their entering the detection system or reentering the laser.

The Faraday rotation includes both real and imaginary terms. The real term corresponds to a simple geometric rotation of the polarization vector about the direction of propagation. The imaginary term, constructed mathematically by analytically continuing the real Faraday angle, relates directly to the ellipticity of the polarization and has frequently been referred to as the circular dichroism. The magnitude of the Faraday rotation at CO_2 wavelengths is minute—about 10^{-4} radians. As such, one may consider the electric vector along the y axis to be a feeble signal added to the comparatively prodigious signal of the original the electric vector along the x axis. This small signal cannot be measured directly by the common method of cross polarizers because the power in the field polarized along the y axis, called the y channel, is proportional to the square of the Faraday angle or $\sim 10^{-8}$ times the power in the original beam in the x channel. Clearly, leakage of the input beam through either polarizer would effectively direct power into the y axis channel which would well overwhelm any amount occasioned by the sample. The natural choice in such instances is heterodyne detection.

Heterodyne detection multiplies the two channels producing a cross term which is proportional to the electric vector along the y axis rather than its square. We realize heterodyne detection by phase modulating the electric vector along the y axis using a PEM, photoelastic modulator. The PEM modulator is a model 90 manufactured by Hinds Instruments, Inc. with a modulation frequency of 50 kHz. It comprises essentially a block of ZnSe and a piezoelectric transducer which creates the stress alternations at a frequency of 50 kHz and ultimately the phase modulation of the light beam. The electric vector along the x axis is essentially unaffected by the PEM.

Returning to our discussion of the optical path the beam emerges from the PEM and then strikes a polarizer on a 45° angle, which, simply stated, allows a portion of the electric vector from each of the y and x directions to contribute to that which emerges now at a 45° degree angle. On the face of the detector these contributions, of course, interfere producing the 50 kHz PEM frequency along with sidebands. The amplitudes of the sidebands are proportional to the electric vector along the y axis and also proportional to the corresponding Bessel function whose argument is the depth of modulation. In fact, as will be derived in Chapter 3, the even sidebands or harmonics are proportional to the real part of the Faraday angle and the odd sidebands or harmonics are proportional to the imaginary part of the Faraday angle.

In the following sections we consider certain elements or subassemblies of the experimental system in detail beginning with the CO_2 laser.

2.2 CO_2 Laser

The CO_2 laser, fashioned from a model PL5 manufactured by Edinburgh, provides a number of spectral lines ranging from 9.174 to 10.860 microns (920 to 1090 cm^{-1}), any one of which is selected by a grating internal to the cavity. A separate CO_2 laser spectrometer manufactured by Optical Engineering verifies the wavelength of each line. The direction of the beam exiting the laser, however, differs for different

lines sometimes by nearly as much as one half of a spatial mode. Without realignment the result would be a spatial shift of the diffraction spot at the sample by as much as one half of a spot diameter. The small size of the sample aggravates the sensitivity of the system to such slight misalignment particularly when such changes cause the beam to wander off or even near the edge of the sample. Lens 3 and the iris shown in Fig. 2 aid in regaining alignment as is necessary to compile valid relative frequency data for the small peeled BSCCO sample of the current experiment. With a moment's thought one will recognize that lens 3 essentially focuses an image of the sample onto the iris. The design and construction of the hardware well ensures that the relative position of the sample, lens 3, and the iris are constant. Therefore, adjusting the laser beam steering to maximize the power through the iris after each laser line change likewise ensures that the beam is passing through the same area of the sample. While actually taking data the iris is dilated to accommodate a small amount of beam wander.

Another consideration of the laser is the high output power—2 to 30 Watts. Attenuators, also shown in figure 1, reduced the power ~30dB to avoid heating the sample while still producing a robust signal within the linear range of the MCT detector. These attenuators are ZnSe windows having an antireflection coating on one side. They replace mirrors in the beamsteering assemblies with the uncoated side serving as the reflective surface. Each of these attenuators introduces approximately 10 dB of loss.

The output power of the laser, notwithstanding its hardiness, fluctuates temporally. Therefore, producing usable data requires the formation of simultaneous ratios between the 2nd and 3rd harmonics, and a sample of the laser power level. The current experiment employs the usual method of "source compensation" [27] which involves the chopper shown in Fig. 2 along with an additional lockin amplifier. Note also that the heterodyne detection system described above permits use of the same detector for the power level sample as well as the 2nd and 3rd harmonics. As to be

derived in Chapter 3, the power level sample, aside from the chopper frequency, corresponds to the original optical carrier frequency centered within the sidebands mentioned above. This unique feature eliminates the effect of the dependence of the detector response to different optical wavelengths and thus facilitates accurate relative measurements of the wavelength dependence of the complex Faraday angle.

A final consideration regarding the laser involves its placement with respect to the magnet. The particular position of the laser as seen in plate 1 is perpendicular to the magnetic field and at such a distance as to reduce detuning of the laser cavity, caused by magnetostriction, to a tolerable amount.

2.3 Magnet System and Sample Mounting

The magnet system began as an 8 Tesla, split coil, Helmholtz Spectromag manufactured by Oxford Instruments and, except for modifications to the external windows, the sample handling hardware, and the internal bore tube shielding, it has served the experiment with little modification. To understand the modifications to the external windows, consider that the wavelength range of interest requires ZnSe windows. However, the band gap of ZnSe is only 2.7eV, and the magnetic field of 2 Tesla at the original location of the windows caused a significant Faraday rotation, which overwhelmed that of the sample. The extension tubes locate the windows where the magnetic field is less than 0.1 Tesla. The remaining Faraday rotation background is thus reduced to the same order as that of the sample and having been carefully measured for different wavelengths can be easily removed from the data at a later time.

The sample handling hardware, inadequate and ill-fit as supplied, enjoyed substantial redesign and remanufacture. The effort included adding a steady pin and vice, implementing a more responsive temperature control system, and developing a near stress free sample mount. Plate 3 depicts the steady pin, which is also shown schematically in Fig 2. The pin protrudes from the blade of the original sample stick to

which it is brazed. The vice, shown only in Fig 2, engages the pin using a teflon collet. This combined apparatus restrains the sample stick against the forces induced by the magnetic field. Without this restraint the motion of the sample during the magnetic field sweeps caused curious, unpredictable oscillatory signals which utterly obscured the sample response.

Plate 3 also depicts the new temperature control system which comprises a heater and a cooling link. The heater is a 400 Ohm 1/4 Watt resistor potted into the copper sample carrier using 2850FT Epoxy with Catalyst 9 both of which are manufactured by Emerson & Cuming. The cooling link is simply a 4 cm length of 22 gauge copper wire connecting the copper sample carrier to the blade of the original sample stick from which it is otherwise thermally insulated by spacers and nylon screws. The operation is delightfully simple. Liquid helium delivered to the sample stick by the original provision, cools the blade to about 10 K, and the cooling link cools the copper sample carrier. Current delivered to the resistor in an easily controlled fashion can provide up to 2 Watts of heat to the copper sample carrier. Because of the low thermal mass of both the copper sample carrier and the link, a compromise temperature emerges within about one minute. Sweeping the temperature entails nothing more than adjusting the current. A important advantage of this system is that only the rather small copper sample carrier changes temperature. The other hardware, remaining essentially constant in temperature, finds little reason to move or warp and adversely affect the measurement.

The near stress free sample mount consists of a phosphor bronze wire retaining spring and a thermally conductive flexible silver filled RTV known as Eccobond 59C manufactured by Emerson & Cuming, Inc. The BSCCO sample is a small irregularly shaped film approximately 200 nanometers thick which had been peeled by D. Romero of the Laboratory for Physical Science, University of Maryland from a single bulk crystal of BSCCO 2212 grown by G. D. Gu of the Department of Physics, Brookhaven

National Laboratory, Upton, NY. This small film is placed against a polished surface of a barium fluoride crystal which serves as a substrate and maintains the temperature of the sample. Van der Waal's force holds the film in place. A 2° wedge of the BaF substrate eliminates etalon effects. Only one of the two corners of the substrate is cemented to the copper sample carrier. The phosphor bronze retaining spring lightly holds the other corner while allowing some motion to relieve the stress caused by dissimilar thermal expansion coefficients. Without this provision the stress induced in the substrate had caused overwhelming and unpredictable complex Faraday rotations. It is this stress free mounting which actually facilitated the fast temperature scans required to eliminate 1/f noise apparent in previous work.

The copper sample carrier is provided with a small indexing hole also shown in plate 3. Prior to insertion of the sample stick into the magnet the sample's position is accurately measured with respect to this hole. After insertion, the indexing hole is located using the transmitted intensity of the laser beam. The sample is then positioned within the beam by raising or lowering the magnet and sliding the sample stick in or out.

The new reentrant bore tubes are not shown in any figures. They are fit with graphite plates to absorb the stray radiation scattered from the incident laser beam by the various reflective surfaces, e.g., the sample, the BaF substrate, the magnet windows, etc.

2.4 Optical Table Components

Plate 2 provides a view of those items of Fig. 2 which are located on the aluminum optical table and which will receive consideration within this section. Among these items are the chopper and lens 1. As explained above, the chopper impresses upon the beam a squarewave amplitude variation of 112 Hertz. Lens 1 participates in this task by focusing the beam to a point at the chopper blades. Thus, the passage of a blade cuts the beam off and on in an most abrupt manner. This prevents

spatial variations within the beam from causing phase and amplitude errors in the reported laser power level.

Also of particular importance, though not well depicted, is the pivot platform upon which sits the optical detection system. Two aluminum box beams connect this platform to a vertical pivot located directly below the sample. When the two clamps securing the platform to the optical table are loosened the platform may be rotated about the vertical axis of the pivot. This motion is necessary to align the detection system to both the indexing hole and wedged substrates which bend the laser beam about the same axis by an amount depending on the substrate wedge angle and its index of refraction.

The laser beam having passed through the sample and having exited the magnet next encounters the ellipticity calibrator. This calibrator comprises a ZnSe window and a removable weight, which when suspended as shown in plate 4 compresses the window along a direction approximately 35° from the horizontal. The resulting birefringence introduces an ellipticity into the laser beam. The calculated variation of this ellipticity with laser wavelength compared to the empirical result can supply a calibration standard if the stress-optic coefficient of ZnSe is determined. The etalon effects of the window are standardized by rotating the calibrator about its mounting post to obtain an etalon transmission maximum (or alternatively a minimum) for each wavelength. When taking data the calibrator is removed.

2.5 Optical Detection System

The first component encountered by the laser beam after passing through the magnet window and ellipticity calibrator is lens 3 which focusses an image of the sample onto the iris as previously discussed. This lens joins with the PEM and polarization analyzer in an assembly shown in plate 5. This entire assembly can be rotated as a single unit about the input optical axis which is the z axis. With another

moment's thought one will recognize that such a rotation is equivalent to a real, but opposite, Faraday rotation, at least for sufficiently small angles so that the polarization sensitivity of the MCT detector is not apparent. Referring to plate 5, a calibration rotation limit in fact limits this rotation to a known amount thus serving as a Faraday rotation calibrator. Simply put, one rotates the assembly the known amount and uses this to scale the empirical values for each wavelength.

Another important consideration involves reflection at the surfaces of the ZnSe interaction block of the PEM. A reflected beam which makes additional passes through the ZnSe interaction block will receive additional modulation. Since, the cross term is proportional to the depth of modulation such triply modulated stray beams can cause significant errors. An AR coating and, as shown in plate 5, a tilting of the PEM by 25° reduce and displace reflected beams and, thereby, sufficiently reduces their effect.

A variable selection of polyimide films attenuate the laser beam so that its power is within the linear range of the MCT detector which is a model J15D14 mercury cadmium telluride detector manufactured by EG&G Judson. This happens to correspond to about 100 mV at the output of the MCT preamp.

2.6 Electronic Instrumentation

Along with the electronics which attend the magnet, PEM, chopper, etc., the system uses three lockin style, harmonic amplifier/detectors manufactured by EG&G and designated as "7260 lockin amplifier" and " 7265 lockin amplifier". These lockins differ from previous styles in that they detect and report the complex coefficient of a selectable harmonic of the input signal. This feature is essential because, as derived later, the even harmonics of the phase modulation of the PEM are proportional to the real part of the Faraday angle and the odd harmonics are proportional to the imaginary part. The 7260 lockin determines the RMS voltage at 112 Hertz and is usually considered to be the DC reference. One of the 7265 lockins determines the RMS

voltage at 2ω, the 2nd harmonic of the PEM frequency, and the other determines the RMS voltage at 3ω, the 3rd harmonic. A Labview program running on a local computer records data points consisting of the following:

$$\left\{\text{time in seconds or B field in Tesla}, \frac{2\omega\ \text{RMS voltage}\ (x\ \text{channel})}{112\ \text{Hz RMS voltage}}, \frac{2\omega\ \text{RMS voltage}\ (y\ \text{channel})}{112\ \text{Hz RMS voltage}}, \frac{3\omega\ \text{RMS voltage}(x\ \text{channel})}{112\ \text{Hz RMS voltage}}, \frac{3\omega\ \text{RMS voltage}(y\ \text{channel})}{112\ \text{Hz RMS voltage}}, .112\ \text{Hz RMS voltage}\right\}$$

If the beam moves within the PEM aperture the phase of the harmonics will change. This phase is initially set such that the y channel is very nearly zero with most of the signal in the x channel. To avoid any errors from the changing phase we use a combination of the x and y channels:

$$\text{data}2\omega = \text{sign}\sqrt{\left(\frac{2\omega\ \text{RMS voltage}\ (x\ \text{channel})}{112\ \text{Hz RMS voltage}}\right)^2 + \left(\frac{2\omega\ \text{RMS voltage}\ (y\ \text{channel})}{112\ \text{Hz RMS voltage}}\right)^2}$$

and

$$\text{data}3\omega = \text{sign}\sqrt{\left(\frac{3\omega\ \text{RMS voltage}\ (x\ \text{channel})}{112\ \text{Hz RMS voltage}}\right)^2 + \left(\frac{3\omega\ \text{RMS voltage}\ (y\ \text{channel})}{112\ \text{Hz RMS voltage}}\right)^2}$$

where "sign" is either +1 or −1 and reintroduces the sign of the original x channel.

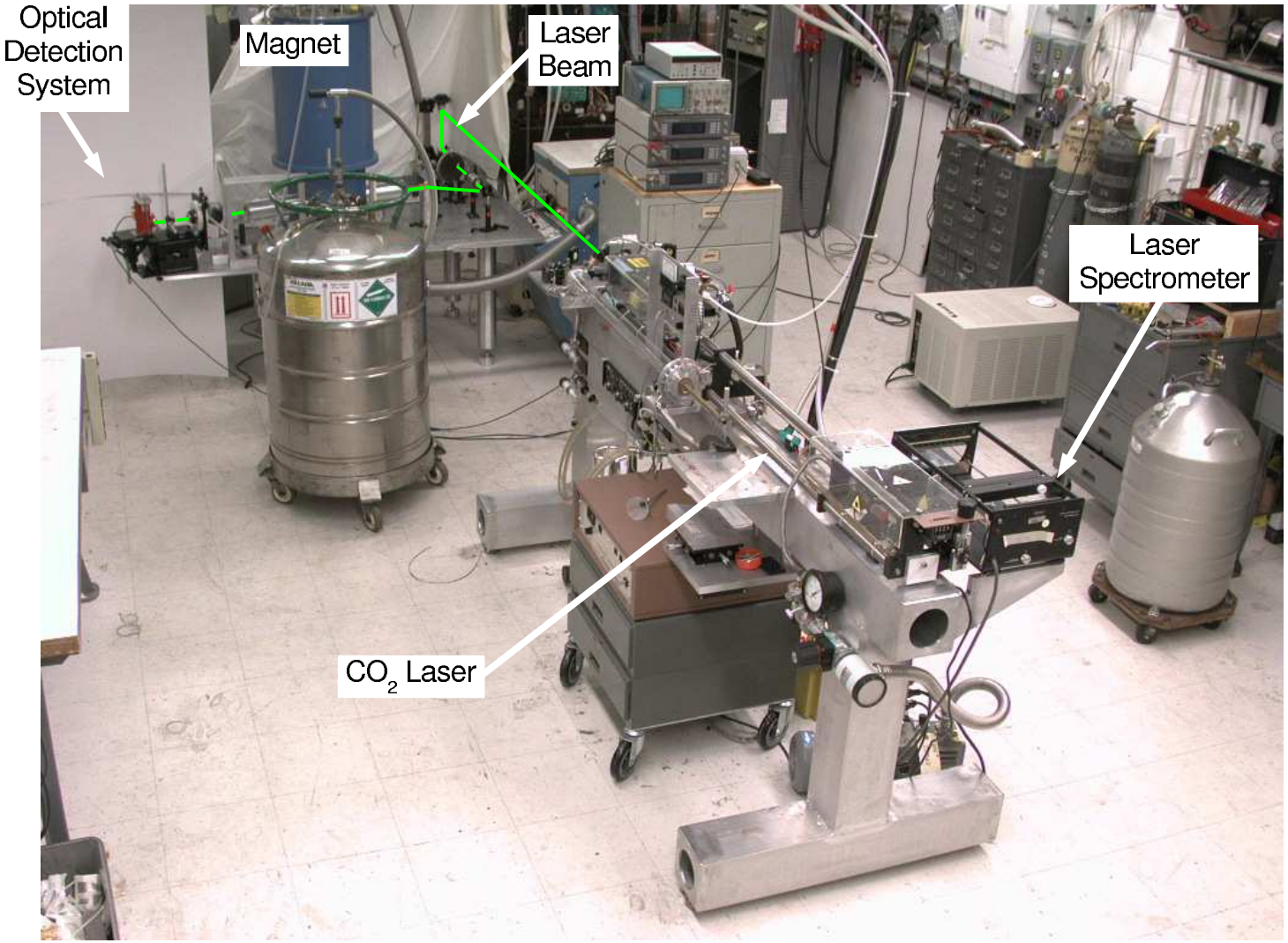

Plate 1 Overall View of Experimental System

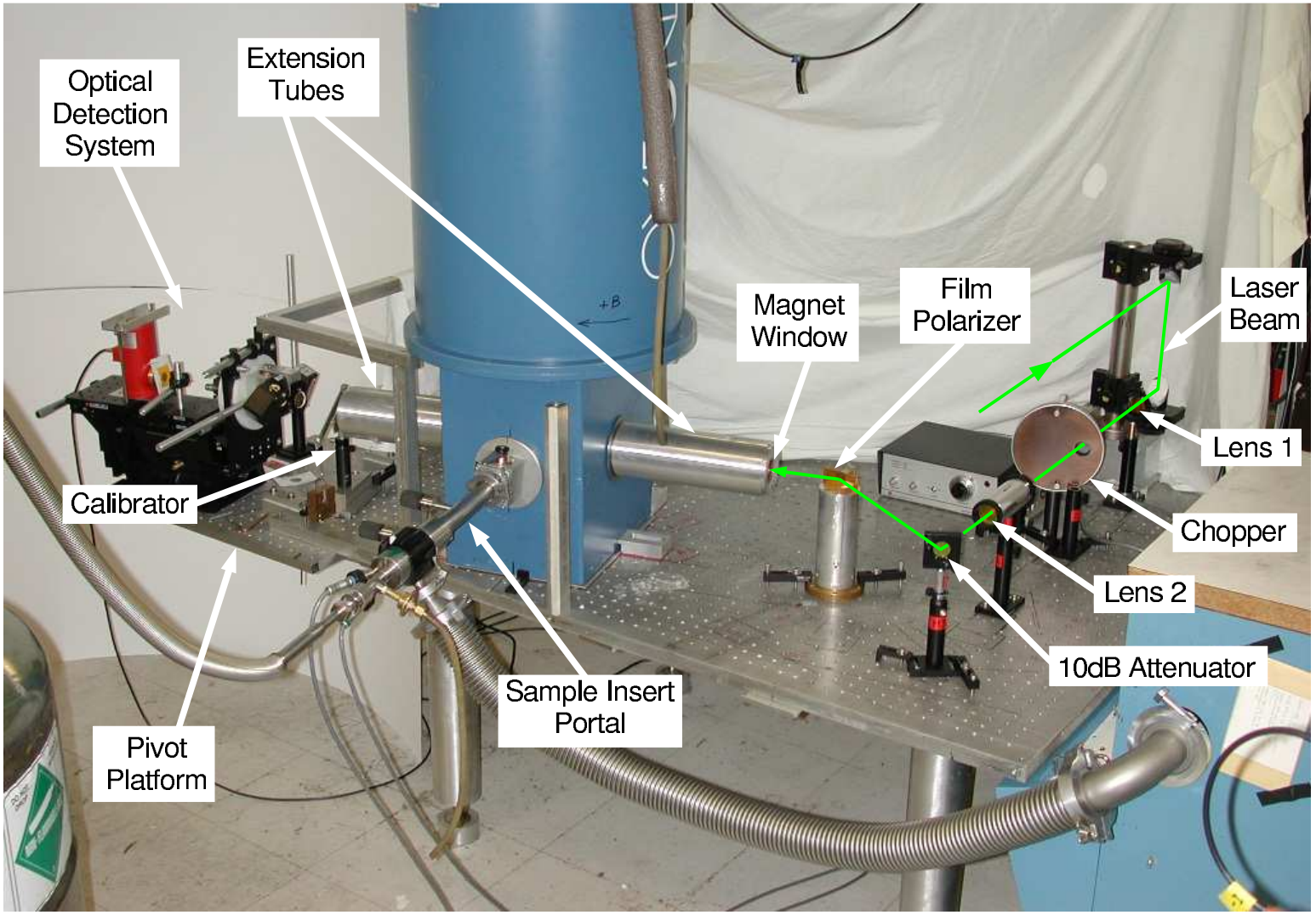

Plate 2 Optical Table

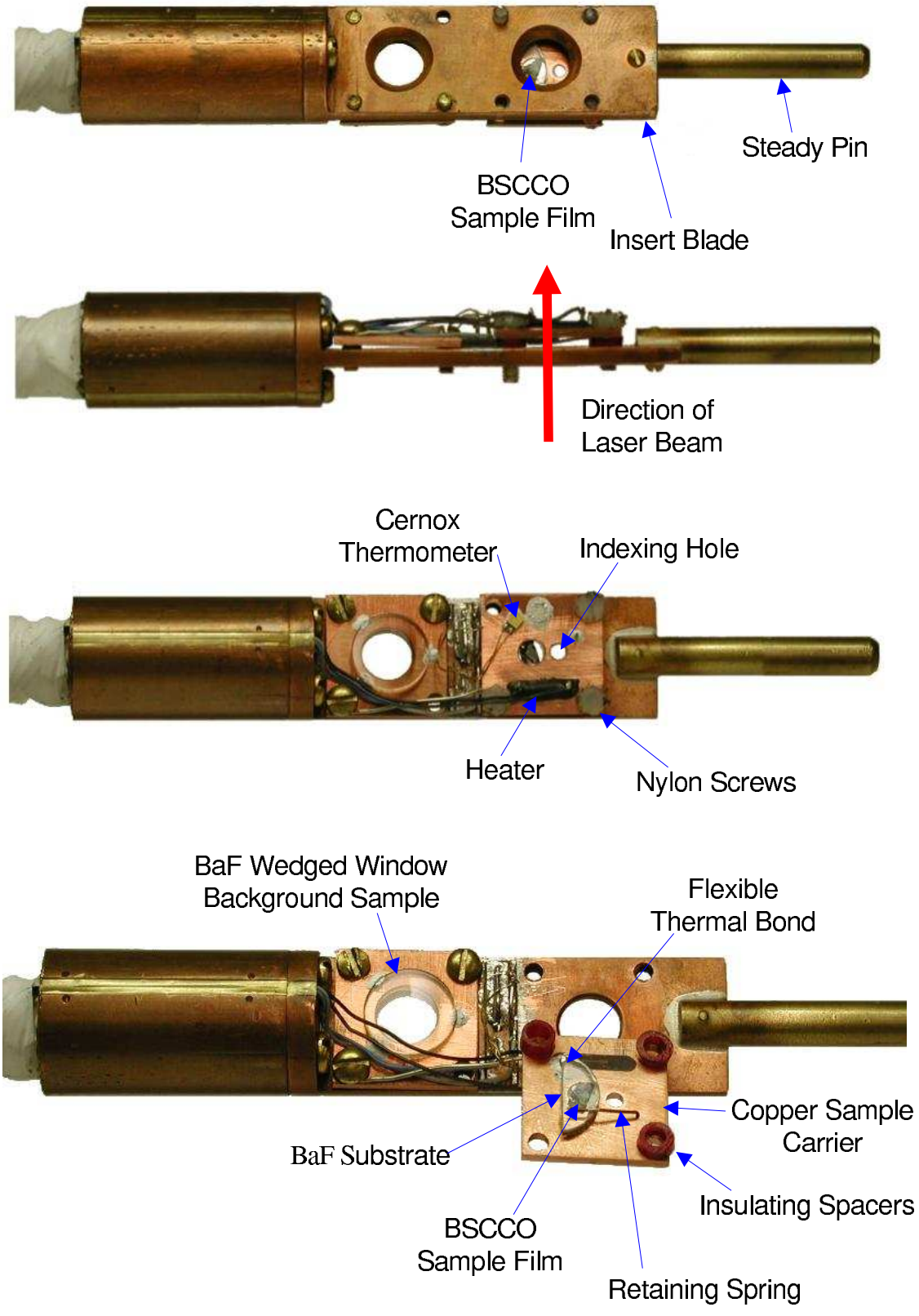

Plate 3 Sample Mount Assembly

Plate 4 Ellipticity Calibrator

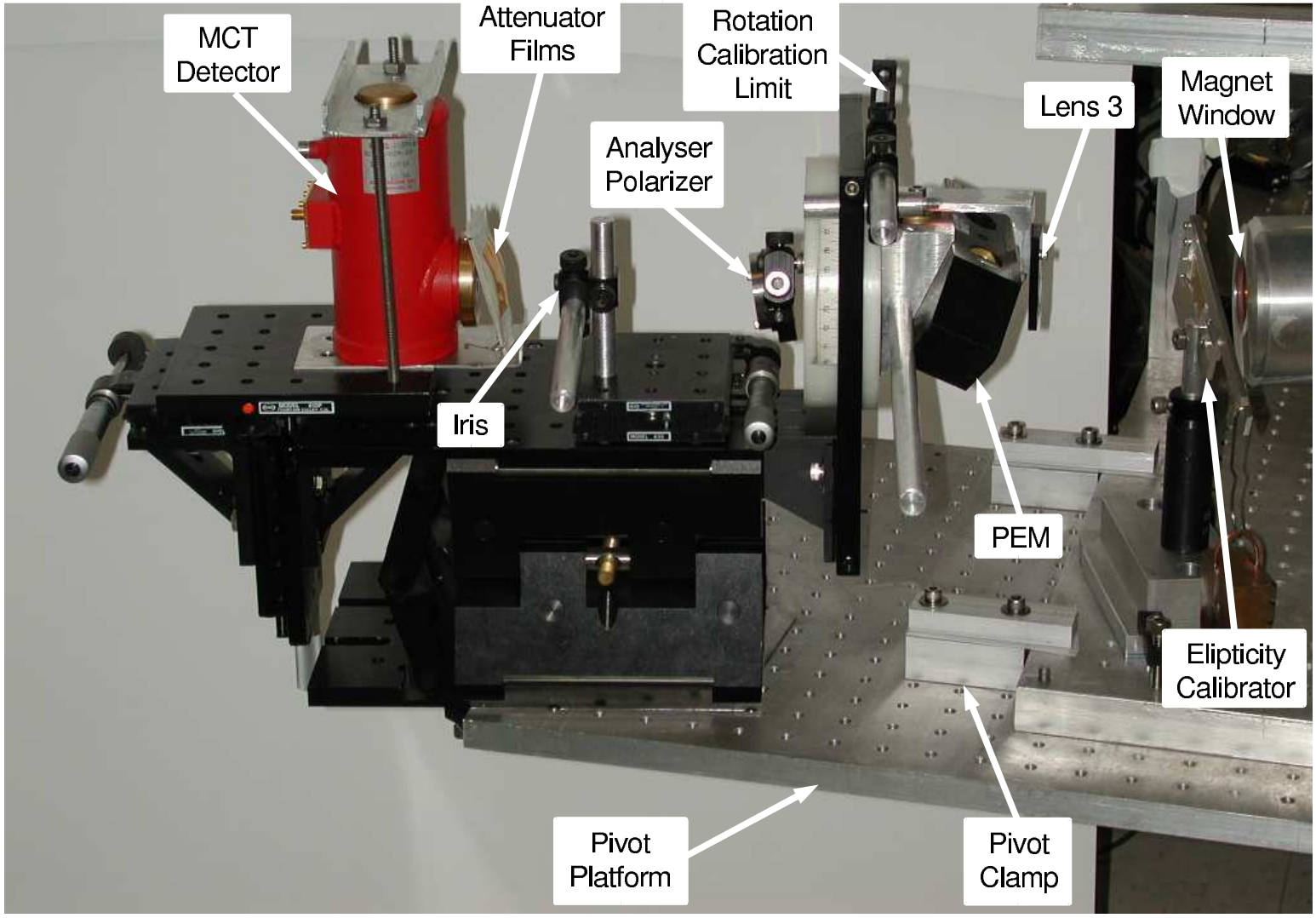

Plate 5 Optical Detection System

3 Analysis

With confusing signs and the winding prospects
Of manifold roundabout paths—

Ovid, Metamorphoses

The foregoing has likely raised at least two questions in the mind of the reader: How exactly do the lockins' outputs relate to the complex Faraday angle and how does the complex Faraday angle relate to the sample properties, e.g., conductivity?

In deriving the relationships in question we employ two formalisms. One concerns the representation and transformation of the polarization state of light and is presented in Appendix 6.1. The other formalism concerns the transmission and reflection response of multilayer stacks with complex material properties, σ, ϵ, or μ and is presented in Appendix 6.2.

3.1 Faraday Angle θ_F vs Lockin Output

For incident propagating in the z direction and polarized along the x axis, we define the real Faraday angle as

$$\tan\theta_f = \frac{t_{yx}}{t_{xx}}. \tag{14}$$

Where t_{xx} is the field transmission along the x polarization and t_{yx} is the field transmission along the y polarization.

As such it represents the amplitude in the y channel (or polarization) having been derived from the incident radiation in the x channel. It is this equation which we analytically continue in order to define the complex Faraday angle which we denote using a capital "F" subscript:

$$\theta_F = (\theta_f + i\,\theta_d) = \arctan\left(\frac{t_{yx}}{t_{xx}}\right). \tag{15}$$

For the small angles encountered in the current experiment

$$\theta_F = (\theta_f + i\,\theta_d) = \frac{t_{yx}}{t_{xx}}. \tag{16}$$

Consider next that the experimental system examines the light transmitted by the sample, which results from incident light initially polarized along the x axis (recall the z axis is the direction of propagation). A simple matrix equation represents this activity in the linear polarization basis as

$$\begin{pmatrix} t_{xx} & t_{xy} \\ t_{yx} & t_{yy} \end{pmatrix} \begin{pmatrix} x_{in} \\ 0 \end{pmatrix} = \begin{pmatrix} x_{out} \\ y_{out} \end{pmatrix}. \tag{17}$$

Assuming the a and b axes of the sample to be indistinguishable, i.e., near square symmetry, and noting that the B field is uniform and parallel to $\hat{z}$, we know that the sample transmission of equation (17) will be diagonal in the circular basis. Using the formalism in Appendix 6.1 and setting the off-diagonal elements to zero produces

$$\begin{pmatrix} t_p & 0 \\ 0 & t_n \end{pmatrix} = \begin{pmatrix} t_{xx} - i\,t_{yx} & 0 \\ 0 & t_{xx} + i\,t_{yx} \end{pmatrix} \tag{18}$$

where t_p is the transmission coefficient corresponding to positive helicity (positive $\hat{\phi}$ rotation seen at fixed point for a wave traveling in the positive z direction, and t_n is the transmission coefficient corresponding to negative helicity (negative $\hat{\phi}$ rotation seen at fixed point for a wave also traveling in the positive z direction. Transforming back to the linear basis,

$$\begin{pmatrix} t_{xx} & t_{xy} \\ t_{yx} & t_{yy} \end{pmatrix} = \begin{pmatrix} t_{xx} & -t_{yx} \\ t_{yx} & t_{xx} \end{pmatrix} \tag{19}$$

which is considerably simpler.

It is also useful to note that by definition (15) the Faraday angle relates very simply to the ratio of the transmissions of the right and left circular polarization:

$$\begin{pmatrix} \frac{t_p}{t_n} & 0 \\ 0 & \frac{t_n}{t_p} \end{pmatrix} = \begin{pmatrix} e^{-i2\theta_F} & 0 \\ 0 & e^{i2\theta_F} \end{pmatrix}. \tag{20}$$

For the purpose of developing a relation between the sample transmission and the lockin outputs consider the relevant experimental elements represented schematically as:

laser beam ⟶ sample ⟶ PEM ⟶ analyzer polarizer at an angle of 45°
⟶square-law detector ⟶lockins.

Using the polarization analysis formalism of Appendix 6.1 the first line appears as:

$$|\,\text{out}\,\rangle = R\left(\tfrac{\pi}{4}\right)\cdot\begin{pmatrix} 1 & 0 \\ 0 & 0 \end{pmatrix}\cdot R^{-1}\left(\tfrac{\pi}{4}\right)\cdot \text{PEM}\cdot\text{sample}\cdot|x\rangle$$

or, in the circular basis as

$$\begin{pmatrix} \langle p\,|\,\text{out}\,\rangle \\ \langle n\,|\,\text{out}\,\rangle \end{pmatrix} =$$

$$\begin{pmatrix} e^{-i\frac{\pi}{4}} & 0 \\ 0 & e^{i\frac{\pi}{4}} \end{pmatrix}\begin{pmatrix} 1 & 0 \\ 0 & 0 \end{pmatrix}\begin{pmatrix} e^{i\frac{\pi}{4}} & 0 \\ 0 & e^{-i\frac{\pi}{4}} \end{pmatrix}\begin{pmatrix} 1 & -i \\ 1 & i \end{pmatrix}\cdot$$

$$\begin{pmatrix} e^{i\beta\cos(\omega t)} & 0 \\ 0 & 1 \end{pmatrix}\begin{pmatrix} 1 & 1 \\ i & -i \end{pmatrix}\begin{pmatrix} e^{-i(\theta_f + i\theta_d)} & 0 \\ 0 & e^{i(\theta_f + i\theta_d)} \end{pmatrix}\begin{pmatrix} 1 & -i \\ 1 & i \end{pmatrix}\begin{pmatrix} 1 \\ 0 \end{pmatrix}$$

where $\omega = 2\pi f$ is the radial frequency of the PEM modulation and β is the modulation amplitude. The above signal is incident upon a square-law detector whose output is a voltage proportional to the square of the modulus of the amplitude of the fields:

$$\text{voltage} \propto \langle\,\text{out}\,|\,\text{out}\,\rangle \propto \text{optical power}.$$

The multiplication of these matrices along with the Bessel function expansion of $e^{i\beta\cos[2\pi f t]}$ produces

$$\theta_f = \text{re}\left(\frac{t_{yx}}{t_{xx}}\right) = -\frac{1}{4J_2(\beta)}\,\frac{\text{power}(2\omega)}{\text{power(DC)}} \tag{21}$$

$$\theta_d = \text{im}\left(\frac{t_{yx}}{t_{xx}}\right) = -\frac{1}{4J_3(\beta)}\,\frac{\text{power}(3\omega)}{\text{power(DC)}} \tag{22}$$

where $J_2(\beta)$ and $J_3(\beta)$ refer to 2nd and 3rd order Bessel functions respectively, the terms "power (2ω)" and "power (3ω)" refer to the coefficients of the Fourier terms for 2 and 3 times the PEM modulation frequency, and the term "power(DC)" refers to the coefficient of the zero frequency Fourier term which is actually 112 Hertz because of the chopper frequency. The lockin amplifier readings are actually voltages which are generated by the MCT square-law detector and are proportional to the DC, 2ω, or 3ω optical power.

3.2 Sample Properties vs. Complex Faraday Angle

The sample transmission matrix, equation (18) is diagonal in circular polarization. Thus, each circular polarization channel acts independently and may be treated as such. Indeed, by the same symmetry considerations the sample matrix representation of the conductivity tensor is also diagonal in the circular basis. In what follows we will develop an expression for the transmission of the sample-substrate combination and then separately apply this expression to each polarization channel. This will give us an expression for the indices of refraction for positive and negative helicity, N_p and N_n respectively, which are then easily related to σ_{xx} and σ_{xy}.

Figure 3 appearing earlier in section 2.1 depicts the transmission through the sample substrate combination. The input beam strikes the sample film; 83% reflects as shown, 6% propagates into the sample film and 1% emerges in the forward direction at the output side of the film. This 1% strikes the interface between the film and the BaF mounting surface. Some of this beam reflects back into the sample film and some proceeds as a beam into the BaF wedge soon reaching the BaF-air interface. Most of this beam propagates into the air eventually arriving at the detection system. Because of the wedge angle of the BaF-air interface, the small reflected portion leaves the optical path and is absorbed by strategically placed graphite slabs located on the reentrant bore tubes. All of the relevant activity above can be represented as

$$\underrightarrow{\text{air}} \mid \underleftrightarrow{\text{BSCCO}} \mid \underrightarrow{\text{BaF}} \mid \underrightarrow{\text{air}}.$$

We can further simplify this sequence by removing the output wedged interface. This is equivalent to having the detector in a medium with the same index as BaF. This clearly will have no significant effect on the Faraday angle. (The only effect is the differential reflection at the interface caused by the different indices of refraction for positive and negative helicity which is certainly negligible.) The sequence above, thus, becomes

$$\underrightarrow{\text{air}} \mid \underleftrightarrow{\text{BSCCO}} \mid \underrightarrow{\text{BaF}}.$$

The formalism for multilayer transmission presented in Appendix 6.2 represents this sequence generally as

$$(\text{sample}) \begin{pmatrix} \mathcal{E}_{\text{air},\rightarrow} \\ \mathcal{E}_{\text{air},\leftarrow} \end{pmatrix} = \begin{pmatrix} \mathcal{E}_{\text{BaF},\rightarrow} \\ 0 \end{pmatrix}. \tag{23}$$

That is, the BSCCO/BaF combination acts on the electric field vectors $\mathcal{E}_{\text{air},\rightarrow}$ and $\mathcal{E}_{\text{air},\leftarrow}$ of the incoming and reflected waves respectively on the input side producing the electric field vectors $\mathcal{E}_{\text{BaF},\rightarrow}$ and $\mathcal{E}_{\text{BaF},\leftarrow}$ of the outgoing and reflected waves on the output side where of course we have no incoming wave.

We desire only the transmission which from equation (23) is

$$\frac{\mathcal{E}_{\text{BaF},\rightarrow}}{\mathcal{E}_{\text{air},\rightarrow}} = [(\text{sample})^{-1}]_{1,1}. \tag{24}$$

Since by the second law of thermodynamics the transmission is the same for either propagation direction; a moments thought will lead one to propagate backwards to avoid taking the inverse of the BSCCO/BaF matrix.

$$(\text{sample}) \begin{pmatrix} 0 \\ \mathcal{E}_{\text{air},\leftarrow} \end{pmatrix} = \begin{pmatrix} \mathcal{E}_{\text{BaF},\rightarrow} \\ 1 \end{pmatrix}, \tag{25}$$

$$\text{transmission} = \frac{\mathcal{E}_{\text{air},\leftarrow}}{1} = \frac{1}{(\text{sample})_{2,2}}. \tag{26}$$

The multilayer formalism when applied to the film-BaF combination produces

$$\text{sample} = S_{\text{BSCCO, BaF}}\, U_{\text{BSCCO}}\, S_{\text{air,BSCCO}} \tag{27}$$

where S refers to the interface matrices and U to the propagation matrix. Equations (26) and (27) along with those in Appendix 6.2 provide a relationship between the material properties (the real and imaginary relative impedance) and the transmission, which after some manipulation yield an equation for the transmission versus index of refraction:

$$t(\text{nf}) = -\frac{4\, e^{\frac{2\, i\, d\, \text{nf}\, \pi}{\lambda}}\, \text{nBaF}\, \text{nf}}{\left(e^{\frac{4\, i\, d\, \text{nf}\, \pi}{\lambda}}\,(\text{nf}-1)-\text{nf}-1\right)\text{nf}-\text{nBaF}\left(e^{\frac{4\, i\, d\, \text{nf}\, \pi}{\lambda}}\,(\text{nf}-1)+\text{nf}+1\right)} \tag{28}$$

where nf is the index of refraction of the BSCCO film,

nBaF is the index of refraction of BaF,

d is the thickness of the BSCCO film,

and λ is the free space wavelength of the input radiation.

There is one such equation for each circular polarization channel.

Analysis of the data ultimately requires an equation for the index of refraction (or some other material property) in terms of the Faraday angle. Equation (20) with equation (28) contains the pertinent information but the combination does not lend itself to inversion. Fortunately, because the relative difference between N_p and N_n is very small, we can generate a readily invertible form by expanding their combination about either N_p or N_n. Choose $\text{nf} = N_p$. Then expanding (20) and keeping only the linear term results in

$$\theta_F = \delta N\, \frac{d}{d\, \delta N}\, \frac{i}{2} \ln\left(\frac{t(N_p)}{t(N_p+\delta N)}\right)$$

where $\delta N = N_n - N_p$ is the difference in refractive indices for negative and positive helicity as noted above and $t(N_p) = t_p$ and $t(N_p + \delta N) \approx t_p$. This is easily inverted and combined with (28) and after some manipulation simplifies to:

$$\delta N = 2\, \theta F\, N_p\, \frac{(n\, N_p + N_p) - i \tan(k\, d)\, (n + N_p^{\,2})}{k\, d\,(n + N_p^{\,2}) - \tan(k\, d)\, [n + i\, k\, d\, (1+n)\, N_p - N_p^{\,2}]} \tag{29}$$

where $\delta N = N_n - N_p$ is the difference in refractive indices for negative and positive helicity as noted above,

$k = \frac{2\pi N_p}{\lambda}$ is the propagation constant in the BSCCO film,

n is the index of refraction of BaF,

and d is the thickness of the BSCCO.

For an expression for σ_{xx} and σ_{xy} note that by the same symmetry assumed earlier $\vec{\epsilon}$ and $\vec{\sigma}$ are also diagonal in circular polarization:

$$\vec{\sigma} \doteq CL \cdot \begin{pmatrix} \sigma_{xx} & \sigma_{xy} \\ -\sigma_{xy} & \sigma_{xx} \end{pmatrix} \cdot LC = \begin{pmatrix} \sigma_{xx} + i\sigma_{xy} & 0 \\ 0 & \sigma_{xx} - i\sigma_{xy} \end{pmatrix} = \begin{pmatrix} \sigma_p & 0 \\ 0 & \sigma_n \end{pmatrix} \qquad (30)$$

To obtain the expression for σ_{xx} and σ_{xy} in terms of σ_p and σ_n we simply reverse the transform.

$$\vec{\sigma} \doteq LC \cdot \begin{pmatrix} \sigma_p & 0 \\ 0 & \sigma_n \end{pmatrix} \cdot CL = \begin{pmatrix} \frac{\sigma_n + \sigma_p}{2} & \frac{1}{2} i (\sigma_n - \sigma_p) \\ -\frac{1}{2} i (\sigma_n - \sigma_p) & \frac{\sigma_n + \sigma_p}{2} \end{pmatrix} = \begin{pmatrix} \sigma_{xx} & \sigma_{xy} \\ -\sigma_{xy} & \sigma_{xx} \end{pmatrix} \qquad (31)$$

Then, by comparison

$$\sigma_{xx} = \frac{1}{2}(\sigma_n + \sigma_p) \qquad \text{and} \qquad \sigma_{xy} = \frac{1}{2} i (\sigma_n - \sigma_p) \qquad (32)$$

Next, we need an equation involving the difference in the indices of refraction of the BSCCO film as in equation (29). From Maxwells equations

$$\sigma = -\frac{i\omega\epsilon}{4\pi} = -\frac{i\omega}{4\pi} n^2 \qquad \text{(CGS)}$$

Then, from equations (32)

$$\sigma_{xx} = -\frac{i\omega}{8\pi}(N_n^2 + N_p^2) \qquad \text{and} \qquad \sigma_{xy} = \frac{\omega}{8\pi}(N_n^2 - N_p^2)$$

$$\approx -\frac{i\omega}{4\pi} N_p^2 \qquad \text{and} \qquad \approx \delta N \frac{\omega}{4\pi} N_p$$

After substituting (29) into the above expression for σ_{xy} then, in CGS units

$$\sigma_{xy} = (\theta_f + i\theta_d) \frac{\omega (N_p)^2}{2\pi} \frac{(n N_p + N_p) - i \tan(k d)(n + N_p^2)}{k d (n + N_p^2) - \tan(k d)[n + i k d (1+n) N_p - N_p^2]} \qquad (33)$$

This expression of course requires accurate values for θ_F and θ_d. The experiment, however, introduces several systematic effects into these values, which we have ignored up to this point but, which nevertheless must be removed or compensated. The following section examines these affects and derives amended forms for equations (21) and (22) which ultimately appear below as equations (41) and (43).

3.3 Calibration

Below we will address the correction of three rather serious systematic effects ignored in the foregoing. First, the MCT detector and subsequent electronics introduce their own response functions which must be removed from the data. Second, the PEM modulation reported by the PEM electronics is frequently in error for reasons to be discussed below. Third, the Faraday angle θ_F determined by the above equations is the total Faraday angle, which includes a background amount, which results mostly from the ZnSe magnet windows and the substrate.

Regarding the response functions, equations (21) and (22) above require the ratio of the optical power in the 2nd and 3rd harmonics to the optical power at 112 Hertz (referred to as DC) at the MCT detector:

$$\frac{\text{power}(2\,\omega)}{\text{power(DC)}} \quad \text{and} \quad \frac{\text{power}(3\,\omega)}{\text{power(DC)}}$$

However, the MCT and other electronics possess frequency transfer functions which attenuate these signals by different amounts. To remove these effects divide the data sets by the responses:

$$\text{data}2\omega \, \frac{\text{ResponseDC}}{\text{Response}2\omega} \tag{34}$$

$$\text{data}3\omega \, \frac{\text{ResponseDC}}{\text{Response}3\omega} \tag{35}$$

where data2ω and data3ω are the ratios recorded during the experiment discussed above in section 2.6.

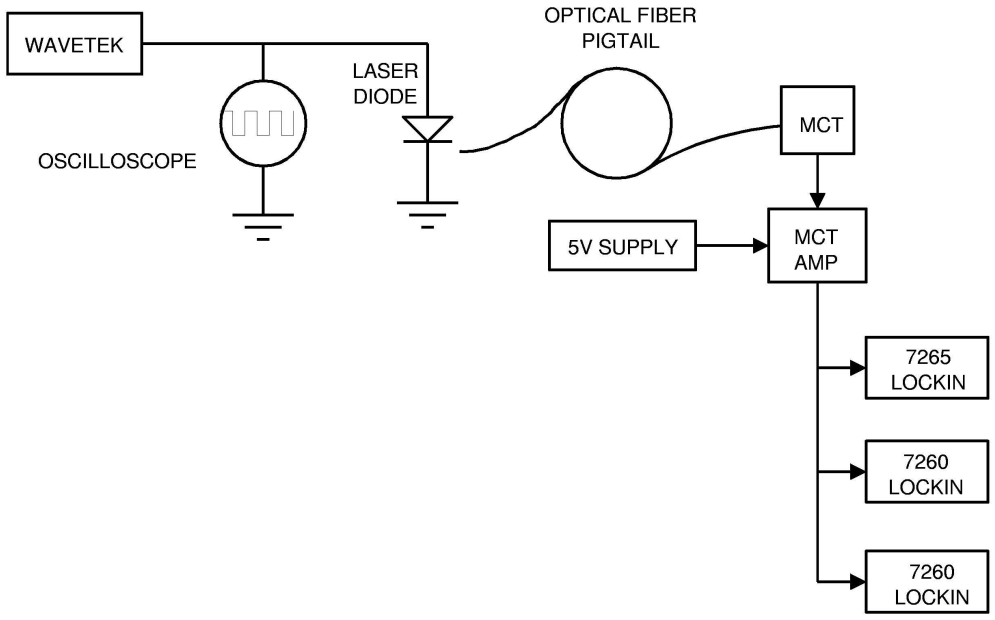

FIG. 4 Experimental arrangement for determining the equipment response. This arrangement was used to determine the responses of the MCT detector, lockin, and preamp combination.

Figure 4 depicts the experimental arrangement used to determine the above responses as a single quantity for each data channel, data2ω and data3ω. The arrangement shows a square wave signal from a wavetek signal generator, which drives a Marconi 1.5 micron laser diode, whose output is coupled to an optical fiber pigtail, which directs the light to the MCT detector. An oscilloscope monitors the signal generator to insure the output does not change as a function of output frequency. The intensity of the output light is comparable to that of our experiments at 10.6 microns, which is such as to produce approximately a 100mV RMS signal at the output of the MCT preamp. All of the lockin amplifiers are set to read the first harmonic of the preamp output. Recording the output of each lockin amplifier for each driving frequency of 112 Hz, 100kHz, and 150kHz from the Wavetek produced essentially the same results for all lockins:

$$\frac{\text{Response}2\omega}{\text{ResponseDC}} = \frac{100\,\text{kHz reading}}{112\,\text{Hz reading}} = .803$$

$$\frac{\text{Response}3\omega}{\text{ResponseDC}} = \frac{150\,\text{kHz reading}}{112\,\text{Hz reading}} = .650$$

Next consider that the 7265 measures the RMS voltage of only the 1st harmonic of the 112 Hz square wave chopped signal. To determine this correction factor we examine the relation between a square wave and its first harmonic. This entails performing an integral transform. The normalization requirement generates the inverse of the first harmonic:

$$\int_0^\tau f^{-1}(t)\, f(t)\, dt = 1$$

Therefore, to find the normalization constant N:

$$\int_0^\tau f^{-1}(t)\,\text{Sin}[\omega t]\, dt = N \int_0^\tau \text{Sin}[\omega t]\,\text{Sin}[\omega t]\, dt = 1$$

$$= N\,\frac{\tau}{2} \qquad \text{(sign dropped)}$$

$$\therefore\ f^{-1}(t) = \frac{2}{\tau}\,\text{Sin}[\omega t]$$

We now perform the integral transform to determine the first harmonic amplitude for a squarewave of peak amplitude 1.

$$\int_0^\tau f^{-1}(t)\,\text{Square Wave}\, dt = \frac{2}{\tau}\int_0^\tau \text{Sin}[\omega t]\,\text{Square Wave}\, dt$$

$$= \frac{2}{\tau}\,\frac{1}{\omega}\,4 = \frac{4}{\pi}$$

So, for a squarewave of peak amplitude 1, the output of the 7265 would be the RMS value for a sinewave of peak amplitude $4/\pi$. Because data2ω and data3ω (also recorded in RMS) were divided by the 112 Hz RMS signal, removing this effect therefore entails multiplying (34) and (35) by $4/\pi$:

$$\frac{\text{power}(2\omega)}{\text{power(DC)}} = \text{data}2\omega\ \frac{1}{.803}\ \frac{4}{\pi} \tag{36}$$

$$\frac{\text{power}(3\omega)}{\text{power(DC)}} = \text{data}3\omega\ \frac{1}{.650}\ \frac{4}{\pi} \tag{37}$$

Note also that the RMS voltage above was calculated not from peak to peak value but rather to the peak value of the square wave which is, of course, 1/2 of the full power level. As such it includes a factor of 1/2 which cancels the duty cycle factor of 1/2 which is also present in the output of the 2ω and 3ω lockin amplifiers caused by chopping.

Next, consider the PEM. The PEM electronics as supplied by the manufacturer at best only infer the amplitude of the phase modulation impressed upon the transmitted beam. This inference does not consider the path of the beam through the ZnSe interaction crystal, the ZnSe crystal temperature, nor the possible changes in coupling between the driving quartz crystals and the ZnSe interaction crystal. Equations (21) and (22), however, require an accurate knowledge of this modulation in the value of the variable β. The current experiment explores, among other things, the frequency dependence of θ_f. Because the frequency dependence is weak, its determination requires data with very high relative accuracy. In view of equations (21) and (36), another simpler method arises for obtaining θ_f which makes use of the provision for physically rotating the PEM assembly back and forth a predetermined amount as discussed above in section 2.5. Prior to collecting each data set for each laser line one rotates the PEM assembly back and forth by the predetermined amount and records the readings from the lockin amplifiers. This defines the θ_f calibration factor:

$$\text{calibration}\theta_f = \frac{\text{predetermined physical rotation}}{\text{Reading}_2 - \text{Reading}_1} \tag{38}$$

where

$$\text{Reading}_i = \frac{\text{Reading}(2\,\omega)_i}{\text{Reading}(112)_i}.$$

Subsequent to this calibration the real Faraday angle emerges from the data as

$$\theta_f = \text{data}2\omega \cdot \text{calibration}\theta_f \tag{39}$$

without the direct use of equations (21) and (36). This calibration also supplies the sign of θ_f which the electronics by itself leaves somewhat ambiguous. For the electrical connections and phase settings in the current experiment a positive θ_f produces a negative value for data2ω. Therefore, calibrationθ_f will be negative.

Because the frequency dependence of θ_d is also weak, its determination also requires data with very high relative accuracy. Equation (21) along with the rotation calibration above also afford a relative calibration for θ_d mainly for the purpose of adjusting for the small errors which result when changing laser lines. As the exact source of these errors remains uncertain this calibration is essential in order to reliably determine the correspondingly small wavelength dependence of $\theta_d(\lambda)$. The procedure entails simply comparing the actual, predetermined, physical rotation with the calculated value from equation (21) and then adjusting the value of β, the retardance until they agree. When calculating θ_d with equation (22) we use this adjusted value β_{adj} in place of that determined from the manufacturers calibration. This procedure should be performed initially, and then after each laser line change. Combining the foregoing calibration corrections (37) with (22) gives

$$\theta_d(\lambda) = -\frac{1}{\pi J_3(\beta_{adj})}\,\frac{1}{.650}\,\text{data}3\omega(\lambda) \tag{40}$$

Section 2.4 describes the ellipticity calibrator which supplies the sign for θ_d. In fact, the calculation contained in Appendix 6.3 indicates that the θ_d resulting from placing the calibrator weight upon the arm as shown in plate 4 is positive. The system, however, produces a negative result. Therefore, the 3rd harmonic lockin values must be multiplied by -1 and equation (40) becomes

$$\theta_d(\lambda) = \frac{1}{\pi J_3(\beta_{adj})}\,\frac{1}{.650}\,\text{data}3\omega(\lambda) \tag{41}$$

which serves for all wavelengths.

Finally consider the background contribution to θ_F which manifests itself as a number of terms:

$$\theta_F(\text{background}) = \theta_0 + \theta_1 \, B + \theta_2 \, B^2 + ...$$

where the coefficients θ_i may have a wavelength dependence. In the current work the data sets contain θ_F as a function of magnetic field which is, for example, scanned from +8 to -8 Tesla or vice versa. From this data we compute the slope $\partial\theta_F / \partial B$ which obviously does not contain θ_0. Further, because the magnetic field values are both positive and negative, computation of the average slope eliminates all terms even in B. Removing the remaining odd terms requires direct measurement of the background using the background sample disc shown in Fig. 2 and plate 3 followed by simple subtraction of the result from the data sets. The background sample disc is a piece of 2° wedged BaF having the same thickness as that which holds the BSCCO film. The determination of θ_F is detailed in Appendix 6.4 and includes the background caused by the ZnSe windows. The result is

$$\begin{aligned} \theta_F(\text{background}) &= \theta_f(\text{background}) \\ &= (-0.0000113525 + 1.05565 \times 10^{-10} \, \omega^2) \, B \end{aligned} \tag{42}$$

where θ is in radians, ω is in cm^{-1}, and B is in Tesla. There is no significant θ_d background contribution nor any perceptible temperature dependence. This is consistent with the absence of free carriers in ZnSe and BaF. The final expression for the real part of the Faraday of the sample is, therefore,

$$\theta_f = \text{data}2\omega \cdot \text{calibration}\theta_f - (-0.0000113525 + 1.05565 \times 10^{-10} \, \omega^2) \, B \tag{43}$$

These equations, (41) and (43), are the amended forms for equations (21) and (22).

4 Discussion of Results

...But know that in the soul
Are many lesser faculties, that serve
Reason as chief. Among these Fancy next
Her office holds; of all external things,
Which the five watchful senses represent,
She forms imaginations, aerie shapes,

Paradise Lost

Having completed the lengthy preamble explaining the relevance of the data and the experimental method by which it was produced, let us now turn to the results of the measurements themselves. The first item to be addressed is the suitability of the sample as a representative of the general properties of single crystal $Bi_2Sr_2Ca_1Cu_2O_8$. The sample was cleaved or, rather, peeled by D. Romero of the Laboratory for Physical Sciences, University of Maryland, College Park, MD from a single bulk crystal grown by G. D. Gu of the Department of Physics, Brookhaven National Laboratory, Upton, NY. Infrared conductivity data from measurements performed by J. J. Tu (also of the Department of Physics, Brookhaven National Laboratory) on bulk crystals from this batch indicate the batch to be of high quality [28]. These data supplied the real and imaginary parts of σ_{xx} which were used in the analysis of the data in the current work.

The peeling process relies on the easy cleavage between the Bi-O planes marked in Fig 1. The process is as follows. First one cleaves the bulk crystal and fastens it cleaved-surface-down onto a surface plate using a thin film of nail polish. Next, one uses adhesive tape to peel away layer after layer until the crystal film remaining on the substrate is the desired thickness. Finally, using acetone one floats this crystal film off of the surface plate and onto the transmission substrate where it remains mostly due to van der Waals forces. A plot of the AC magnetic susceptance measurements shown Fig. 5 confirm the quality of the resulting peeled segment used in

the current work. It reveals a most precipitous drop with less than 1K width and a T_c of 92 K. This measurement was performed after all of the Hall measurements of the current work had been completed and therefore certainly establishes the integrity of the sample and recommend the Hall data as representative of optimally doped BSCCO.

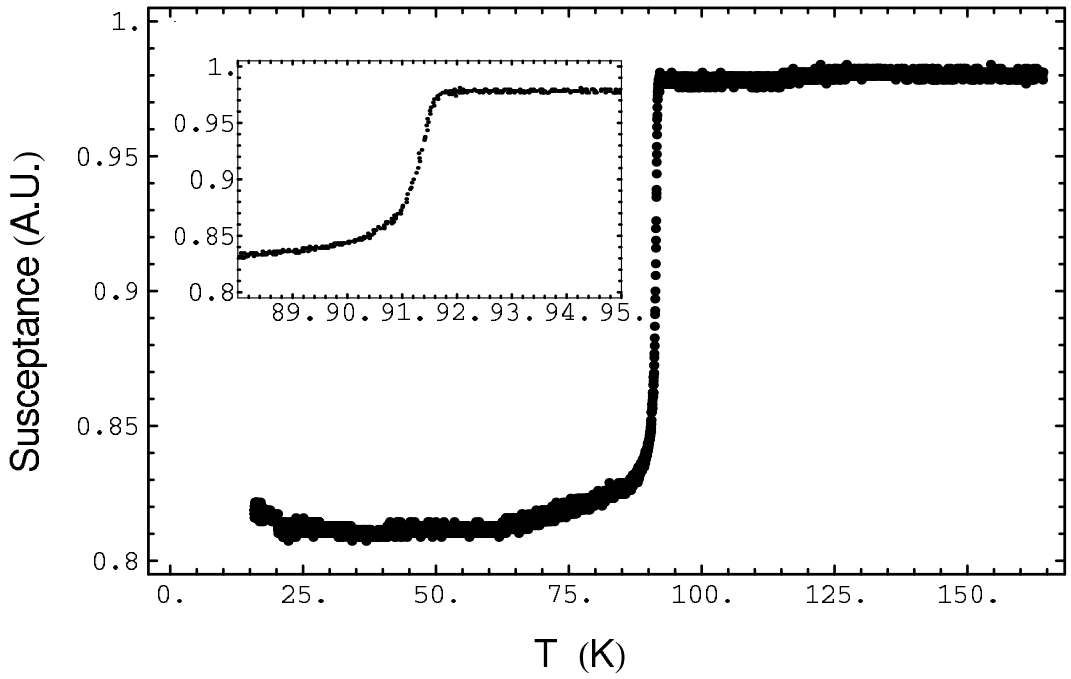

FIG. 5 The susceptance in arbitrary units vs. temperature for 2212 BSCCO.

The last information required of the sample before proceeding is the thickness. Because of the micaceous nature of the sample material, a direct physical measurement of the thickness is no simple task. Further, such a measurement would destroy most of the sample, which at the time of this writing remains intact for further study. Rather, the value of the thickness used here issues by inference from transmission measurements at 10.6 μm with the help of equation (28). Assuming the sample to be uniform in character, the inferred thickness is 205±3 nm. Later we will visit the effects caused by violations of this assumption.

The Hall measurements of the current work include the response of the sample

to input radiation from 920 to 1090 cm^{-1} and over a temperature range from 30 to 330 K in an external B field ranging from -8 to $+8$ Tesla. This response manifests as a complex Faraday angle as explained in section 3 and as calculated from the raw data using equations (41) and (43). Figure 6 depicts an example of such a response versus temperature. This response is not too unlike the Hall angle with which it may be compared (see for example Fig. 13). In the following sections the complex Faraday measurements, by means of equation (33), along with the forementioned conductivity data will yield various material properties including σ_{xy}, θ_H and $\theta_H{}^{-1}$, R_H, and also ω_H and γ_H by additionally fitting the data to an extended Drude model. Finally, we shall visit the implications of the relevant sum rules.

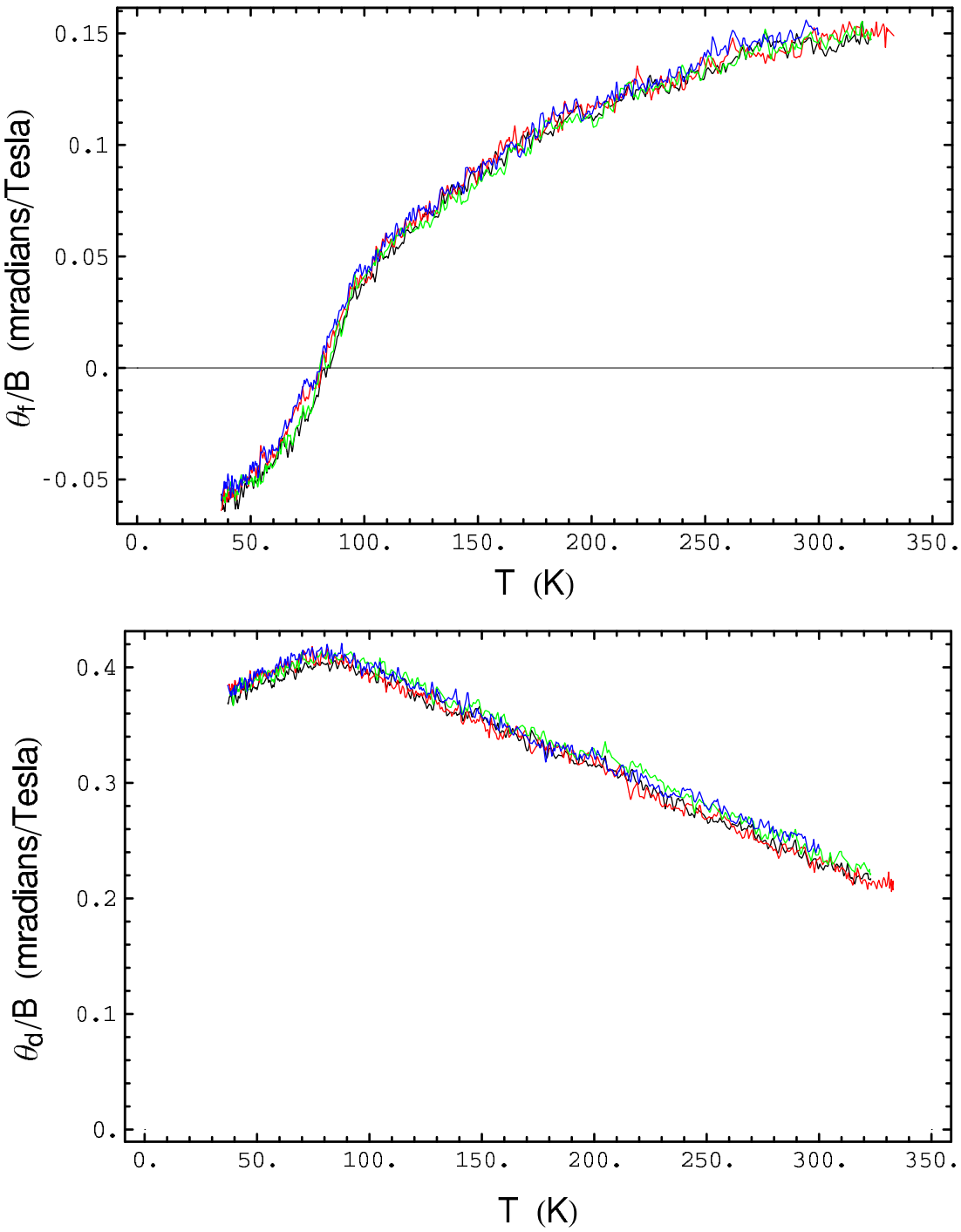

FIG. 6 The real part of the Faraday angle (upper) and the imaginary part of the Faraday angle (lower) each per Tesla and versus temperature for 2212 BSCCO measured at 950 cm^{-1}. Each color represents a different subtracted pair of temperature scans. There are four pairs total in each graph.

4.1 σ_{xx} and σ_{xy}

To obtain the transverse conductivity σ_{xy} equation (33) requires the index of refraction. This is easily calculated from σ_{xx} using

$$\sigma_{xx} \approx -\frac{i\omega}{4\pi} N_p^2 \qquad \text{(CGS)}$$

where N_p is the index of refraction of the sample for positive helicity. Figures 7 and 8 depict σ_{xx} measured in the AB plane. These graphs are adapted from the earlier mentioned measurements performed by J. J. Tu [28] upon bulk crystals from the same batch whence came the current sample. The results agree closely with data by Quijada [5] on other single crystal 2212 BSCCO. Neither work indicates any significant difference between the a and b directions for wavelengths around 10.5 microns, so no differentiation is made below. It is interesting to note that the figures show very little temperature dependence for σ_{xx} in the mid-infrared.

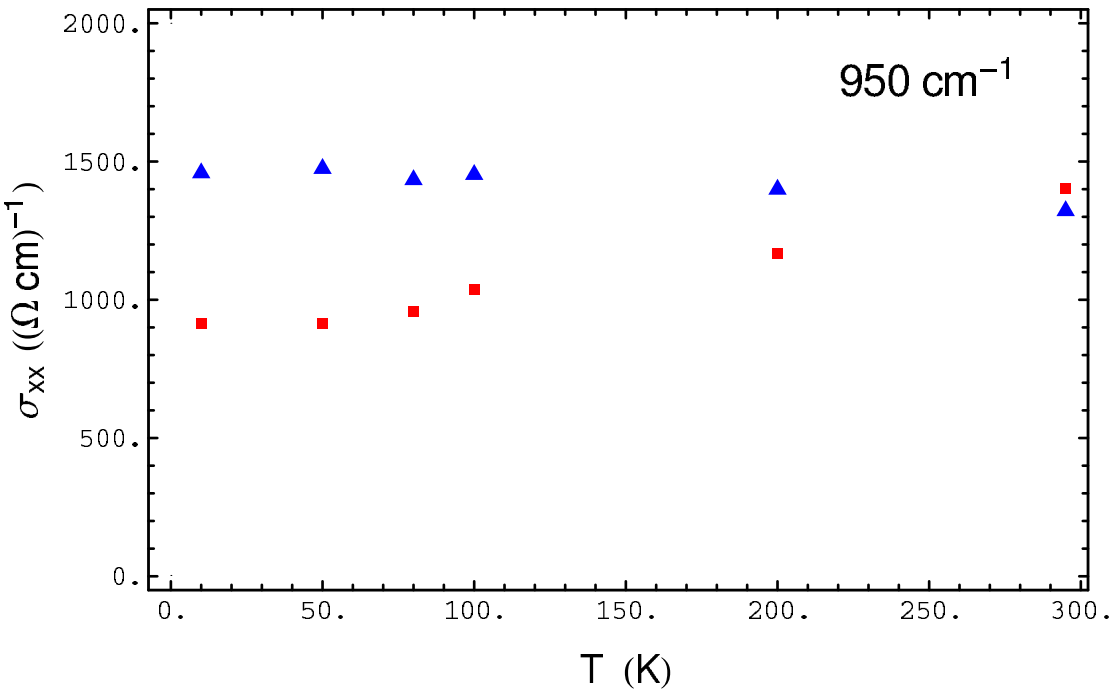

FIG. 7 σ_{xx} vs. sample temperature for 2212 BSCCO at 950 cm^{-1}. The red squares represent Re(σ_{xx}) and the blue triangles represent Im(σ_{xx}). Adapted from measurements performed by J. J. Tu [28].

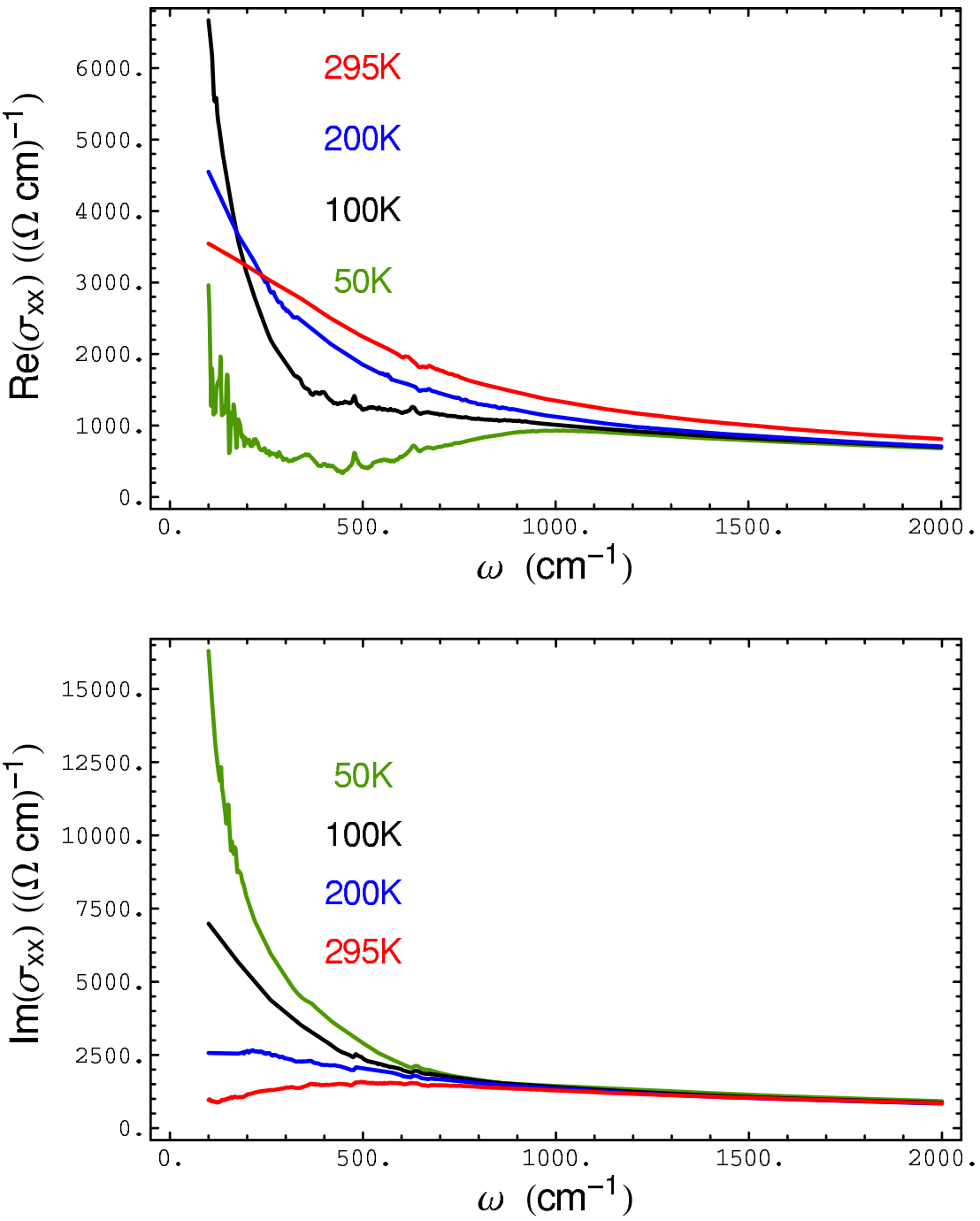

FIG. 8 The real part of σ_{xx} (upper) and the imaginary part of σ_{xx} (lower) both vs. frequency for 2212 BSCCO. Measurements performed by J. J. Tu [28].

The transverse conductivity σ_{xy} is shown in Fig. 9 for discrete frequencies from 920 to 1090 cm^{-1} at two temperatures, 35 K and 300 K. It should be noted that in

this plot and indeed in all subsequent plots for discrete frequencies at 300 K there are four data points at each frequency 920 and 1090 cm^{-1} and two data points at each of the other frequencies. Each of these points results from holding the sample temperature constant and ramping the magnetic field at a constant rate of 0.82 Tesla/min. from ±8 to ∓8 Tesla and measuring the average slope of the response. This ramping, balanced about zero Tesla, eliminates extraneous influences such as motion caused by induced dipole forces and all other influences which are even with magnetic field. Furthermore, to reduce hysteretic influences, which are odd with field, each frequency includes the same number of up and down magnetic field ramps. These slopes were then corrected using equations (41) and (43), and the plotted points finally emerge from the corrected slopes through equation (33) and the σ_{xx} data of Figs. 7 and 8.

Returning to Fig. 9, the real part of σ_{xy} at 300 K equals approximately -0.16 (Ohm cm Tesla)$^{-1}$ and is essentially frequency independent unlike that at 35 K, which is below T_c. The imaginary part exhibits an average value of about 0.45 (Ohm cm Tesla)$^{-1}$ and decreases with frequency as $\omega^{-1.2}$. This compares with the blue line in each graph corresponding to a Drude model with $\omega_p = 11000\,cm^{-1}$, cyclotron frequency $\omega_c = 0.27\,cm^{-1}$ at 1 Tesla, and a scattering rate $\gamma = 480\,cm^{-1}$. The values for the cyclotron frequency and scattering rate are taken from fits discussed below in section 4.3.

The nearly opposite behavior with frequency of the superconducting state was unanticipated in the current work, which is concerned with the normal state characteristics. Certainly one expects the imaginary part of σ_{xy}, which represents the losses, to decrease as we venture into the superconducting region. Here the quasiparticles condense into a near delta function about zero and create vortices with a number of resonances also very near zero frequency. However, the strong frequency

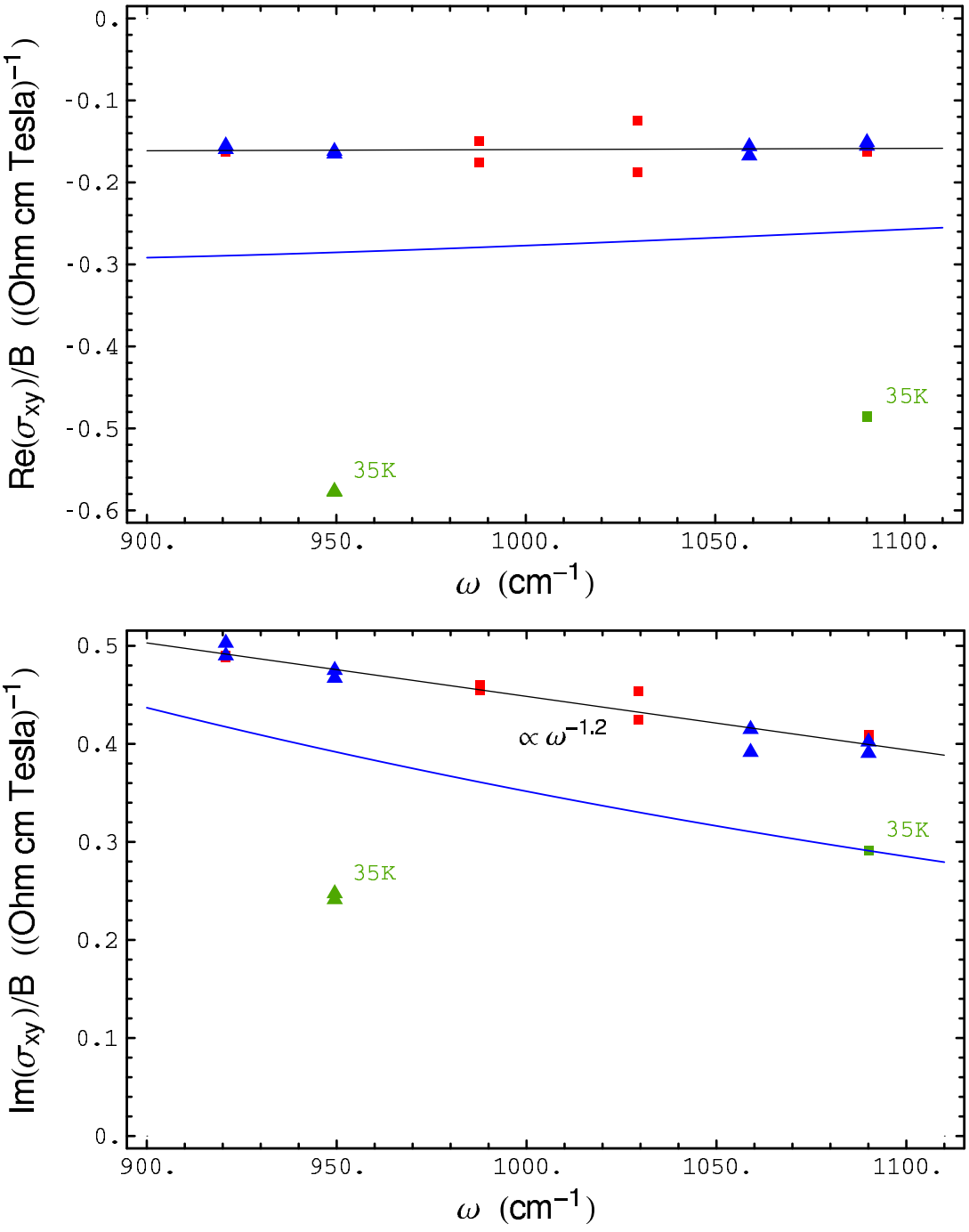

FIG. 9 The real part of σ_{xy} / Tesla (upper) and the imaginary part of σ_{xy} / Tesla (lower) for 2212 BSCCO, each versus frequency. The squares represent data set BSCCOBaFBScan083101.dat and the triangles represent data set BSCCOBaFBScan090201a.dat. The data correspond to a sample temperature of near 300K except for those points marked otherwise. There are twenty data points in each plot. The blue line corresponds to a Drude model with $\omega_p = 11000\,\mathrm{cm}^{-1}$, $\omega_c = 0.27\,\mathrm{cm}^{-1}$ at 1 Tesla, and $\gamma = 480\,\mathrm{cm}^{-1}$. The black line is a linear fit to the data along with its frequency dependence in black lettering.

dependence of this drop begs more study.

Figure 10 displays the real and imaginary part of σ_{xy} versus temperature at 950 cm^{-1}. The data of this graph are generated by maintaining the magnetic field constant at 8 Tesla and recording the response while ramping the temperature up and down. As above, this first result is corrected using equations (41) and (43). This is repeated for a magnetic field of −8 Tesla. The two resulting corrected responses are subtracted and when divided by $8 - (-8) = 16$ Tesla produce the real and imaginary part of the slope, θ_F / Tesla. Then equation (33) is used to convert θ_F to σ_{xy} for each temperature. This process performed four times produced the four plots in each graph. The curves, each corresponding to a pair of scans, are somewhat distinguishable by their color.

Clearly, the results demonstrate reproducibility. The real part of σ_{xy} exhibits an almost linear change, becoming less negative with temperature. This is quite different from the behavior for σ_{xx} shown above, which displays little temperature dependence at 1000 cm^{-1}. It is also unlike the T^{-3} behavior of σ_{yx} at DC of Chien [11] or the low frequency behavior reported by Grayson [17]. The imaginary part of σ_{xy} is somewhat flat at around 0.45 $(\text{Ohms cm Tesla})^{-1}$ for temperatures in the normal state. Note also that Fig. 10, after multiplying by 8 Tesla to equate the scales, is very much like Fig. 1 of Cerne [15]. This is a bit surprising when one considers that the sample examined by Cerne was a twinned film of YBCO. But, as it is surprising, it is also encouraging in its indication of the universal nature of the Hall conduction for the cuprates. Finally, we see in the figure the expected drop of the imaginary part as the temperature drops below T_c as discussed earlier.

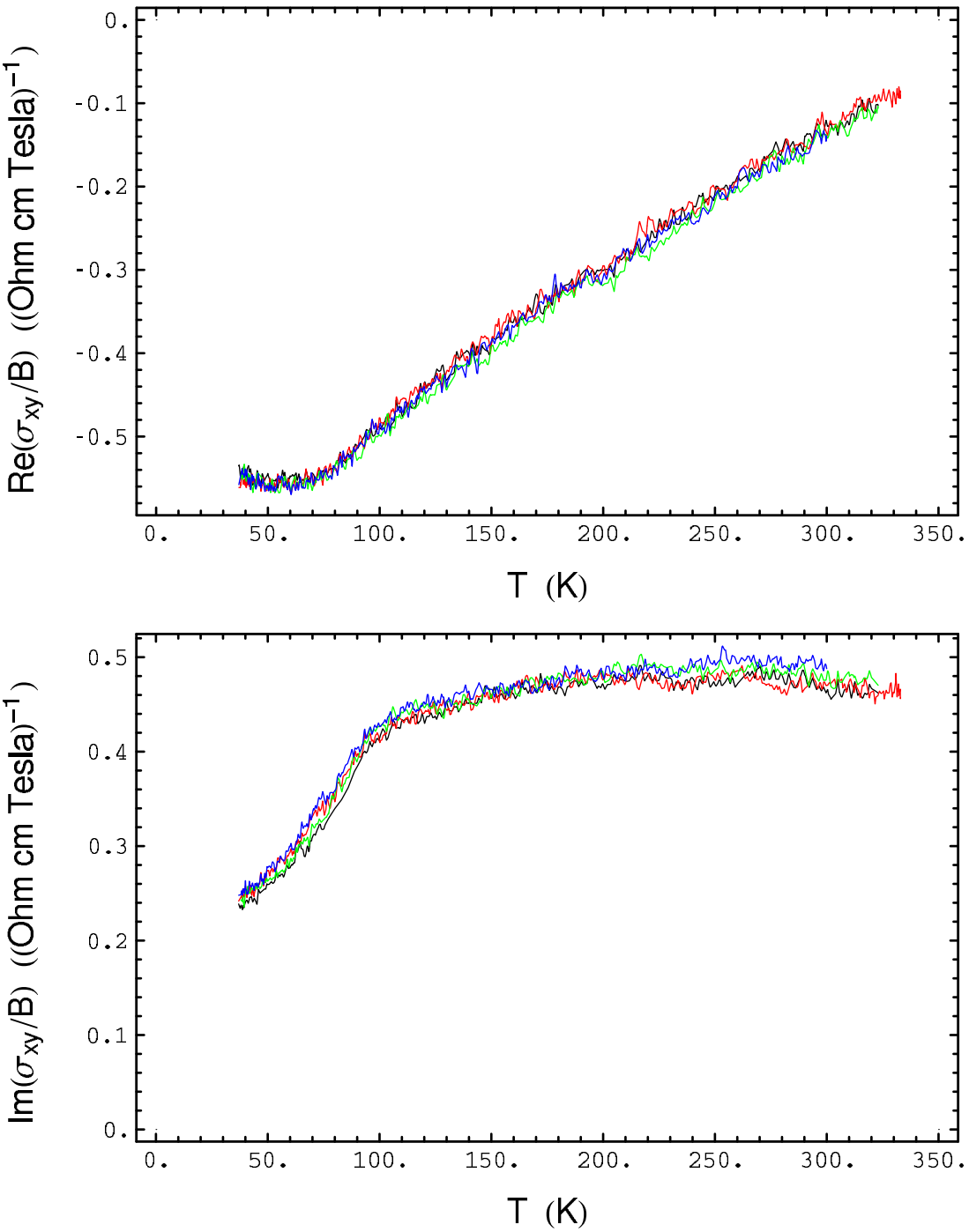

FIG. 10 The real part of σ_{xy} / Tesla (upper) and the imaginary part of σ_{xy} / Tesla (lower) versus temperature for 2212 BSCCO. Each color represents a different subtracted pair of temperature scans corresponding to a laser frequency of 950 cm^{-1}. There are four pairs in each graph.

For comparison Fig. 11 displays the results for the σ_{xy} frequency data for the current work along with the far-infrared results of Grayson and several Drude forms fitted by adjusting the scattering rates to follow a $\sim T^{1.5}$ behavior. Both real and imaginary parts of σ_{xy} of the current work would seem to line up rather well with simple extensions from the far-infrared results except, of course, for the temperature dependence already discussed. The real part of σ_{xy} for the data of the current work is negative and nearly linearly increasing with temperature, whereas the imaginary part is nearly temperature independent in the normal state. However, following both Chien and Grayson, who encourage us to examine the Hall angle rather than σ_{xy} (which in Anderson's model may be confused with a factor τ_{tr} related to longitudinal scattering) let us proceed to such in the next section.

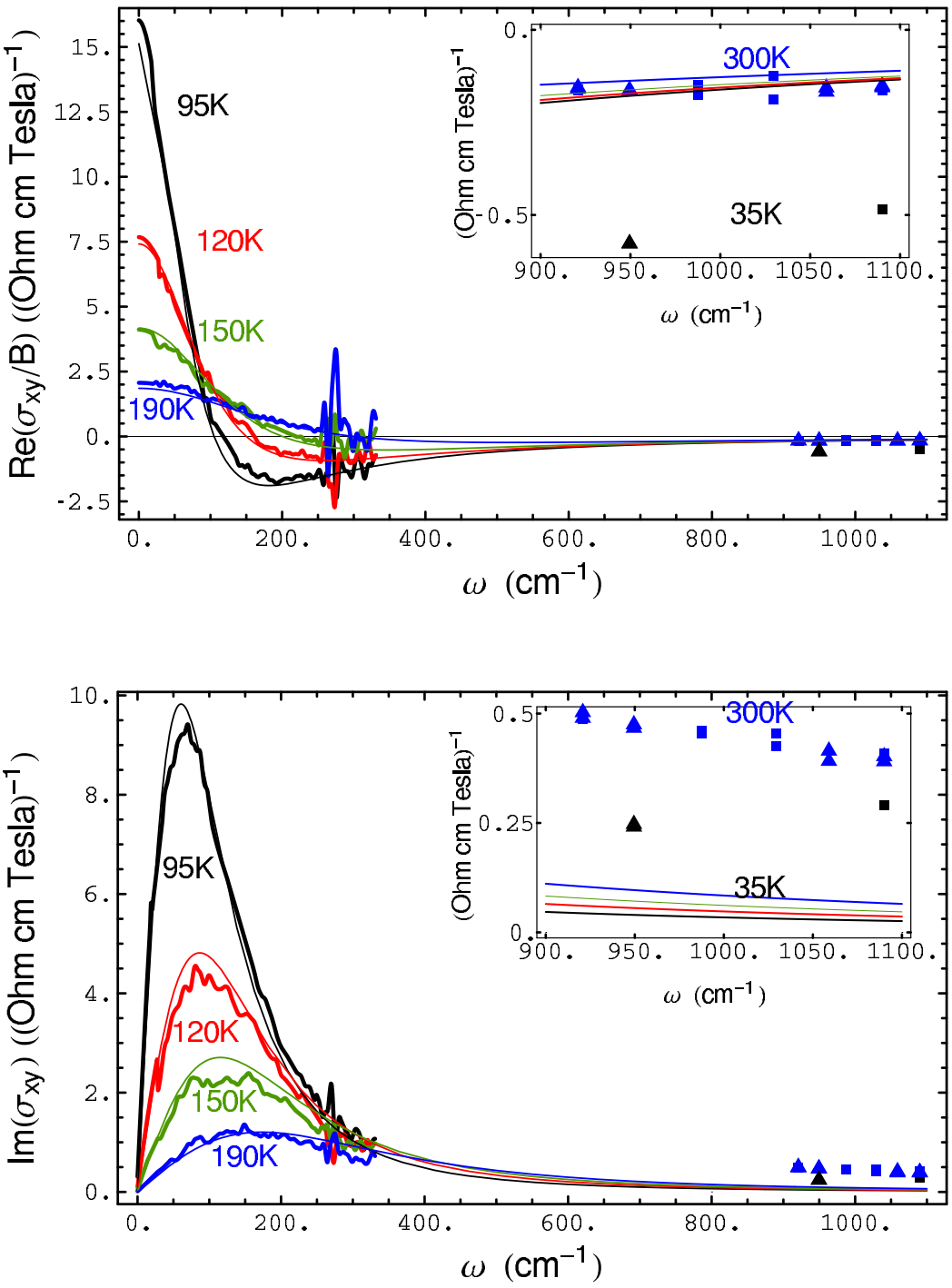

FIG. 11 $\mathrm{Re}(\sigma_{xy})/\mathrm{Tesla}$ (upper) and $\mathrm{Im}(\sigma_{xy})/\mathrm{Tesla}$ (lower) vs. frequency. Grayson *et al.* [17] provided the far-infrared data below 400 cm^{-1}. The data of the current work, which are centered about 1000 cm^{-1} also appear in the inset with expanded axes. The smooth thin lines represent simple Drude forms fitted by adjusting the scattering rate. The final parameters are: $\omega_p = 9000\,\mathrm{cm}^{-1}$, $\omega_c = 0.12\,\mathrm{cm}^{-1}$ at 1 Tesla, and $\gamma = 105,\ 150,\ 200,$ and $300\,\mathrm{cm}^{-1}$.

4.2 θ_H and $(\theta_H)^{-1}$

To form θ_H one would usually divide σ_{xy} by the value of σ_{xx} corresponding to the same temperature and frequency. But here, we wish to examine that part of the Hall angle related to the "free carriers." Interband transitions which are on the order of ~1 volt contribute essentially nothing to σ_{xy}. However, we must remove their somewhat more substantial contribution to σ_{xx} before taking the ratio. In CGS units

$$\epsilon_{total} = \epsilon_{bound} + i\,\frac{4\pi\sigma_{free}}{\omega}$$

$$= i\,\frac{4\pi\sigma_{total}}{\omega}$$

Therefore,

$$\sigma_{free} = \left(\sigma_{total} + \frac{i\omega\epsilon_{bound}}{4\pi}\right) \qquad \text{CGS} \qquad (44)$$

For ϵ_{bound} we will use the value $\epsilon_\infty = 4.6$ from Quijada [7].

Figure 12 displays the resulting values of θ_H versus frequency. Clearly, both real and imaginary parts are decreasing with frequency. Here, we are fascinated with a nearly Drude behavior for both real and imaginary parts. Also in the figure we see the curiously different slope at 35 K, which is below T_c, but this time it occurs only for the real part. The imaginary part displays much less frequency dependence than the real part. Its average value is approximately twice that of the real part. Recall that for a Drude model the phase of the Hall angle (the ratio of the imaginary to the real part) equals ω/γ. We shall see below that this is in agreement with the scattering rate of 500 cm^{-1} at 300 K, which results when the data is analyzed as a Drude form.

Figure 13 displays the values of θ_H versus temperature. The real part of θ_H increases with temperature but appears to saturate around 300 K. Note that the real part of the Hall angle is positive for all temperatures in the normal state.

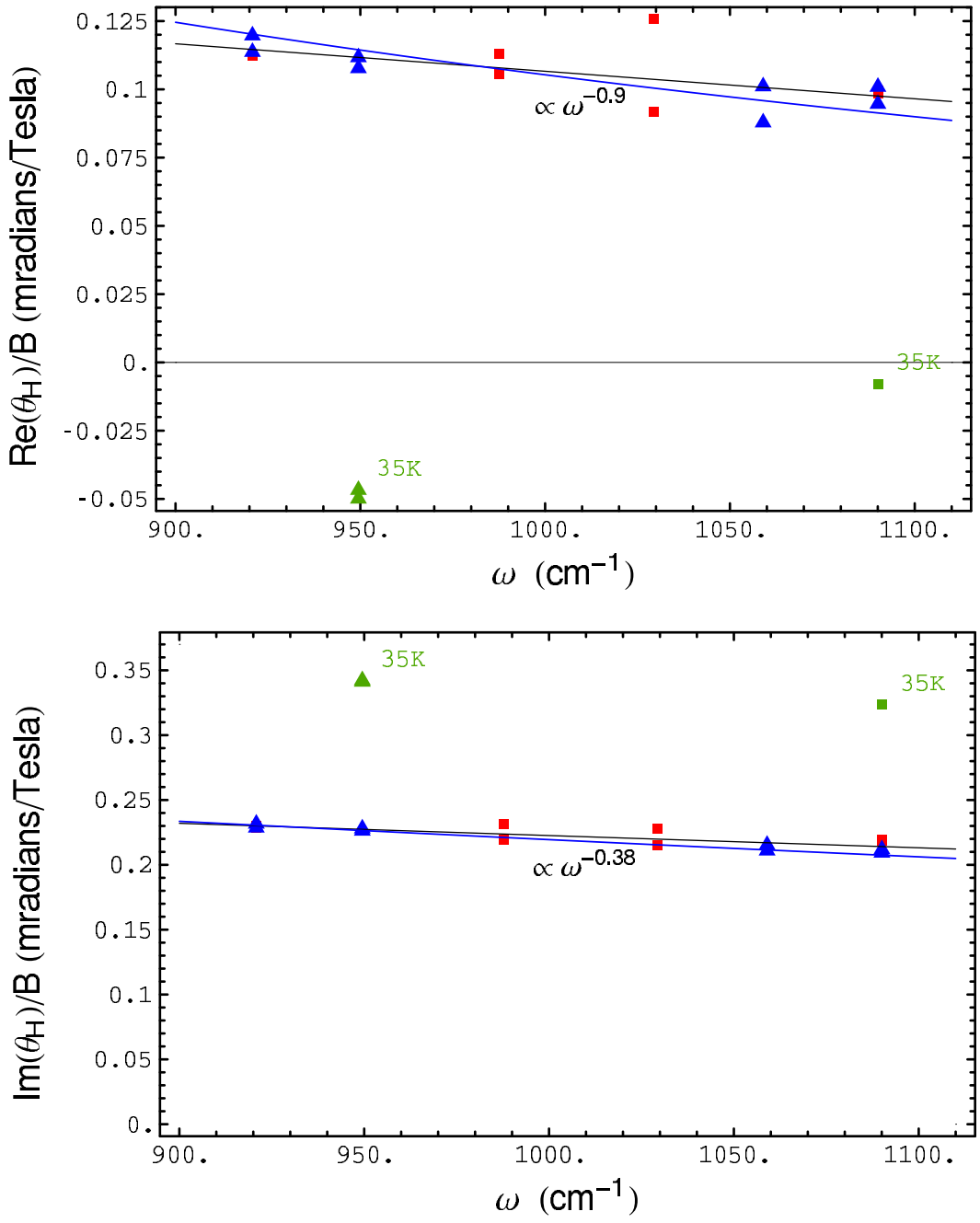

FIG. 12 The real part of θ_H /Tesla (upper) and the imaginary part of θ_H /Tesla (lower) for 2212 BSCCO, each versus frequency. The squares represent data set BSCCOBaFBScan083101.dat and the triangles represent data set BSCCOBaFBScan090201a.dat. The data correspond to a sample temperature of near 300K except for those points marked otherwise. There are twenty data points in each plot. The blue line corresponds to a Drude model with $\omega_p = 11000\,\mathrm{cm}^{-1}$, $\omega_c = 0.27\,\mathrm{cm}^{-1}$ at 1 Tesla, and $\gamma = 480\,\mathrm{cm}^{-1}$. The black line is a linear fit to the data along with its frequency dependence in black lettering.

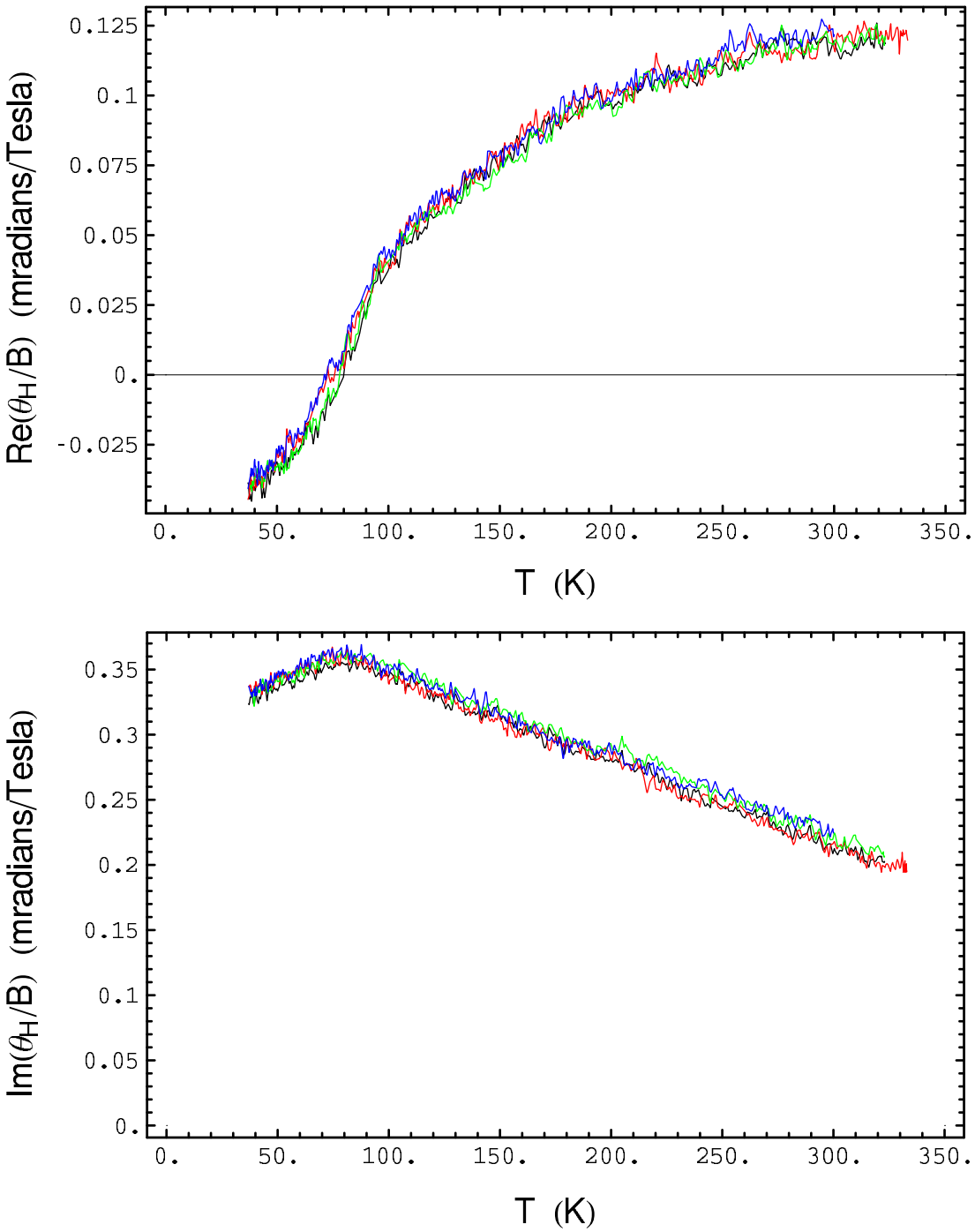

FIG. 13 The real part of θ_H / Tesla (upper) and the imaginary part of θ_H / Tesla (lower) vs. temperature for 2212 BSCCO. Each color represents a different subtracted pair of temperature scans all corresponding to a laser frequency of 950 cm^{-1}. There are four pairs in each graph.

The imaginary part of the Hall angle is decreasing with temperature in a very linear fashion. Keeping these dependences in mind let us now compare these with the far-infrared data of Grayson in Fig. 14.

In Fig. 14 we observe a disconnect between the behavior of the far- and mid-infrared Hall angle some of which is perhaps due to the fact that we are comparing the results of two different materials. Starting at about 230 cm^{-1} the real part of the Hall angle for low temperatures appears to be negative. However, as noted above it is certainly positive in the mid-infrared. The temperature dependence of the far-infrared data changes sign at around 150 cm^{-1}, which then agrees with that of the mid-infrared. The temperature dependence of the imaginary part of the Hall angle of the far-infrared data is decreasing with frequency so as to become more similar to that of the mid-infrared. The fit of the AC extended version of the model of Varma and Abrahams, shown as blue lines, accommodates the far-infrared results well. However, the extension of the real part into the mid-infrared remains negative unlike the data which are positive. The fit to the imaginary part displays essentially zero temperature dependence in the mid-infrared whereas the data display a linear dependence.

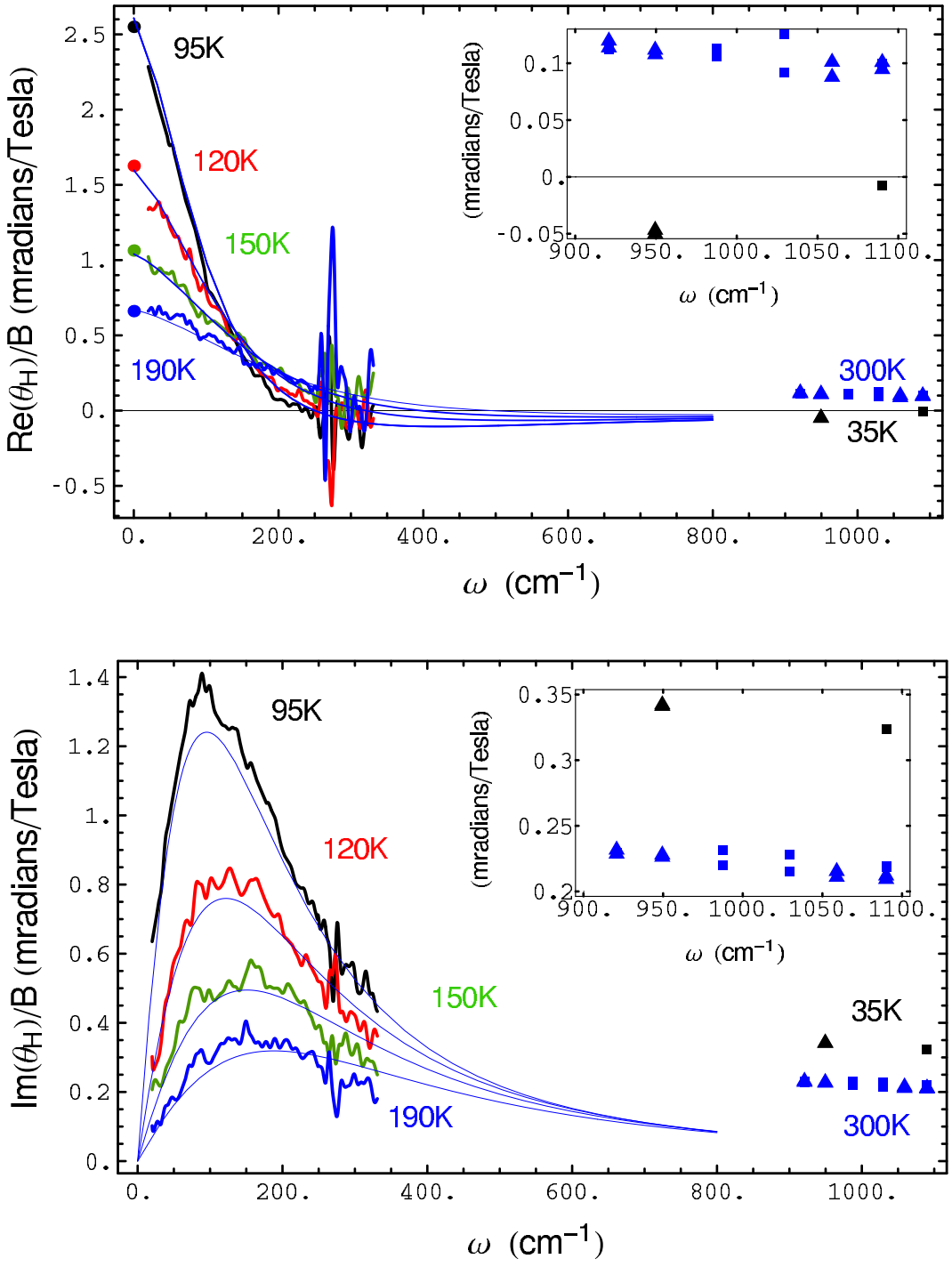

FIG. 14 $\mathrm{Re}(\theta_H)/\mathrm{Tesla}$ (upper) and $\mathrm{Im}(\theta_H)/\mathrm{Tesla}$ (lower) vs. frequency. The far-infrared data, which are below 400 cm^{-1}, along with the squared Lorenztian fit based on the Varma Abrahams model is taken from Grayson [17]. The data of the current work are centered about 1000 cm^{-1} and also appear in the inset with the axes expanded.

The Yakovenko model, which employs two Drude terms, appears in Fig. 15 along with the data. This model had been assembled to address only low frequency properties. Notwithstanding, let us extend it into the mid-infrared in the figure for comparison. This model permits adjustment by six separate parameters. The set of parameters used in the figure were supplied by Zheleznyak [24] and had been generated to fit infrared transmission data, the single temperature Hall data of Kaplan [14], and the Fermi surface. They are

$$\sigma_{xx} = \frac{\omega_p{}^2}{4\pi}(a_1\,\tau_1 + a_2\,\tau_2) \tag{45}$$

and

$$\sigma_{xy} = \frac{\omega_H\,\omega_p{}^2}{4\pi}(b_1\,\tau_1{}^2 + b_2\,\tau_2{}^2)$$

where

$$a_1 + a_2 = 1$$

$$b_1 + b_2 = 1$$

$$a_1 = 0.9$$

$$b_1 = 0.71 \tag{46}$$

$$\frac{1}{\tau_1} = 4.5\,\mathrm{T} - i\,\omega$$

and

$$\frac{1}{\tau_2} = 4.5\,\frac{\mathrm{T}^2}{82.5\,\mathrm{K}} - i\,\omega$$

where the τ's are to be extended as $1/\tau \rightarrow (1/\tau) - i\,\omega$. Even without any additional adjustment the model agrees qualitatively with the data except for the deep plunge of the real part at 250 cm^{-1} and the temperature dependence in the mid-infrared, for which it was not designed.

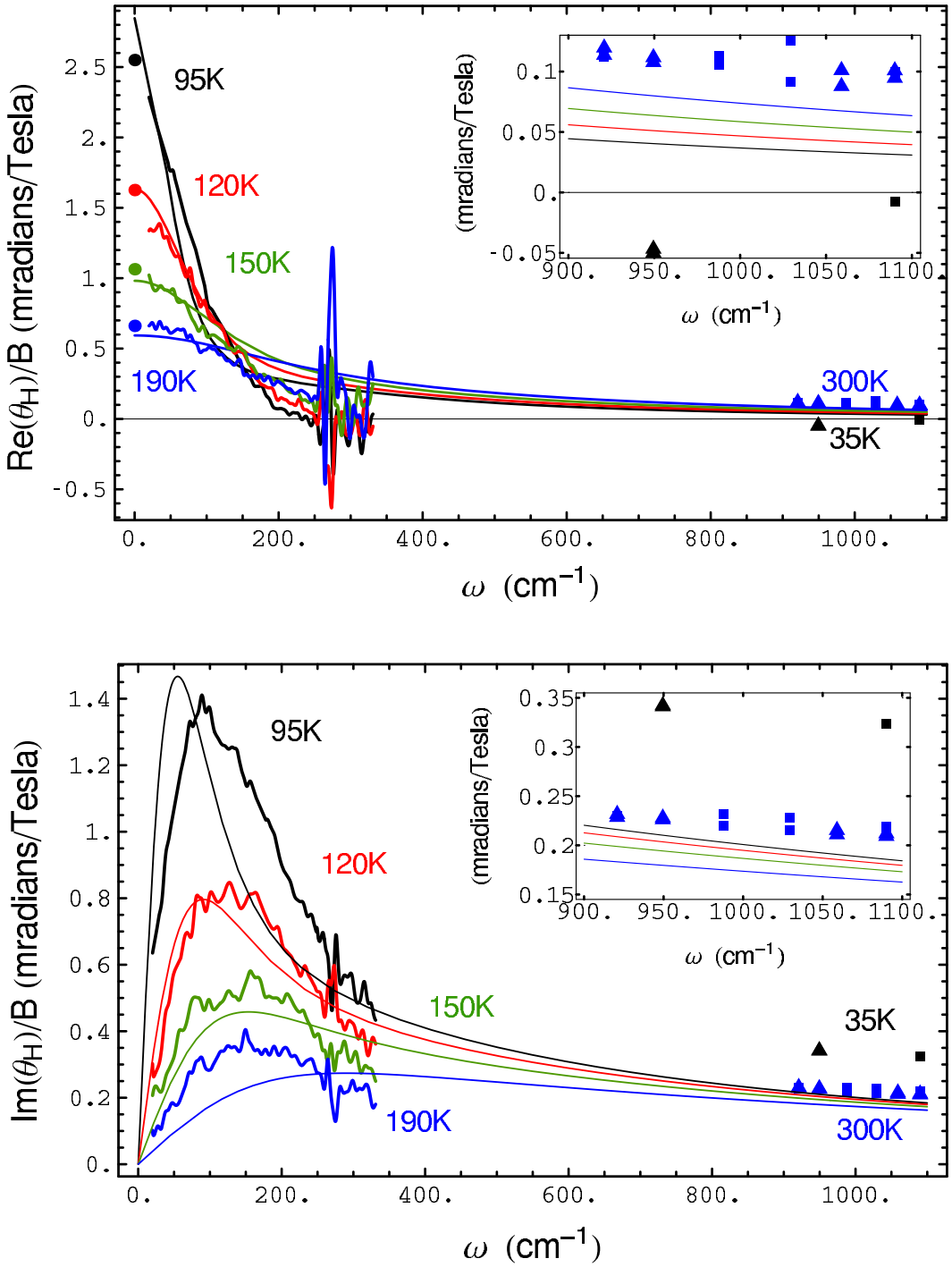

FIG. 15 Re(θ_H)/Tesla (upper) and Im(θ_H)/Tesla (lower) vs. frequency. The far-infrared data, which are below 400 cm^{-1}, are taken from Grayson [17]. The smooth thin lines are fits using the Yakovenko model with the same parameters assembled in Zheleznyak [24]. The data of the current work are centered about 1000 cm^{-1} and also appear in the inset with expanded axes.

The Ioffe-Millis model produces a simple Drude form with a T^2 scattering rate for the Hall angle. As we have seen, a Drude model cannot produce the deep plunge at 300 cm^{-1}, nor can it produce the proper temperature dependence for the mid-infrared. In the upper plot of Fig. 16 the prediction of the model matches the DC results but as the frequency increases it fails to follow the quickly falling response. Continuing into the mid-infrared, the model displays nearly a squared temperature dependence whereas in Fig. 13 the data appears rather to be approaching saturation at higher temperatures. To see the problem clearly examine the plot of the model and data expressed as the inverse Hall angle in Fig. 17. The upper plot of Fig. 17 illustrates the frequency independence of the real part of the inverse Hall angle of a Drude model, which equals $1/\omega_c \tau$ —a constant. The far-infrared data, however, displays a pronounced decrease with frequency, which for the 95K appears about to become negative. Furthermore, the model simply carries the $\sim T^2$ DC temperature dependence of the real part into the mid-infrared range. However, as we shall see below the temperature dependence in the mid-infrared is almost linear. The lower plot of Fig. 17 illustrates the temperature dependence of the imaginary part of the inverse Hall angle which is proportional to the negative of the Hall mass. For the Drude model there is no temperature dependence and all the curves are coincident and are shown as the single, straight, thin blue line. But, the temperature dependence of the far-infrared inverse Hall angle is undeniable. As we shall see later in equation (47), this would indicate a Hall mass increasing with temperature. In fact, the low frequency, far-infrared data when analyzed with the extended Drude form suggest that both the scattering rate $\gamma = 1/\tau$ and the inverse of the Hall frequency ω_H increase linearly with temperature dependence and conspire to produce the approximate $\sim T^2$ behavior of the inverse Hall angle dependence for DC.

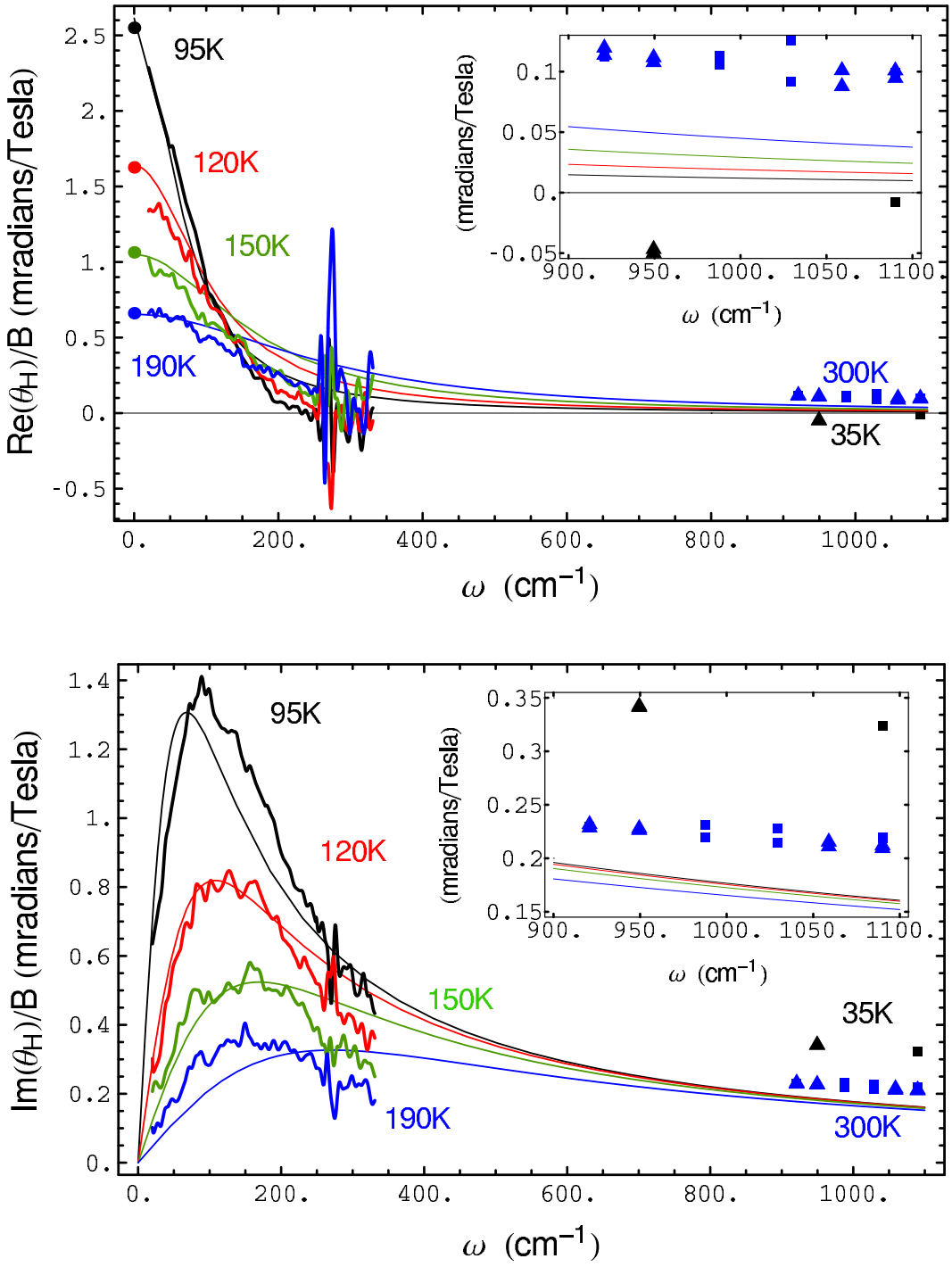

FIG. 16 Re(θ_H)/Tesla (upper) and Im(θ_H)/Tesla (lower) vs. frequency. The far-infrared data, which are below 400 cm^{-1}, are taken from Grayson [17]. The data of the current work are centered about 1000 cm^{-1} and also appear in the inset with the axes expanded. The smooth thin lines represent the fit using the Ioffe-Millis model.

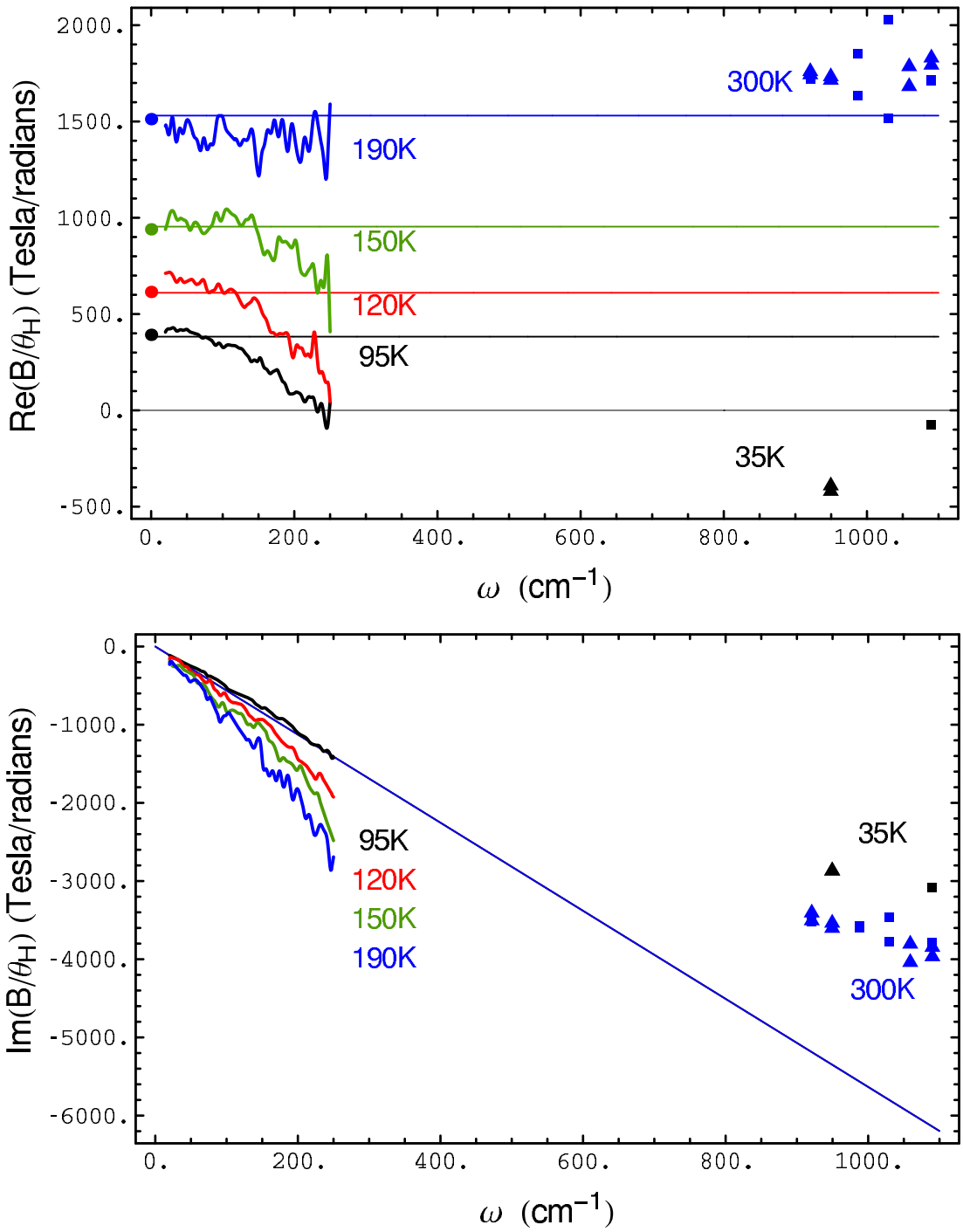

FIG. 17 $\mathrm{Re}(\theta_H^{-1})$ (upper) and $\mathrm{Im}(\theta_H^{-1})$ (lower) vs. frequency and normalized to 1 Tesla. The far-infrared data, which are below 400 cm^{-1}, are taken from Grayson [17]. The data of the current work are centered about 1000 cm^{-1}. The smooth thin lines represent the fit using the Ioffe-Millis model.

There are innumerable ways to accommodate the plunge in the real part of the Hall angle at 300 cm^{-1} and to join these results with those of the mid-infrared of the current work. This would seem to require at least one minimum and at least one maximum between 300 to perhaps 600 cm^{-1}. The plot of the imaginary part is equally strange and also demands some type of minimum and maximum between 300 and 600 cm^{-1}. Such a feature is suggestive of a simple resonance like that described in Appendix 6.4 in connection with the background Faraday rotation. However, our present purpose calls for a purely classical approach styled after the Drude model, which the reader may find in Appendix 6.5. This response arises from a simple charged harmonic oscillator in a magnet field.

Adding such a resonance to both σ_{xx} and σ_{xy} of a simple Drude model and calculating the Hall angle generated the plots in Fig. 18. The resonance accommodates the plunge rather well but it has done nothing to correct the temperature dependence in the mid-infrared. The values used for the plot are $\omega_c = .25\,cm^{-1}$ at 1 Tesla and

Temp	γ_1	ω_0	γ_2
95 K	100 cm^{-1}	300 cm^{-1}	700 cm^{-1}
120 K	160 cm^{-1}	380 cm^{-1}	700 cm^{-1}
150 K	250 cm^{-1}	420 cm^{-1}	700 cm^{-1}
190 K	380 cm^{-1}	500 cm^{-1}	700 cm^{-1}

where γ_1 and γ_2 are the scattering rates for the Drude term and the resonant term respectively. Addition of such a term produces an unusual peak for σ_{xx} which is clearly not seen in the data in Fig. 8. However, a peak is present at ~300 cm^{-1} in the phase of σ_{xx} in the 100 K plot of $\mathrm{Im}\,\sigma_{xx} / \mathrm{Re}\,\sigma_{xx}$ shown in Fig. 19 from the data of J. J. Tu. It is interesting to note that this feature in the phase is not predicted by the Ioffe–Millis model.

The above resonant Drude fit, though proffered without any theoretical basis, will find use below in representing the interpolation of the data for the integrand of the Hall angle sum rule.

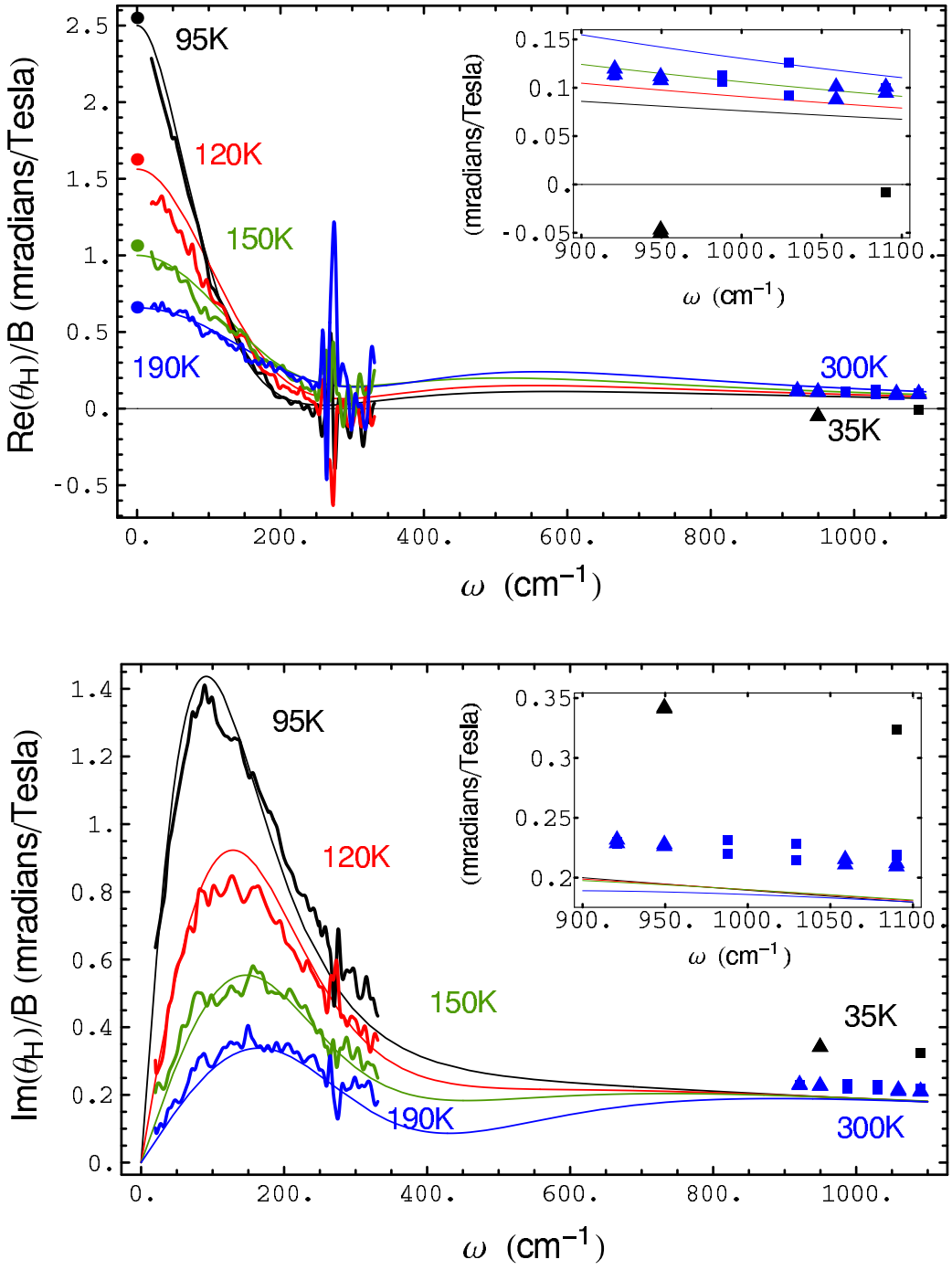

FIG. 18 Re θ_H / Tesla (upper) and Im(θ_H) / Tesla (lower) vs. frequency. The far-infrared data, which are below 400 cm^{-1} are taken from Grayson [17]. The data of the current work are centered about 1000 cm^{-1}, and also appear in the inset with the axes expanded. The smooth thin lines represent the fit using a Drude term plus a resonant term added to both σ_{xx} and σ_{xy}.

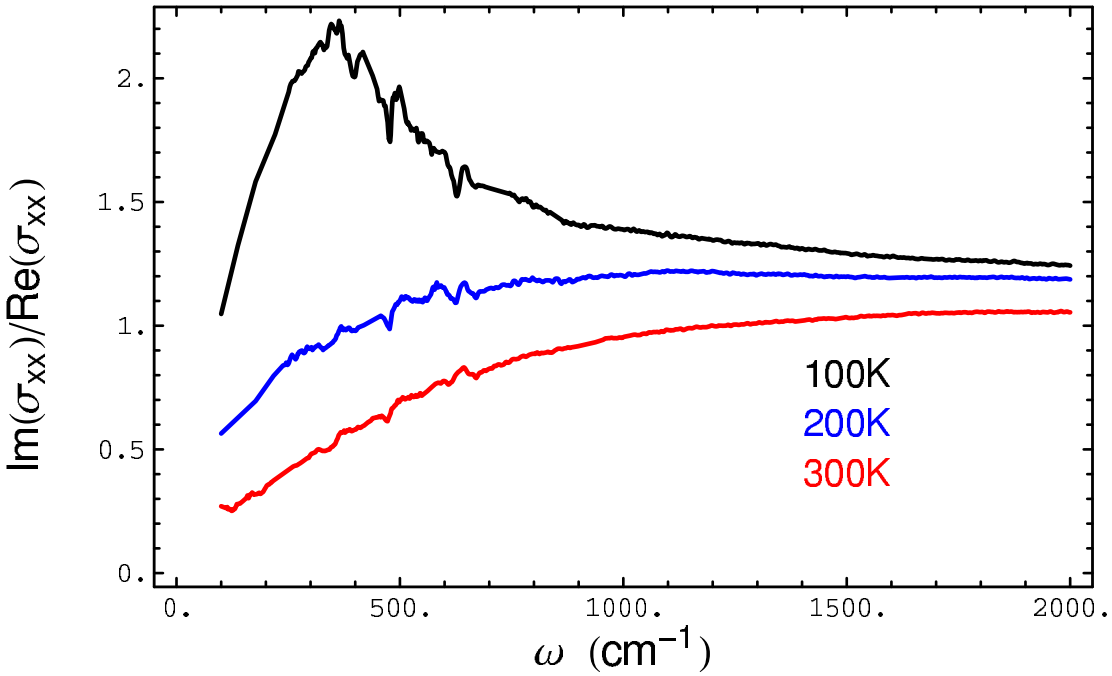

FIG. 19 $\mathrm{Im}\,\sigma_{xx}/\mathrm{Re}\,\sigma_{xx}$ vs. frequency. The data are adapted from that provided by J. J. Tu.

As demonstrated earlier the data of the current work expressed as the Hall angle follows a Drude form to some extent. Following this analysis the inverse Hall angle for a Drude conductivity presents a most revealing form when separated into its real and imaginary parts:

$$\theta_H^{-1} = \frac{1}{\omega_H \tau_H} - i\,\frac{\omega}{\omega_H}. \tag{47}$$

Figs. 20 and 21 contain plots of the real and imaginary parts of the inverse Hall angle for the data of the current work. The real part of θ_H^{-1} does not display a clear frequency dependence. Much of the frequency dependence of the imaginary part probably comes from ω which suggests that we assume a Drude conductivity and plot ω_H and τ_H separately. This we have done in the next section. Finally, unlike the far-infrared data, the temperature dependence in Fig. 21 for the real part of θ_H^{-1} is close to linear while the imaginary part is nearly constant. This also encourages analysis in terms an extended Drude model.

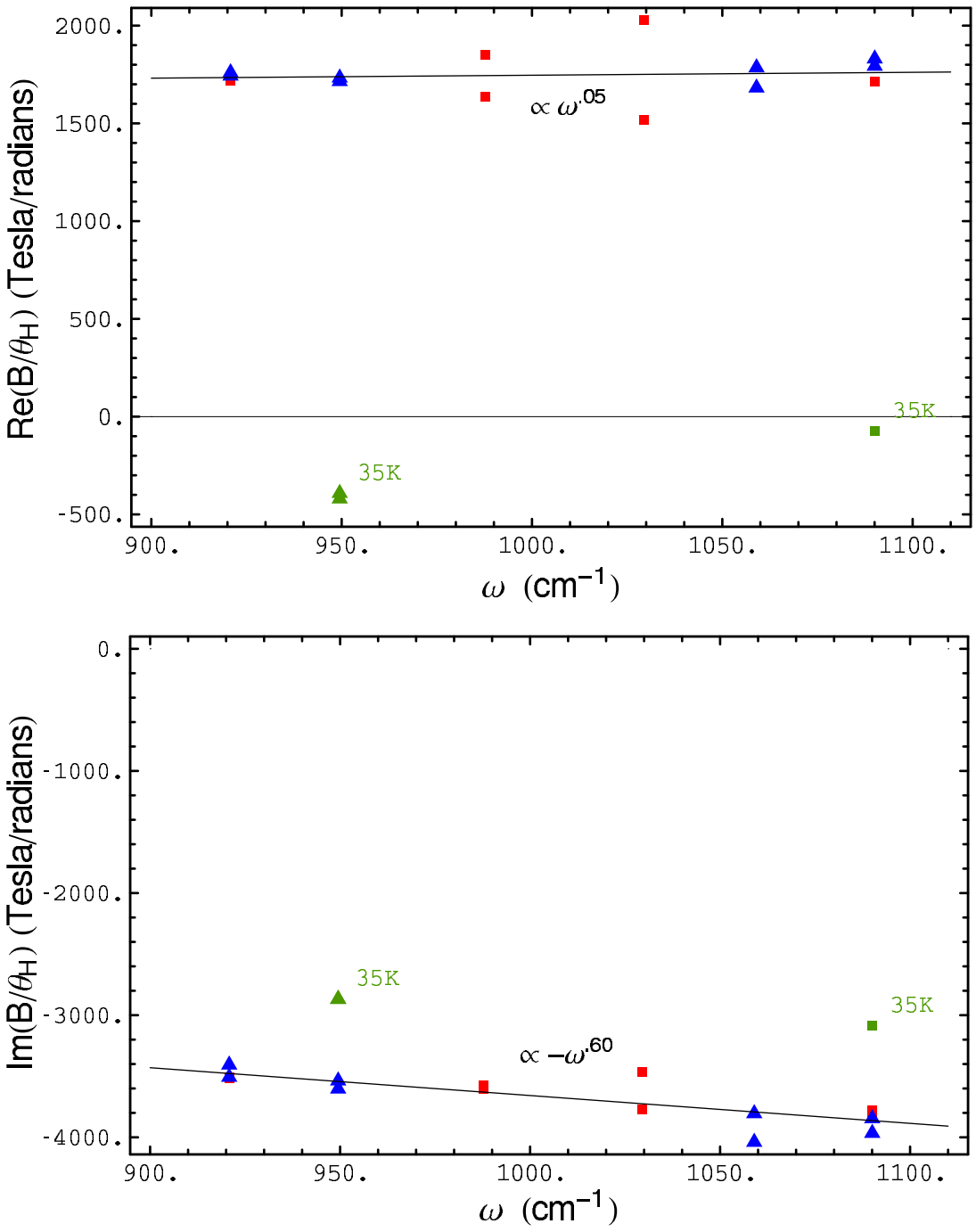

FIG. 20 The real part of $(\theta_H)^{-1}$ (upper) and the imaginary part of $(\theta_H)^{-1}$ (lower) for 2212 BSCCO, each versus frequency and normalized to 1 Tesla. The squares represent data set BSCCOBaFBScan083101.dat and the triangles represent data set BSCCOBaFBScan090201a.dat. The data correspond to a sample temperature of near 300K except for those points marked otherwise. There are twenty data points in each plot. The black line is a linear fit to the data along with its frequency dependence in black lettering.

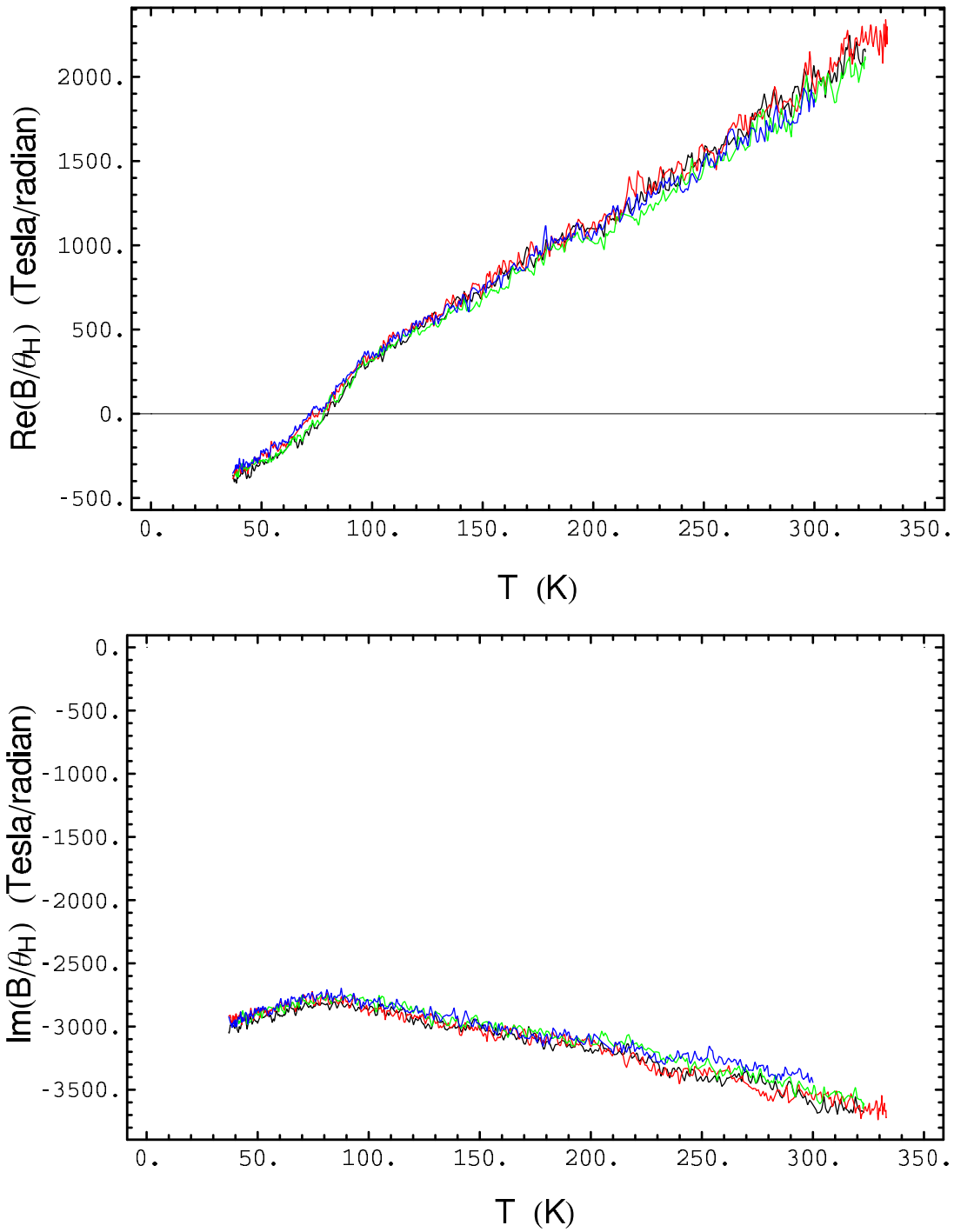

FIG. 21 The real part of θ_H^{-1} vs. temperature (upper) and the imaginary part of θ_H^{-1} vs. temperature (lower) for 2212 BSCCO normalized to 1 Tesla. As above each color represents a different subtracted pair of temperature scans all corresponding to a laser frequency of 950 cm^{-1}. There are four pairs total in each plot.

Before leaving the Hall angle analysis recall that all of the foregoing stands upon the sample thickness inferred from transmission data. Having seen many plots with nearly straight lines, perhaps now is opportune to determine the effects of an error in the assumed sample thickness. This involves entering other values for the thickness into equation (33) and proceeding to the Hall angle expressions. Figure 22 displays the real and imaginary parts of $\theta_H{}^{-1}$ resulting from this exercise for sample thicknesses of 150 nm (red) and 250 nm (blue). The change is small for the real part but the y intercept is different. The change in the imaginary part would change the Hall mass which is discussed in the next section. Even for such a large change in the thickness the conclusions one might have drawn thus far are essentially unchanged. So let us now proceed to Hall frequency and scattering rate analysis of the next section.

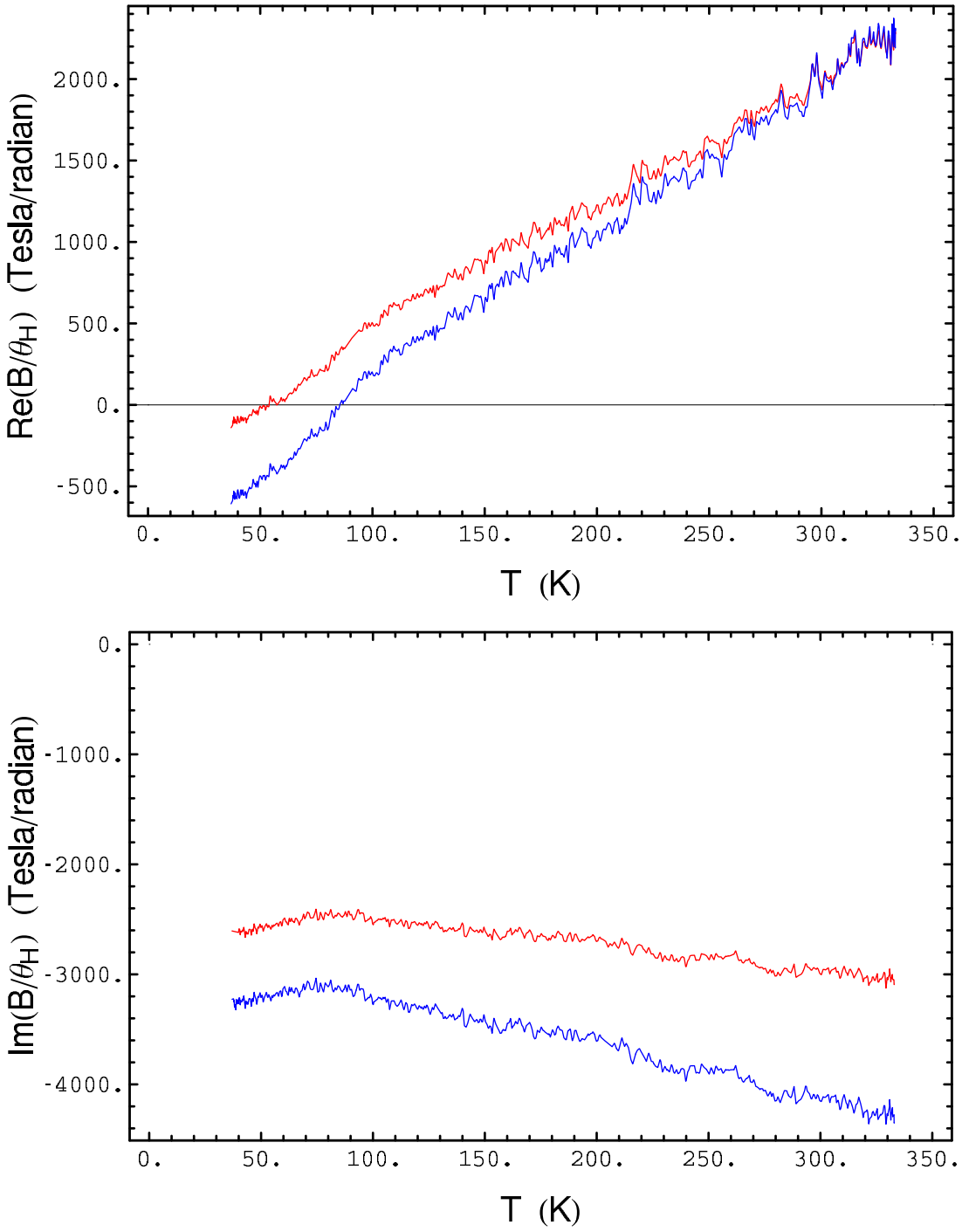

FIG. 22 The real part of θ_H^{-1} vs. temperature (upper) and the imaginary part of θ_H^{-1} vs. temperature (lower) for 2212 BSCCO normalized to 1 Tesla. The upper curve in red in each plot assumes the sample is 150 nm thick while the lower curve in blue assumes 250 nm. All correspond to a laser frequency of 950 cm^{-1}.

4.3 ω_H and γ_H

Following the suggestions of the earlier sections we now directly apply the extended Drude formalism to the data of the current work. We will consider the resulting scattering rate, Hall frequency and Hall Mass as compared to other calculated or measured values. Beginning with the frequency dependence, Fig. 23 shows both the Hall frequency and the scattering rate to be nearly constant in frequency. Recall that the far-infrared data of Grayson [17] when analyzed with the extended Drude form display a very different behavior with the scattering rate in particular exhibiting a strong decrease with frequency. In fact, this is one of the main features which conduced to the squared Lorentzian model. The lack of frequency dependence of the scattering rate of the current work on the other hand contravenes both Fermi liquid and marginal Fermi liquid theories, which claim a strong frequency dependence for the scattering rate at temperatures low compared to the energies corresponding to the frequencies. In the present circumstance $\omega = 1000 \approx 125\,\text{meV} > k_B\ 300\,\text{K} \approx 25\,\text{meV}$, yet there is little to no frequency dependence of the scattering rate.

Figure 24 displays the temperature dependences which fascinate the imagination even more when compared to far-infrared results. The Hall frequency (the inverse of the Hall mass) from the data of the current work is nearly constant—dropping by only a factor of .001 / K. The far-infrared Hall frequency in the extended Drude formalism drops by a factor of .02 / K over the same temperature region. The far-infrared scattering rate when compared to that of the mid-infrared curiously exhibits the same linear increase with temperature. However, the projection of the normal state mid-infrared scattering rate to zero temperature is negative. This feature was also observed for YBCO [15]. Notwithstanding, the extended Drude formalism would still seem to provide a useful description of the mid-infrared Hall behavior.

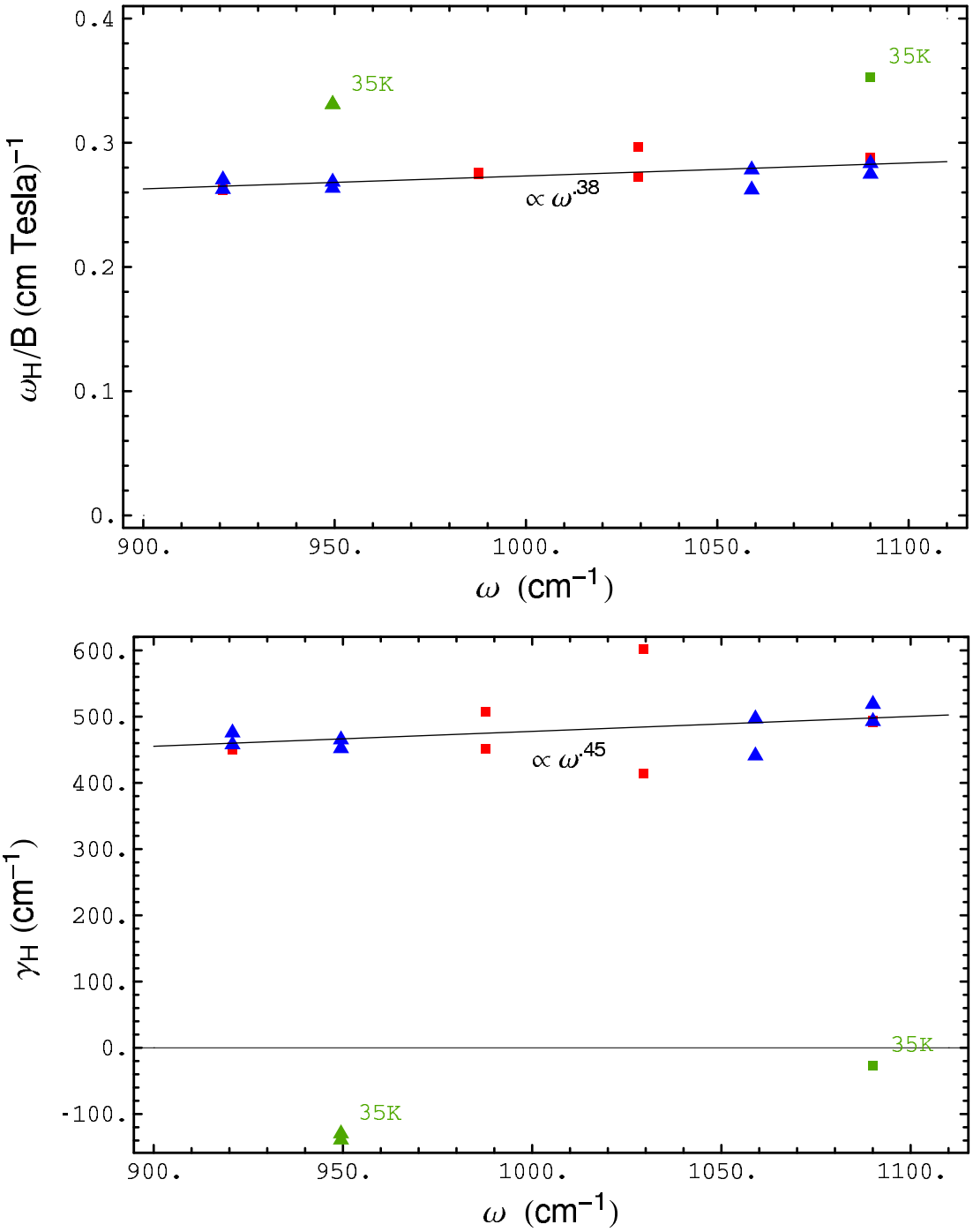

FIG. 23 ω_H normalized to 1 Tesla (upper) and γ_H (lower) both vs. frequency for 2212 BSCCO . The squares represent data set BSCCOBaFBScan083101.dat and the triangles represent data set BSCCOBaFBScan090201a.dat. The data correspond to a sample temperature of near 300K except for those points marked otherwise. There are twenty data points in each plot. The black line is a linear fit to the data along with its frequency dependence in black lettering.

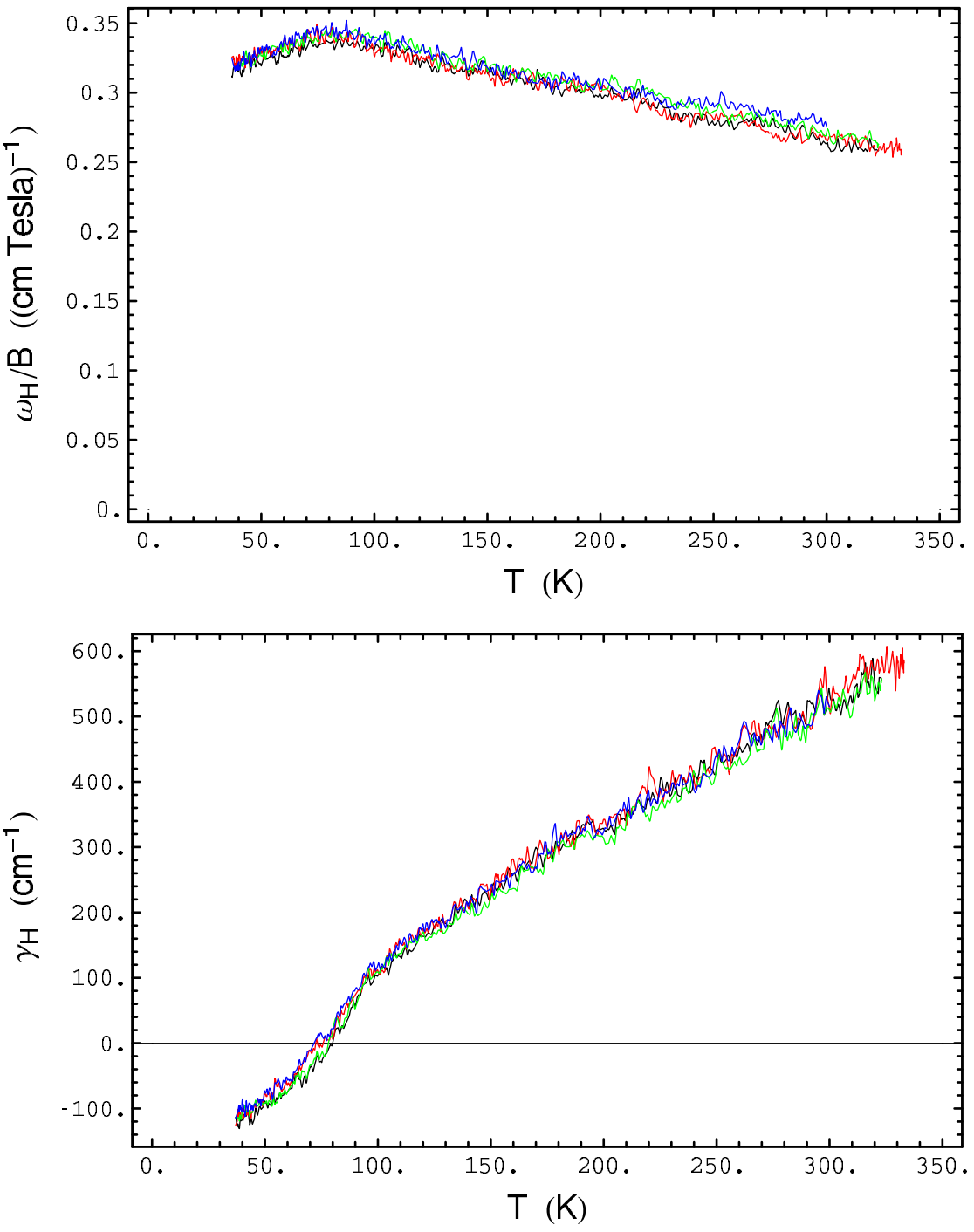

FIG. 24 ω_H normalized to 1 Tesla (upper) and γ_H (lower) both vs. temperature for 2212 BSCCO. Each color represents a different subtracted pair of temperature scans all corresponding to a laser frequency of 950 cm^{-1}. There are four pairs in each graph.

The situation has now become most perplexing: the scattering rate has a strong temperature dependence different than that of σ_{xx} or ImΣ in Fig. 4 of Valla [20] and, therefore, would seem to suggest two separate τ's as in Anderson's model, but the linear behavior disagrees with the predicted DC Hall scattering rate which varies as T^2.

Let us next use the results for ω_H to calculate the Hall mass and compare it to the both the band mass and the Fermi mass. The semiclassical model defines the Hall frequency as

$$\omega_H = \frac{2\pi e B}{\hbar^2 c}\left(\frac{\partial A(E)}{\partial E}\right)^{-1} \tag{48}$$

where $A(E)$ is the cross-sectional area of the Fermi distribution from $E = 0$ to E_F. Comparing this to the cyclotron frequency for a free electron one defines the Hall mass as

$$m_H = \frac{\hbar^2}{2\pi}\frac{\partial A(E)}{\partial E}$$

Thus, equation (48) becomes

$$\omega_H = \frac{eB}{c\, m_H} \tag{49}$$

Figure 24 indicates $\omega_H = 0.33\,\mathrm{cm}^{-1}$ at 95K and normalized to 1 Tesla. By equation (49) $m_H = 2.8\, m_e$.

The other values of the mass follow from the equation involving the velocity v:

$$m = \frac{\hbar k_F}{v}.$$

The band mass results from the use of the average band velocity, $\hbar v_{band} = 3.0$ eV Å, from Millis [31] and corresponding to a zone diagonal velocity of ~4.0 eV Å. The Fermi mass is calculated from the ARPES velocity, $\hbar v_F = 1.8$ eV Å, determined from the average of the dispersion [19]

$$\hbar v_F = \frac{\partial E}{\partial k}.$$

In either case we must first must determine the Fermi wave vector appropriate to the problem. This would be the hole-like surface shown in cross-section in Fig. 25. From Fig. 1 the Brillouin zone diagonal is $2\pi/5.5\,\text{Å}^{-1}$ and from Valla [20] $k_F = 0.446\,\text{Å}^{-1}$. So the radius of the nearly circular, hole-like Fermi surface shown in Fig 25 is $k_F' = 0.69\,\text{Å}^{-1}$.

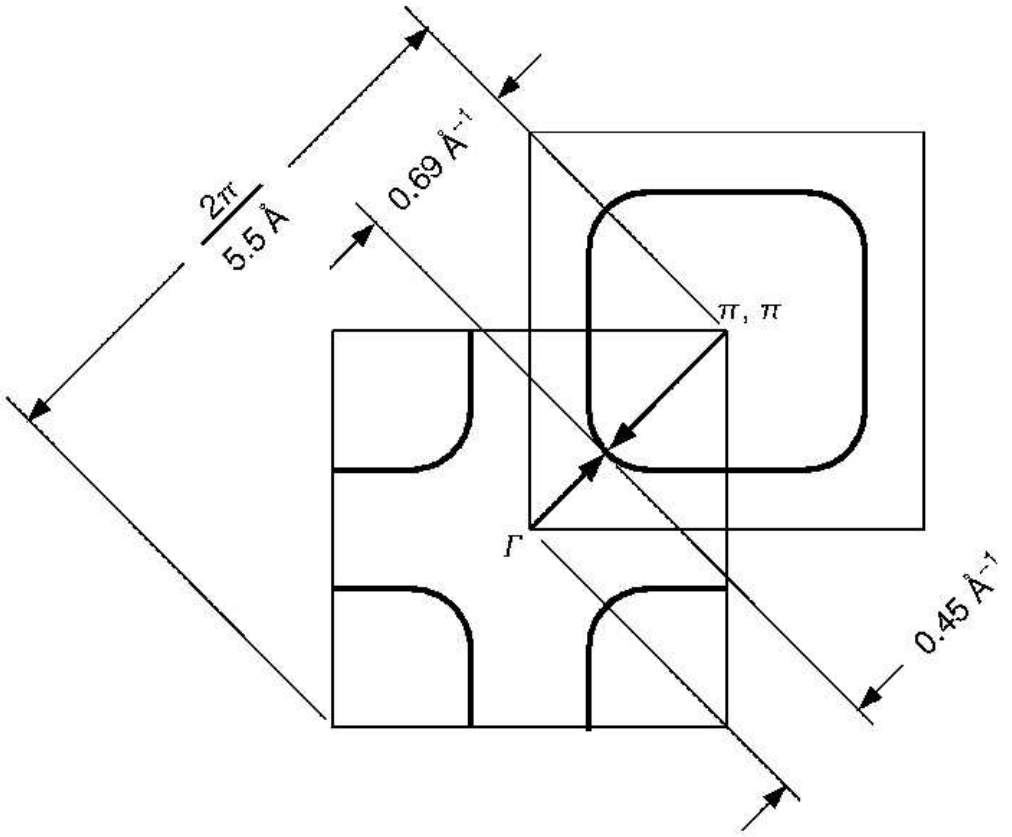

FIG. 25 Brillouin zone for 2212 BSCCO

The band mass is therefore

$$m_b = \frac{\hbar k_F}{v_b} = 1.8\,m_e .$$

The Fermi mass from ARPES is

$$m_F = \frac{\hbar k_F}{v_F} = \hbar k_F \left(\frac{1}{\hbar}\frac{\partial E}{\partial k}\right)^{-1} = 2.9\,m_e$$

which is surprisingly close to the Hall mass of the current work of $2.8\,m_e$.

Let us finally compare both the Hall mass and scattering rate with the mass and scattering rate for σ_{xx} by plotting the data of J.J. Tu using an extended Drude model:

$$1+\lambda(\omega) = -\frac{{\omega_p}^2}{4\pi}\,\frac{1}{\omega}\,\mathrm{Im}\left(\frac{1}{\sigma(\omega)}\right) \qquad \text{and} \qquad \gamma(\omega) = \frac{{\omega_p}^2}{4\pi}\,\mathrm{Re}\left(\frac{1}{\sigma(\omega)}\right)$$

where $1+\lambda(\omega)$ is the mass enhancement factor. Fig. [26] contains both results. For the mass an absolute value requires a knowledge of the number density. This value, which is explored below in section 4.5, can be based on any number of assumptions from the cut off for the *f*-sum rule to the volume of the Fermi surface determined by ARPES. For the present let us consider only the dependences. The frequency dependence for the mass enhancement in the mid-infrared region at 300K is $\omega^{-0.27}$ as shown in Fig. 26 by the thick black line Recalling that the mass dependence is the inverse of that of the Hall frequency, Fig. 23 (upper) gives $m_{\mathrm{H}} \propto \omega^{-.38}$.

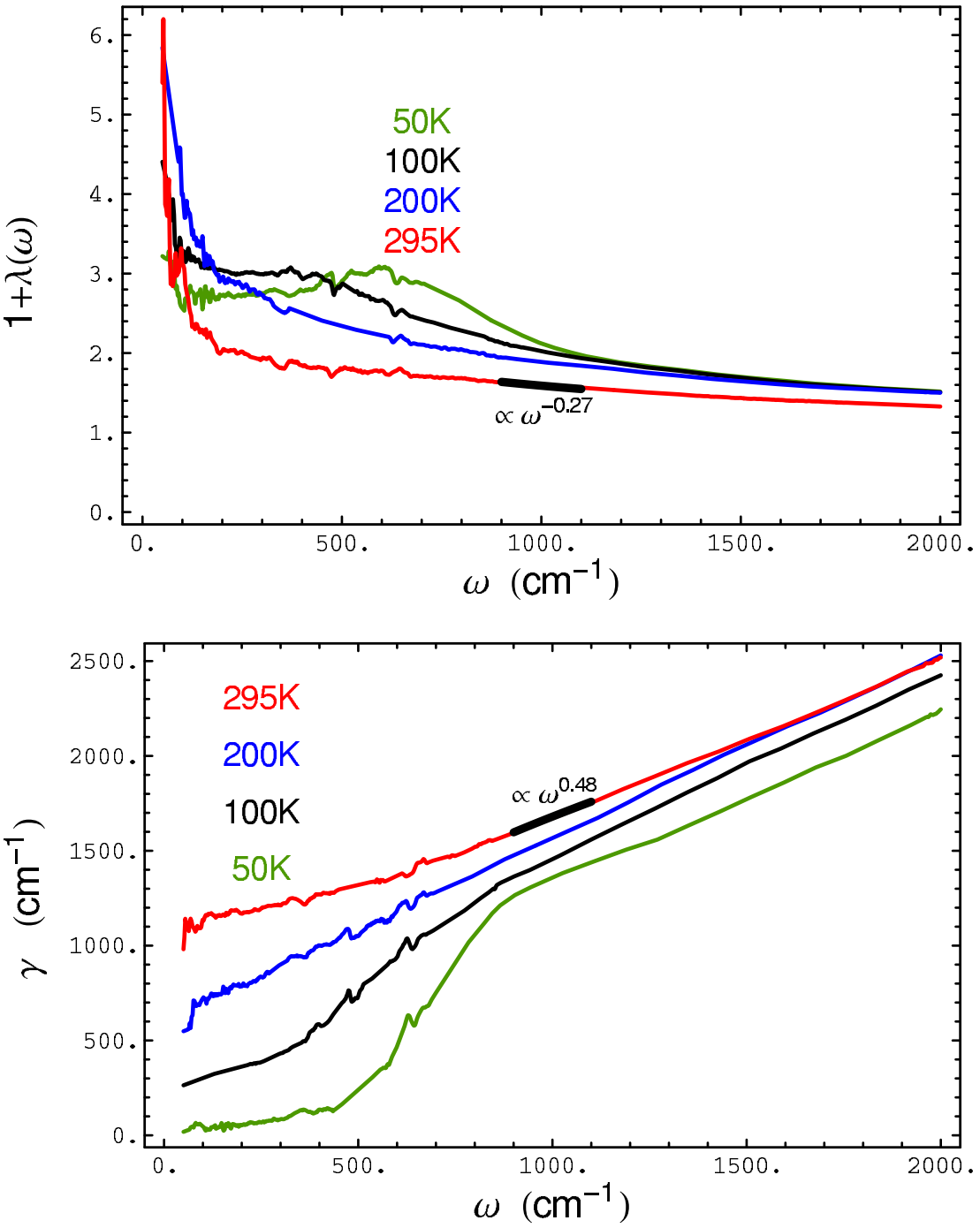

FIG. 26 Extended Drude analysis of σ_{xx} data provided by J. J. Tu. The thick black line demonstrates the frequency dependence in the 1000 cm^{-1} region

For the temperature dependence we cannot be quite so quantitative. Fig. 26 indicates that the mass decreases by about 20% from 100K to 295K in a nonlinear manner, whereas Fig. 24 shows ~20% increase in the mass over the same region in a linear manner.

At 300K the longitudinal scattering rate shown in Fig 26 (lower) is approximately three times higher than the Hall scattering rate shown in Fig. 23 but displays a frequency dependence of $\omega^{0.48}$ which is essentially the same as the $\omega^{.45}$ dependence of the Hall scattering rate in the mid-infrared. The temperature dependence of the longitudinal scattering rate in the mid-infrared appears quite linear in Fig 26, increasing about 15% from 100K to 295K, whereas the Hall scattering rate changes by about 85% over the same range. It is this large change in the Hall scattering rate at the relatively high frequency 1000 cm^{-1} (compared to the thermal energy) which argues against a Fermi liquid description of the mid-infrared scattering process.

4.4 $R_H = \sigma_{xy} / (\sigma_{xx}^2 B)$

Finally we may view the data of the current work as the real and imaginary parts of the Hall constant, which appear versus frequency in Fig. 27 and versus temperature in Fig. 28. The red line designated R_H^* represents the limiting value at high frequencies. It is calculated based on ARPES data and is explained below in section 4.5 with regard to the sum rule for R_H. Again we see the conduction is positive or hole–like. Neither term demonstrates any frequency dependence except in the superconducting state. Curiously, there remains the imaginary part which is about 1/3 of the real part and, lacking any frequency dependence, provides no hint of an eventual departure beyond the range of the current data. For a Drude we expect R_H to be real and constant in both frequency and temperature:

$$R_H = \frac{1}{ne}. \tag{50}$$

Fig. 28, however, indicates that the both the real part and imaginary parts of the Hall constant are decreasing with T. Further, even though the imaginary part is decreasing with increasing temperature, this decrease is slowing compared to the real part whose decrease with temperature appears to be accelerating. So, the trend does not seem to be approaching Drude behavior.

Figure 29 displays real and imaginary parts of the Hall constant for both the mid- and far-infrared data. The red line designated R_H^* represents the limiting value at high frequencies. It is calculated based on ARPES data and is explained below in section 4.5 with regard to the sum rule for R_H.

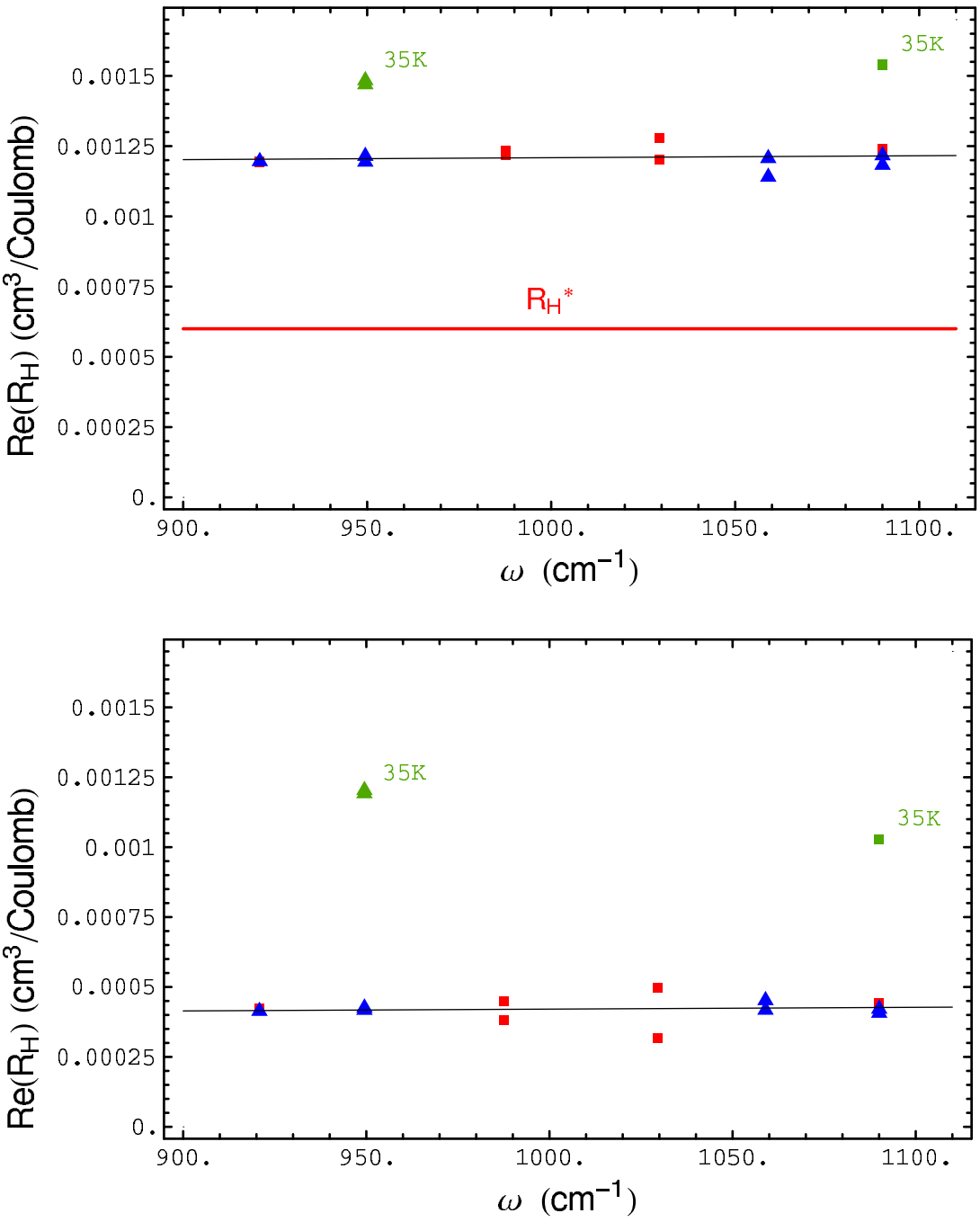

FIG. 27 The real part of R_H (upper) and the imaginary part of R_H (lower) for 2212 BSCCO, each versus frequency. The squares represent data set BSCCOBaFBScan083101.dat and the triangles represent data set BSCCOBaFBScan090201a.dat. The data correspond to a sample temperature of near 300K except for those points marked otherwise. There is a total of twenty data points in each plot. The red line designated R_H^* represents the limiting value at high frequencies calculated based on ARPES data. The black line is a linear fit to the data.

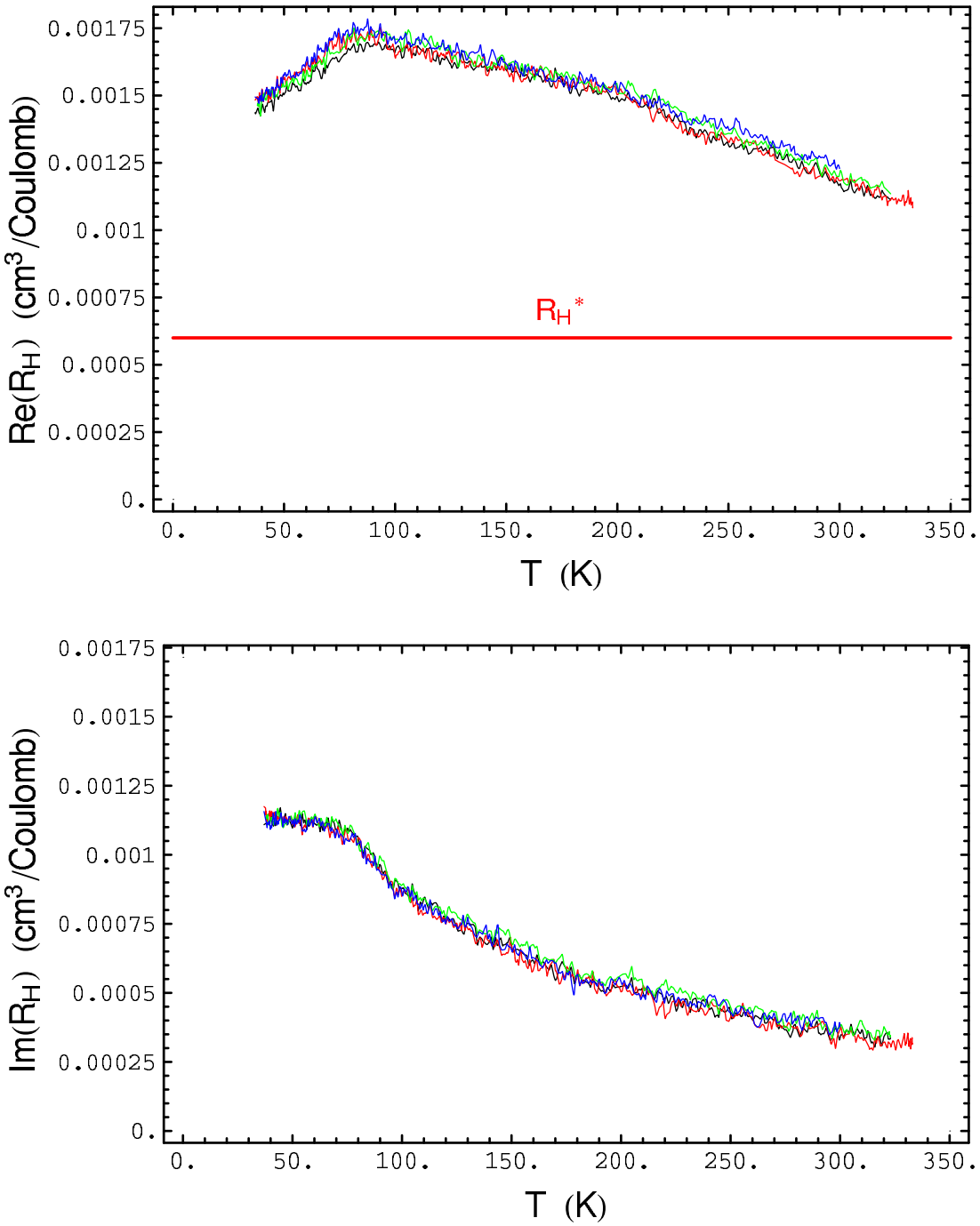

FIG. 28 The real part of R_H (upper) and the imaginary part of R_H (lower) vs. temperature for 2212 BSCCO. Each color represents a different subtracted pair of temperature scans all corresponding to a laser frequency of 950 cm^{-1}. There are four pairs in each graph. The red line designated $R_H{}^*$ represents the limiting value at high frequencies calculated based on ARPES data.

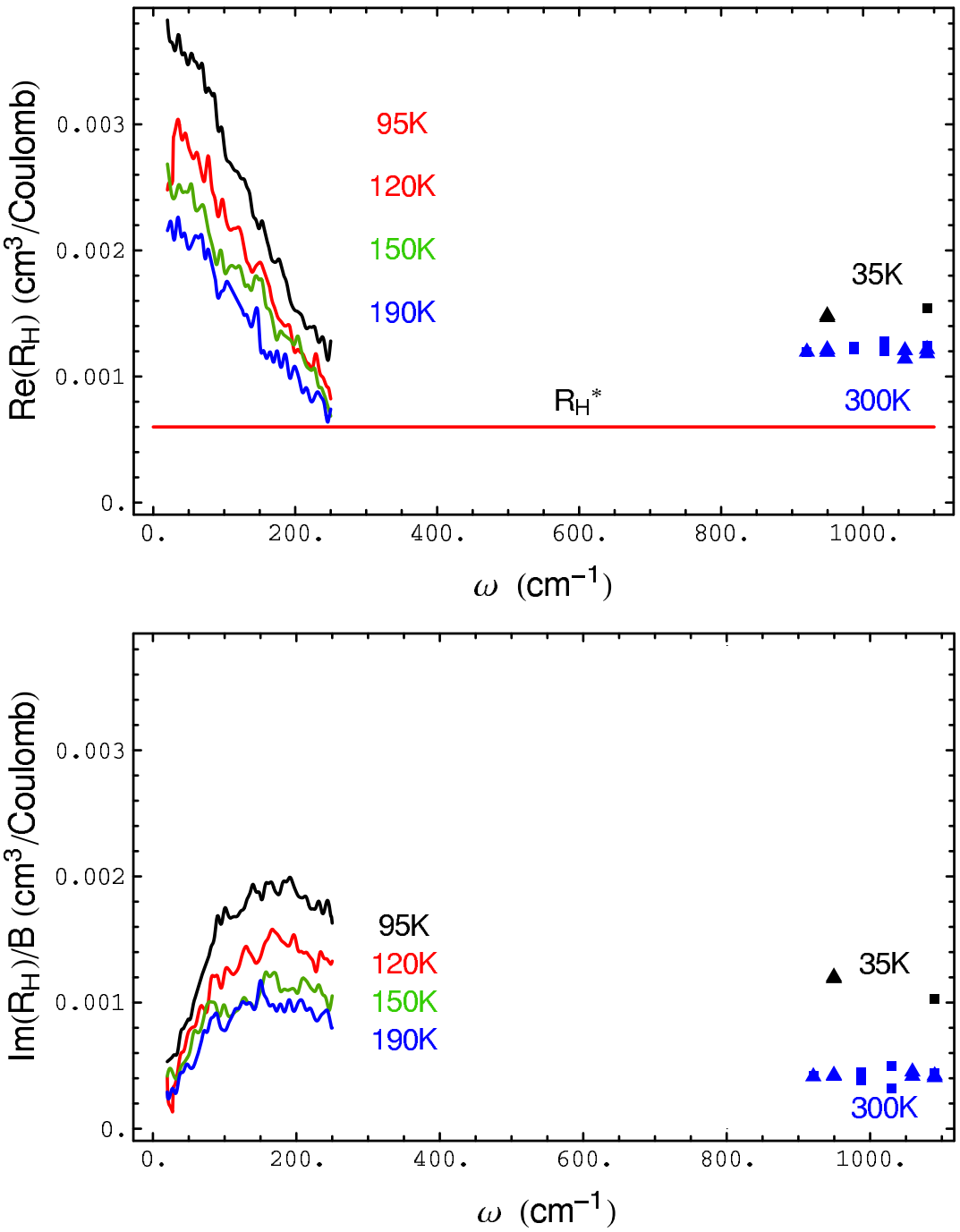

FIG. 29 The real part of R_H (upper) and the imaginary part of R_H (lower) vs. frequency for 2212 BSCCO. The far-infrared data, which are below 400 cm^{-1}, are taken from Grayson [17]. The data of the current work are centered about 1000 cm^{-1}. The squares represent data set BSCCOBaFBScan083101.dat and the triangles represent data set BSCCOBaFBScan090201a.dat. The red line designated R_H^* represents the limiting value at high frequencies calculated based on ARPES data.

4.5 Sum Rules

Hall data exists only for limited, separated regions of frequency space. To some extent we can extend our sight and knowledge using sum rules. The most relevant to our purpose are

$$S_{xx} = \int_0^{\omega_i} \mathrm{Re}\,\sigma_{xx}\, d\omega = \frac{\pi}{2}\,\frac{n e^2}{m} \propto \langle k_F\, v \rangle$$

$$\int_0^{\omega_i} \mathrm{Re}\,\sigma_{xy}\, d\omega = 0$$

$$\int_0^{\omega_i} \omega\,\mathrm{Im}\,\sigma_{xy}\, d\omega = S_{xx}\,\omega_H \propto \langle v^2 \rangle$$

$$\int_0^{\omega_i} \mathrm{Re}\,\theta_H\, d\omega = \frac{\pi}{2}\,\omega_H \propto \left\langle \frac{v}{k_F} \right\rangle$$

and

$$\int_0^{\omega_i} \mathrm{Re}\,R_H\, d\omega = \omega_i\, R_H{}^* \propto \left\langle \frac{1}{k_F{}^2} \right\rangle .$$

The use of the upper limit ω_i for the integration follows the "down-folded " approach of Millis [30], which assumes that the bands of interest occupy an energy region which is sufficiently separated from other bands to allow one to disregard their effects. Thus, one would find usefulness in summing a quantity up to an intermediate frequency ω_i which is well below the energies of the disregarded bands. Each of these sum rules is described in detail below.

The first, often called the *f*-sum rule, we should prefer to apply to only the free carriers in the sample. Toward this end let us determine what the sum would be for a Fermi liquid model with a cylindrical Fermi surface of radius k_F. The number of states (carriers) per physical volume within such a Fermi surface is:

$$n = \frac{(\text{spin freedom})\left(\frac{L}{2\pi}\right)^2 \frac{C_0}{2\pi}\pi k_F{}^2 k_z}{L^2 C_0}$$
$$= \frac{k_F{}^2}{C_0 2\pi}$$

where $C_0 = 2\pi/k_z$ is the average spacing between the planes (1/2 the lattice constant). For the mass m there are two values available to us through the following equation involving the velocity v:

$$m = \frac{\hbar k_F}{v}.$$

One value results from the use of the average band velocity, $\hbar v_{band} = 3.0$ eV Å, from Millis [31] and corresponding to a zone diagonal velocity of ~4.0 eV Å. The other is the Fermi mass from the ARPES velocity, $\hbar v_F = 1.8$ eV Å, determined from the average of the dispersion [19]

$$\hbar v_F = \frac{\partial E}{\partial k}.$$

Using $k_F{}' = 0.69$ Å^{-1} derived above from the ARPES data, the value of the sum corresponding to the band value of the velocity is

$$S_b = \frac{\pi}{2}\frac{ne^2}{m} = \frac{\pi}{2}e^2 \frac{k_F{}^2}{C_0 2\pi}\frac{v_b}{\hbar k_F} = 2.6\times 10^{18}\ \frac{1}{\text{cm Ohm second}}$$

and that corresponding to the Fermi value is

$$S_F = 1.6\times 10^{18}\ \frac{1}{\text{cm Ohm second}}$$

or in inverse centimeters

$$S_b = 14\ \frac{1}{\mu\text{Ohm cm}^2} \qquad \text{and} \qquad S_F = 8.4\ \frac{1}{\mu\text{Ohm cm}^2}.$$

From Fig. 30 one might well conclude that integration to 10000 cm^{-1} should include the low frequency contributions and that integration beyond this would add interband transitions. However, the cumulative sum does not achieve the above Fermi value until $\omega_i = 15300$ cm^{-1} nor the band value until $\omega_i = 27000$ cm^{-1}, which from Fig. 30 would

seem to be well within the interband region. This implies that there are substantial interaction effects well above 10000 cm^{-1} .

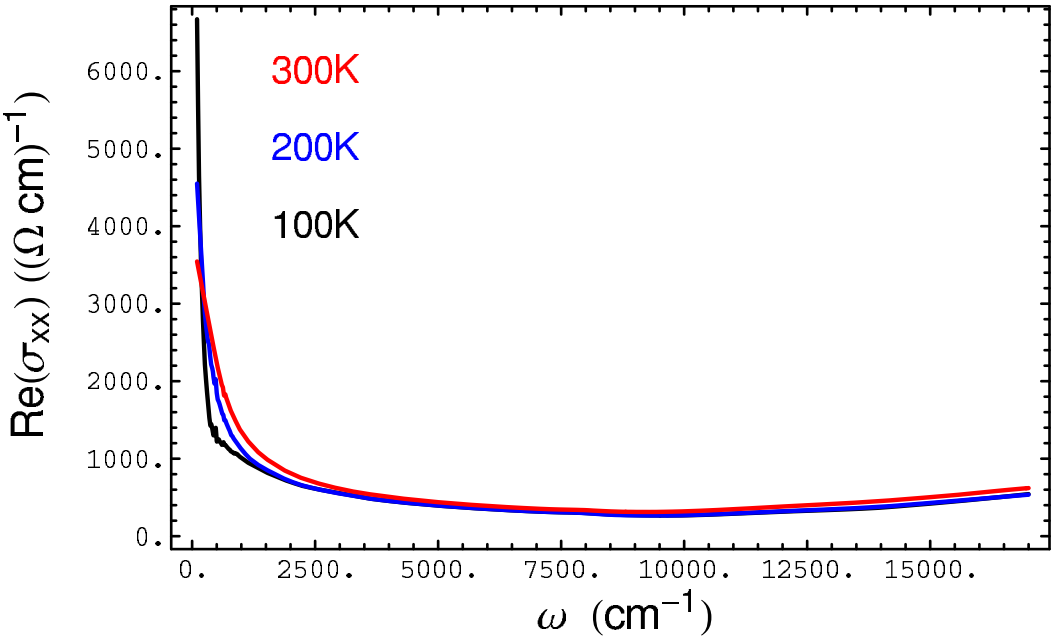

FIG. 30 The longitudinal conductivity of 2212 BSCCO from the data of J. J. Tu [28]

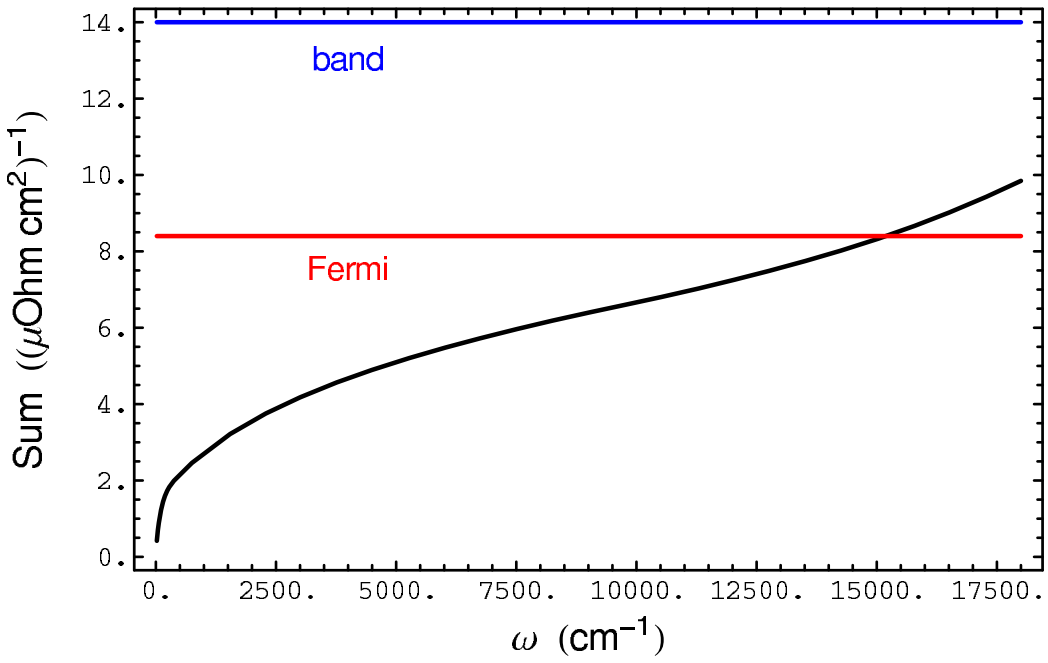

FIG. 31 The cumulative sum of the longitudinal oscillator strength of 2212 BSCCO from the data of J. J. Tu [28]. The blue line is the band value of the sum and the red is based on the Fermi velocity from the ARPES data.

The next sum rule to consider concerns the real part of the transverse conductivity:

$$\int_0^{\omega_i} \mathrm{Re}\,\sigma_{xy}\, d\omega = 0.$$

Because we yet lack continuous data we will substitute the Drude model fitted to each temperature appearing earlier in Fig. 11. To this we must join the consideration that the mid-infrared data for $\mathrm{Re}(\sigma_{xy})$ are constant in frequency in Fig. 9 and display the linear temperature dependence shown in Fig. 10. Neither of these features is represented by the Drude models. This would cause the sums to approach zero faster than shown in Fig. 32

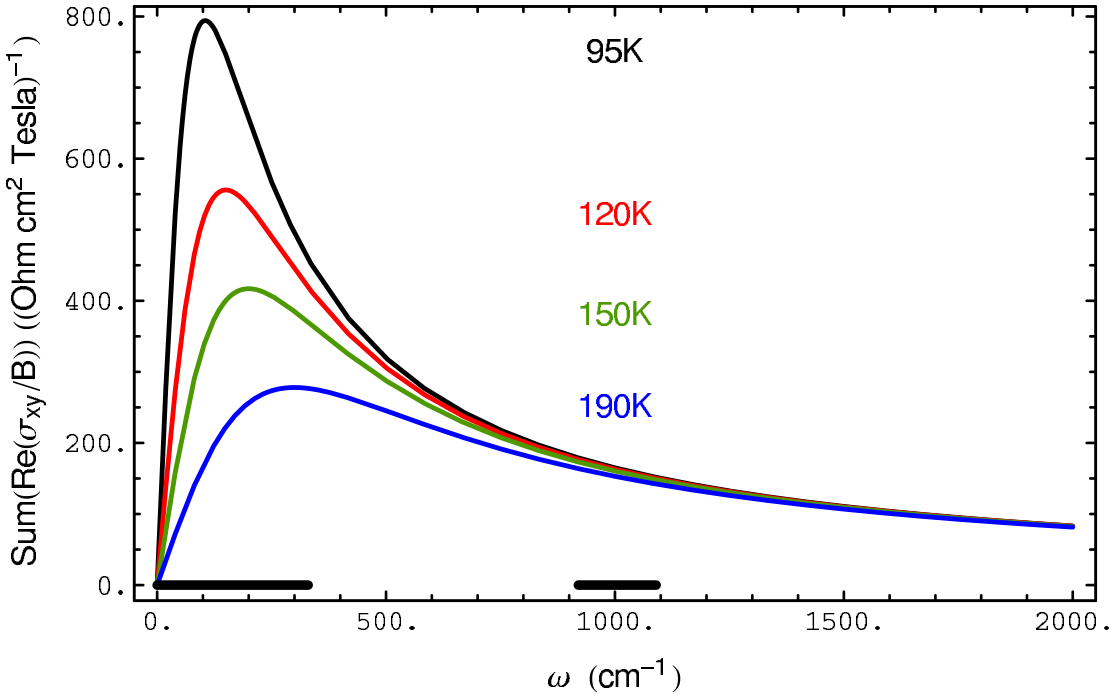

FIG. 32 The cumulative sum of the real part of σ_{xy} using the simple Drude fits shown above in Fig. 11. The heavy black lines at the bottom indicate those frequency regions over which we have data.

For example, if we assume that at 300K $\mathrm{Re}(\sigma_{xy})$ remains constant at the value of $-0.14\,(\Omega\,\mathrm{cm})^{-1}$ shown in Fig. 9, then the cumulative sum will reach zero at ~2000 cm^{-1}. Further, under this assumption, the sum would reach zero even faster for lower temperatures.

Next, let us consider the sum rule appropriate for the imaginary part of σ_{xy}, which for a circular Fermi surface is

$$I_{xy} = \int_0^{\omega_i} \omega\,\mathrm{Im}\,\sigma_{xy}\,d\omega = S_{xx}\,\omega_H \propto \langle v^2 \rangle .$$

The value of ω_H here involves the undressed mass or band mass from $v_{Band} = \partial E/\partial k \approx 3$ eV Å from Millis [31] and $k_F' = 0.69$ Å^{-1} derived above in section 4.5 from ARPES results:

$$m_b = \frac{\hbar k_F}{v_b} .$$

Set B equal to 1 Tesla:

$$(\omega_{\mathrm{H}})_{\mathrm{band}} = \frac{e}{m_{\mathrm{H}}} \text{ Tesla}$$

$$(\omega_{\mathrm{H}})_{\mathrm{band}} = e\,\frac{v_b}{\hbar k_{\mathrm{F}}}, \text{ Tesla}$$

$$= 0.53\,\mathrm{cm}^{-1}\,.$$

This is in contrast to the dressed or Fermi surface mass calculation for ω_{H} using the Fermi velocity from the ARPES data [19] as above:

$$(\omega_{\mathrm{H}})_{\mathrm{Fermi}} = 0.32\,\mathrm{cm}^{-1}\,.$$

We have two possible values for S_{xx} from above:

$$S_b = 14\,\frac{1}{\mu\mathrm{Ohm\,cm}^2} \qquad \text{and} \qquad S_{\mathrm{F}} = 8.4\,\frac{1}{\mu\mathrm{Ohm\,cm}^2}\,.$$

Combining these we obtain the following extreme values for I_{xy} :

$$\text{band:}\quad I_{\mathrm{xy}} = 7.4\times 10^6\,\frac{1}{\mathrm{Ohm\,cm}^3}$$

or

$$\text{Fermi:}\quad I_{\mathrm{xy}} = 2.6\times 10^6\,\frac{1}{\mathrm{Ohm\,cm}^3}\,.$$

Again because we yet lack continuous data, we will substitute the Drude model fitted to each temperature as shown in Fig. 11 for the plot of the cumulative sum. And again to this we must join the consideration that the mid-infrared data are not well represented by the Drude models. In fact, as shown in Figs. 10 and 11, $\mathrm{Im}(\sigma_{xy})$ is higher than the Drude values. This difference is further amplified by the factor of ω in the integrand. This would result in rather large additional contributions to the sum. For example, Fig. 9 indicates that at 1000 cm^{-1} the $\mathrm{Im}(\sigma_{xy}) = 0.45\ (\Omega\,\mathrm{cm\ Tesla})^{-1}$ and has a power law dependence for ω of -1.2. Using these values the cumulative sum at 10000 cm^{-1} is $\sim 3.2\times 10^{6}\ (\Omega\,\mathrm{cm\ Tesla})^{-1}$ or $\sim 1/2$ of the band value. This is very similar to the results for the *f*-sum rule above.

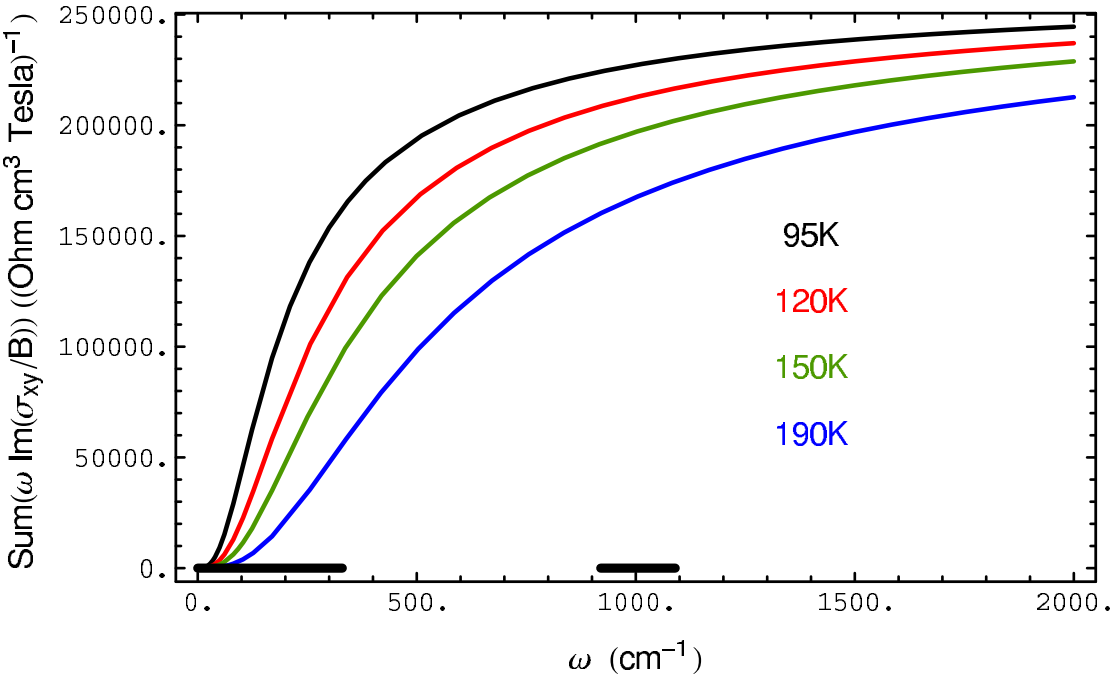

FIG. 33 The cumulative sum of $\omega\ \mathrm{Im}(\sigma_{xy})$ using the simple Drude fits shown above in Fig. 11. The heavy black lines at the bottom indicate those frequency regions over which we have data.

Next in the list is the Hall angle sum rule presented in Drew and Coleman [32]. This is particularly useful in examining the plunge in the real part of the Hall angle around 300 cm^{-1} and its effect on the cumulative sum. The sum rule is

$$\int_0^\infty \mathrm{Re}(\tan\theta_H)\, d\omega = \frac{\pi}{2}\,\omega_H\,,$$

which for the small angles involved may be simplified to

$$\int_0^\infty \mathrm{Re}\,\theta_H\, d\omega = \frac{\pi}{2}\,\omega_H = \frac{\pi}{2}\,\frac{eB}{m}. \qquad \text{(MKS)} \tag{51}$$

The value of ω_H here involves the undressed mass or band mass from $v_{Band} = \partial E/\partial k \approx 3$ eV Å from Millis [31]and the $k_F' = 0.69$ $Å^{-1}$ derived above in section 4.5 from ARPES results

$$m_b = \frac{\hbar k_F}{v_b}.$$

Again setting B equal to 1 Tesla:

$$\omega_H = 0.53\ cm^{-1}.$$

So, equation (51) becomes

$$\int_0^\infty \mathrm{Re}\,\theta_H\, d\omega = 0.83\ cm^{-1}, \tag{52}$$

As above, the gaps in the Hall data require the use of a fitted model to examine the cumulative sum. Below in Fig. 34 we employ the resonant Drude model of Fig. 18. The blue line represents the sum using the band value of the velocity. We have also included the sum based on the Fermi surface mass for comparison. The contribution up to 1100 cm^{-1} corresponding to the present Hall data reaches only 0.25 $(cm\ Tesla)^{-1}$ and provides only ~30% of the sum. If we assume the values indicated in Fig. 12: $\mathrm{Re}(\theta_H) = 0.1$ $(cm\ Tesla)^{-1}$ at 1000 cm^{-1} and a frequency power law dependence of $\omega^{-0.9}$, then the cumulative sum at 10000 cm^{-1} is 0.5 $(cm\ Tesla)^{-1}$ or just over ~1/2 of the band value. This is also very similar to the results for the f-sum rule above.

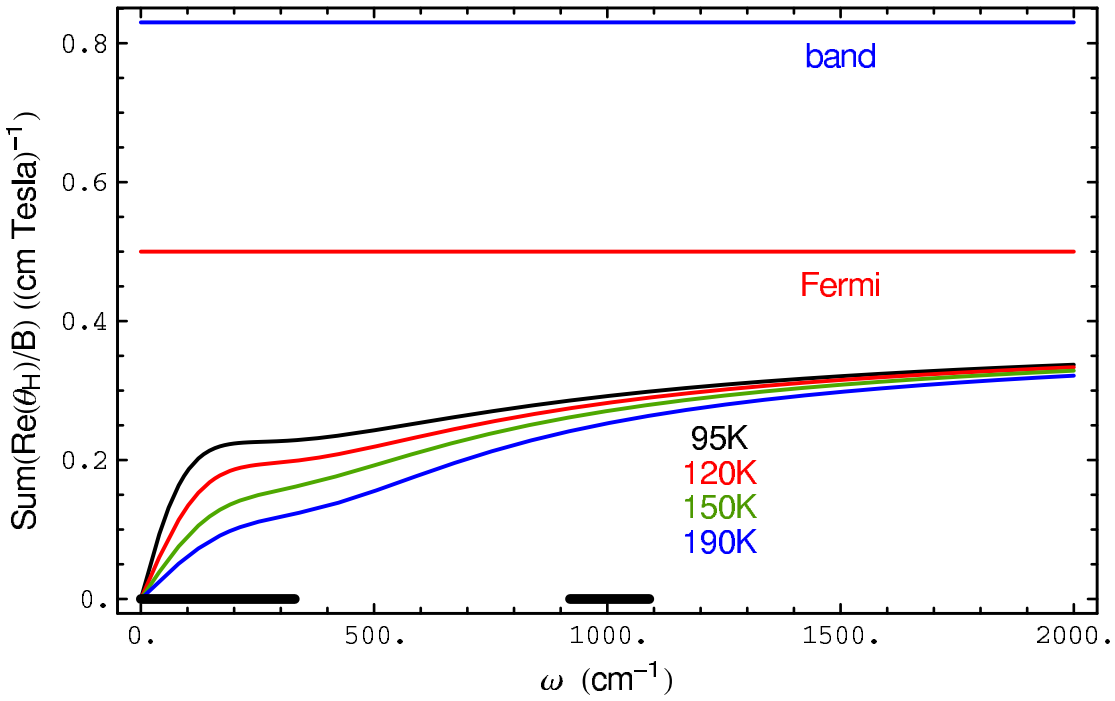

FIG. 34 The cumulative sum of the fits to Re(θ_H) using a simple Drude plus a resonant term. The blue line is the band value of the sum and the red is the based on the Fermi velocity from ARPES data. The heavy black lines at the bottom indicate those frequency regions over which we have data.

Finally, the sum rule involving the Hall constant arrives to us from Lange and Kotliar [29] who derived an expression for the Hall constant versus frequency particularly with regard to the sum rule which they had also derived. This sum rule simply indicates that the average value of R_H is equal to its value at infinity which for a Fermi liquid is

$$(\mathrm{Re}\, R_H)_{ave} = R_H{}^* = \frac{1}{e}\left(\frac{k_F{}^2}{C_0\, 2\pi}\right)^{-1}.$$

Using k_F' = 0.69 Å^{-1} derived above from the ARPES data and C_0 = 7.25 Å

$$(\mathrm{Re}\, R_H)_{ave} = .0006\ \frac{\mathrm{cm}^3}{\mathrm{Coulomb}}.$$

This is the line plotted in the upper graph in Fig. 29. At this point we see that none of the currently available data is below $R_H{}^*$ as required to satisfy the rule.

To realize the true power of these sum rules one requires more continuous data than that which we now possess. In particular the data should be representative of the same material. One could then attend to the task of attempting to relate those cumulative sums which show signs of saturation to physical processes involving particles which act independently of other aspects of these materials. For example, the cumulative sum of R_H seems to be within the range of the data. This sum involves only the Fermi wave vector and not the particle mass. The sums for $\mathrm{Re}(\sigma_{xx})$ and θ_H both involve the particle mass to the first power only. These sums are outside of the range of the data though only by a factor of two. Finally, the sum for $\omega\mathrm{Im}(\sigma_{xy})$ involves the mass to the 2nd power, so one might expect that this sum would lie outside the range of data by a factor of four, which it does not. And so another question arises: Does this behavior proceed out of our simple assumptions used to extrapolate the data, or does this indicate a strange property of the mass? The answer, of course, requires more complete data.

Though we have succeeded mainly in raising many new issues and questions, we have none the less identified some courses to pursue with which we shall in the next section conclude our discussion.

5 Conclusions

The Sixth no sooner had begun
About the beast to grope,
Than, seizing on the swinging tail
That fell within his scope,
'I see,' quoth he, 'the Elephant
Is very like a rope!'

Udana, a Canonical Hindu Scripture

In experimental physics one aspires to complete empirical knowledge and provide answers to pressing questions. In the current work, however, we must be content with raising new questions and demonstrating the need for additional experiments. Much of the cause of this circumstance rises out of the dissimilarity between the data of two nonadjacent regions of frequency space—the high frequency (mid-infrared) and the low frequency (DC to far-infrared). Some more of the cause of the circumstance rises out of the variance of the Hall data with that from longitudinal transport experiments. And still more rises out of the variance with contributions from other fields like photoemission. Below is a brief summary of the major points of contention involving the Hall data. This will be followed by some recommendations for future work.

Because the parameters from an extended Drude analysis of the current work are easily described by straight lines and because it was the odd behavior of these same parameters which in the far-infrared prompted an effort to assemble another model, let us continue with this approach. Probably the most salient feature of the current work is the implied Hall scattering rate. Much effort has been expended to explain the apparent T^2 behavior of the cotangent of the DC Hall angle. This was thought to arise out of a T^2 dependence of a Hall scattering rate. However, both the far- and mid-infrared results suggest that the characteristic behavior of scattering in the cuprates is a linear

increase with temperature. However, the features, which in the far-infrared conduced to the squared Lorentzian form, are not present in the mid-infrared. For example, the extended Drude analysis reveals a mid-infrared scattering rate increasing slowly with frequency, whereas that of the far-infrared decreases with frequency even perhaps becoming negative above 250 cm^{-1}. The linear temperature dependence of the Hall scattering rate in the mid-infrared also disagrees with the ARPES results for $-Im\Sigma$ [20], which imply a decreasing temperature dependence with increasing frequency as is also seen in σ_{xx}. Even marginal Fermi liquid theory, which favors a linear temperature dependence of the scattering is at odds with the lack of frequency dependence. Recall that a frequency dependence would have caused a significant positive intercept in the zero temperature projection of the normal state scattering rate in Fig. 24.

The behavior of the Hall mass is perhaps next in prominence. The frequency dependences for the Hall mass and longitudinal mass in the mid-infrared are similar displaying a slow decrease with increasing frequency. However, the temperature dependences of the masses are opposite each other with the Hall mass actually increasing about 20% over the temperature range of 100 to 300K. Furthermore, the extended Drude analysis of the far-infrared Hall data [17], suggest a mass enhancement with a full linear temperature dependence actually doubling from 95K to 190K and also increasing with frequency. Finally, as to thoroughly confuse the issue of carrier mass, the same ARPES measurements which imply a very different scattering rate returns to identify a full dressed mass which is nearly equal to the calculated mid-infrared Hall mass. Perhaps some of this can be reconciled by considering that interactions and scattering events affect Hall, longitudinal, and ARPES mass and scattering rates in different ways which require the use of more comprehensive calculations like the Kubo formalism in order to quantify.

Next, consider the plunge in the value of the real part of the Hall angle beginning at ~200 cm^{-1} and the very strong suggestion that it actually becomes

negative in the region between the far- and mid-infrared data. No obvious outstanding feature in this frequency range is apparent in either the real or imaginary parts of σ_{xx} or σ_{xy}. However, curiously there is a peak in this range visible in the phase of σ_{xx} at 95K. The frequency of the plunge roughly corresponds to numerous other phenomena including the 41 meV spin resonance, the 50±15 meV phonon interaction [21], the superconducting gap, and the quasiparticle band width of the three band Hubbard model. The relevance of the spin resonance perhaps can be determined by measuring the Hall transport in LSCO, which in neutron scattering studies does not display a strong spin resonance. Further, measuring the Hall transport in underdoped materials, which exhibit prominent pseudogaps, could help determine the relevance of the superconducting gap to the plunge. Of course, there is no substitute for actual data in the region of the plunge itself.

Finally, the sum rules also add no small amount of fascination to the subject. Using very simple extrapolation principles the cumulative *f*-sum, which is proportional to the band velocity, displays an inflection point at ~10,000 cm^{-1}, which would seem to signal the onset of interband transitions. But at this point the cumulative sum achieves only half of the value based on band mass. This suggests that the K.E. is lower or that the mass is higher than the band value by a factor of two due to interactions. The cumulative sum of $\mathrm{Re}(\theta_H)$ at 10,000 cm^{-1} likewise gives a sum which is only half of that based on band mass and therefore also suggests a mass of twice the band value. The cumulative sum for $\omega\,\mathrm{Im}(\sigma_{xy})$ at 10,000 cm^{-1} also achieves a value which is half of that based on band mass. However, because this sum is proportional to the velocity squared it curiously suggests a mass four times higher than the band mass. But, these results, however curious, teeter upon points of wild extrapolation and only additional data at higher frequencies can verify their significance.

No doubt, many other peripheral questions have been awakened in the mind of

the reader: What is the frequency dependence of the mid-infrared Hall transport at other temperatures? What effect would impurities have on the zero temperature scattering rate? What is the nature of the far-infrared Hall transport in BSCCO and how does it compare with that of YBCO? What effects would different dopings manifest? Perhaps the best approach for future work involves extending the Hall measurements for single crystal BSCCO into the far-infrared. Excellent data exists for longitudinal transport over a very large frequency and temperature range. Furthermore, because this material is single crystal, it shows little variation in longitudinal transport from sample to sample, thus allowing these results to be used to isolate σ_{xy}. YBCO, on the other hand, does not admit to the peeling process described above and therefore must be grown on substrates (each with its own optical transmission limitations) resulting in highly twinned structures with considerable variation in transport properties. Also consider that BSCCO is the material of choice for both ARPES and tunneling microscopy, so transport measurements can be more directly compared. The next dimension in which to extend Hall measurements in view of the foregoing is certainly that of other doping concentrations. The effect on the sum rules even in their current state would provide more interesting information relating to kinetic energy or carrier mass. And finally, one might consider designing experiments to obtain Hall data in the 50 meV region as well as the near-infrared. This might shed some light into the reason for the plunge in the Hall angle in this region.

So now, with a comprehensive description of both the experiment and the data behind us and with a comfortable surplus of work ahead, let us abide Prudence and bring an end to our current discussion.

6 Appendices

6.1 Polarization Analysis Using Dirac Notation

In polarimetric measurements a train of optical components, along with a sample, modify or operate on an input beam, which is in some state of known intensity and polarization. Optical components typically include somewhat imperfect devices such as polarizers, waveplates, photoelastic modulators, and mechanical rotators. The modified output beam generally strikes a detector producing an output electrical signal. Here we develop a general formalism useful in relating the electrical signal to the properties of the sample. The formalism uses Dirac notation which well differentiates between a vector or state $|\psi\rangle$ and its representation in some basis: $\langle x|\psi\rangle$. In polarimetry the usual bases are linear polarization and circular polarization. The formalism also replaces the Jones matrices with generalized operators and introduces the basis transformations and geometrical rotation operations. Finally the result is related to the output of the typical optical, "square law" detector.

In what follows the direction of propagation is in the positive z direction and all angles are measured in the positive radial direction off the x axis and about the z axis. Beginning with the input beam, the formalism simply considers it to be a non−normalized ket

$$|\text{in}\rangle.$$

Expressed in the linear polarization basis it is

$$|\text{in}\rangle = \sum_L |L\rangle\langle L|\text{in}\rangle = |x\rangle\langle x|\text{in}\rangle + |y\rangle\langle y|\text{in}\rangle$$

or in the circular basis

$$|\text{in}\rangle = \sum_C |C\rangle\langle C|\text{in}\rangle = |p\rangle\langle p|\text{in}\rangle + |n\rangle\langle n|\text{in}\rangle$$

where $|\,p\rangle$ indicates an electric vector rotating in the positive radial direction about the z axis as seen at a fixed point

and $|\,n\,\rangle$ indicates an electric vector rotating in the negative radial direction about the z axis also as seen at a fixed point.

$|\,p\,\rangle$ and $|\,n\,\rangle$ are also referred to as having positive and negative helicity. In matrix notation

$$\langle L \,|\, \text{in}\rangle = \begin{pmatrix} E_x \\ E_Y \end{pmatrix} \qquad \text{and} \qquad \langle C \,|\, \text{in}\rangle = \begin{pmatrix} E_p \\ E_n \end{pmatrix}$$

The various components in the optical train appear as operators acting on the input ket to produce the output ket:

$$|\,\text{out}\,\rangle = T\,V\,W\,|\,\text{in}\rangle$$

In the linear basis this is

$$\begin{aligned} |\,\text{out}\,\rangle &= |\,L\,\rangle\langle\,L\,|\;T\,V\,W\,|\,L'\,\rangle\langle\,L'\,|\,\text{in}\,\rangle \\ &= |\,L\,\rangle\langle\,L\,|\,T\,|\,L''\,\rangle\langle\,L''\,|\,V\,|\,L'''\,\rangle\langle\,L'''\,|\,W\,|\,L'\,\rangle\langle\,L'\,|\,\text{in}\,\rangle \\ &= |\,L\,\rangle\langle\,L\,|\,T\,|\,L\,\rangle\langle\,L\,|\,V\,|\,L\,\rangle\langle\,L\,|\,W\,|\,L\rangle\langle\,L\,|\,\text{in}\,\rangle \end{aligned}$$

where summation is assumed over repeated state designations, L; and the primes have been dropped with the understanding the order of the matrices will not be changed.

Some devices or operations such as geometric rotation and Faraday rotation are most easily represented in the circular basis. The transformation matrices, $\langle\,C\,|\,L\,\rangle$ and $\langle\,L\,|\,C\,\rangle$, are the means of conversion between these two bases. The transformation for states proceeds as

$$\begin{aligned} |\,\text{in}\,\rangle &= \textstyle\sum_L\; |\,L\,\rangle\langle\,L\,|\,\text{in}\,\rangle \\ &= \textstyle\sum_{LC}\; |\,C\,\rangle\langle\,C\,|\,L\,\rangle\langle\,L\,|\,\text{in}\,\rangle \end{aligned}$$

$$= |C\rangle\langle C|L\rangle\langle L|\text{in}\rangle,$$

and for operators as

$$T = \sum_{L,L'} |L\rangle\langle L|T|L'\rangle\langle L'|$$

$$= \sum_{L,L'} \sum_{C,C'} |C\rangle\langle C|L\rangle\langle L|T|L'\rangle\langle L'|C\rangle\langle C'|$$

$$= |C\rangle\langle C|L\rangle\langle L|T|L\rangle\langle L|C\rangle\langle C|.$$

In Matrix representation

$$\langle C|L\rangle = \frac{1}{\sqrt{2}}\begin{pmatrix} 1 & -i \\ 1 & i \end{pmatrix} \qquad \text{and} \qquad \langle L|C\rangle = \frac{1}{\sqrt{2}}\begin{pmatrix} 1 & 1 \\ i & -i \end{pmatrix}.$$

Below are the representations of some simple optical components:

a perfect polarizer aligned along the x axis in linear basis

$$\begin{pmatrix} 1 & 0 \\ 0 & 0 \end{pmatrix},$$

a 1/4 waveplate aligned with slow axis along x axis

$$\begin{pmatrix} e^{i\frac{\pi}{2}} & 0 \\ 0 & 1 \end{pmatrix},$$

a photoelastic modulator aligned along the x axis in linear basis

$$\begin{pmatrix} e^{i\beta\cos(2\pi f t)} & 0 \\ 0 & 1 \end{pmatrix}.$$

Another concern for the devices or components is their orientation. Assume, for example, that the operator T represents the effect of some component such a polarizer which is aligned with its critical direction at an angle θ from the x axis. A simple rotation operation develops an expression for the rotated polarizer:

$$T(\theta) = R\ T\ R^{-1}$$

where R is an active rotation and in circular representation is

$$\langle C \mid R(\theta) \mid C \rangle = \begin{pmatrix} e^{-i\theta} & 0 \\ 0 & e^{i\theta} \end{pmatrix}.$$

Finally, the output of a square-law type optical detector, aside from any responsivity factor is for our example

$$d(t) \propto \langle \text{out} \mid \text{out} \rangle$$

where $\mid \text{out} \rangle$ is the Hermitian conjugate of $\langle \text{out} \mid$.

6.2 Multilayer Response Using Relative Impedance Matrices

Assume that some layered materials are arranged normal to the z axis and we desire a formalism for the transmitted and reflected intensities for plane waves incident at arbitrary angles. To begin, the plane wave solution to Maxwell's equations is:

$$\begin{aligned} \vec{E}_{i,\pm} &= \vec{\mathcal{E}}_{i,\pm}\, e^{i\vec{k}_{i,\pm}\cdot\vec{r}-i\omega t} \\ \vec{H}_{i,\pm} &= \vec{\mathcal{H}}_{i,\pm}\, e^{i\vec{k}_{i,\pm}\cdot\vec{r}-i\omega t} \end{aligned} \tag{53}$$

where $+$ represents a wave traveling in the positive z direction at some otherwise arbitrary angle

$-$ represents a wave traveling in the negative z direction

and i is the layer number.

Then in CGS:

$$\begin{aligned} \vec{H}_{i,\pm} &= \sqrt{\frac{\epsilon_i}{\mu_i}}\, \hat{k}_{i,\pm} \times \vec{E}_{i,\pm} \\ &= \frac{1}{Z_i}\, \hat{k}_{i,\pm} \times \vec{E}_{i,\pm} \qquad \text{CGS} \end{aligned} \tag{54}$$

where ϵ_i is the complex dielectric constant of the i'th layer and includes all conductivity effects

and $Z_i = \sqrt{\frac{\mu_i}{\epsilon_i}}$ is the relative impedance of the medium and

like ϵ may be complex.

Now that we have a solution inside a layer we need to match solutions for different layers at the boundaries between layers. The curl E Maxwell equation provides one boundary condition:

$$\vec{E}_i \times \hat{z} = \vec{E}_{i+1} \times \hat{z} \tag{55}$$

The curl H Maxwell equation provides the other boundary condition:

$$\vec{H}_i \times \hat{z} = \vec{H}_{i+1} \times \hat{z} \tag{56}$$

To apply the foregoing consider first, S polarization (E perpendicular to the plane of incidence) at each side of a boundary. In such an instance the E field is tangent to the boundary and if we orient the x and y axes so that E is also perpendicular to the y axis, then, from equation (55):

$$\vec{\mathcal{E}}_{i,+,x} + \vec{\mathcal{E}}_{i,-,x} = \vec{\mathcal{E}}_{i+1,+,x} + \vec{\mathcal{E}}_{i+1,-,x} \tag{57}$$

Likewise, substituting equation (54) into (56) produces:

$$\frac{1}{Z_i}\left(\vec{k}_{i,+} \times \vec{\mathcal{E}}_{i,+} + \vec{k}_{i,-} \times \vec{\mathcal{E}}_{i,-}\right) \times \hat{z} = \frac{1}{Z_{i+1}}\left(\vec{k}_{i+1,+} \times \vec{\mathcal{E}}_{i+1,+} + \vec{k}_{i+1,-} \times \vec{\mathcal{E}}_{i+1,-}\right) \times \hat{z}$$

or

$$\frac{\cos(\theta_i)}{Z_i}\left(\mathcal{E}_{i,+,x} - \mathcal{E}_{i,-,x}\right) = \frac{\cos(\theta_{i+1})}{Z_{i+1}}\left(\mathcal{E}_{i+1,+,x} - \mathcal{E}_{i+1,-,x}\right) \tag{58}$$

Defining the incident impedance for S polarization as:

$$Z_{s,i+1} = \frac{Z_i}{\cos(\theta_i)} \tag{59}$$

equation (58) becomes

$$\frac{1}{Z_{s,i}}\left(\mathcal{E}_{i,+,x} - \mathcal{E}_{i,-,x}\right) = \frac{1}{Z_{s,i+1}}\left(\mathcal{E}_{i+1,+,x} - \mathcal{E}_{i+1,-,x}\right) \tag{60}$$

Combining equations (57) and (60) into a matrix form:

$$\begin{pmatrix} \mathcal{E}_{i+1,+} \\ \mathcal{E}_{i+1,-} \end{pmatrix} = \frac{1}{2Z_{s,i}} \begin{pmatrix} Z_{s,i} + Z_{s,i+1} & Z_{s,i} - Z_{s,i+1} \\ Z_{s,i} - Z_{s,i+1} & Z_{s,i} + Z_{s,i+1} \end{pmatrix} \begin{pmatrix} \mathcal{E}_{i,+} \\ \mathcal{E}_{i,-} \end{pmatrix} \tag{61}$$

$$= S_{i,i+1} \begin{pmatrix} \mathcal{E}_{i,+} \\ \mathcal{E}_{i,-} \end{pmatrix} \tag{62}$$

For P polarization (E field || to plane of incidence) define the incident admittance as:

$$Y_{p,i} = \frac{1}{\cos(\theta_i) Z_i} \tag{63}$$

then following the same procedure:

$$\begin{pmatrix} \mathcal{H}_{i+1,+} \\ \mathcal{H}_{i+1,-} \end{pmatrix} = \frac{1}{2\,Y_{p,i}} \begin{pmatrix} Y_{p,i+1} + Y_{p,i} & Y_{p,i+1} - Y_{p,i} \\ Y_{p,i+1} - Y_{p,i} & Y_{p,i+1} + Y_{p,i} \end{pmatrix} \begin{pmatrix} \mathcal{H}_{i,+} \\ \mathcal{H}_{i,-} \end{pmatrix} \tag{64}$$

$$= P_{i,i+1} \begin{pmatrix} \mathcal{H}_{i,+} \\ \mathcal{H}_{i,-} \end{pmatrix}$$

The E field can be determined from H using equation (54).

Equations (59) and (61) and Equations (63) and (64) provide the incident and reflected amplitudes in the $i+1$ layer at the interface in terms of the amplitudes in the i layer at the interface for S and P polarization respectively. It remains to develop the equations to propagate the amplitudes across layer i of thickness d_i. This is already provided by equations (53) which in matrix form become:

$$\begin{pmatrix} \mathcal{E}_{i,+}(z = d_i) \\ \mathcal{E}_{i,-}(z = d_i) \end{pmatrix} = \begin{pmatrix} e^{i\,\vec{k}_{i,+} \cdot \hat{z}\, d_i} & 0 \\ 0 & e^{-i\vec{k}_{i,-} \cdot \hat{z}\, d_i} \end{pmatrix} \begin{pmatrix} \mathcal{E}_{i,+}(z = 0) \\ \mathcal{E}_{i,-}(z = 0) \end{pmatrix}$$

$$= U_i \begin{pmatrix} \mathcal{E}_{i,+}(z = 0) \\ \mathcal{E}_{i,-}(z = 0) \end{pmatrix}$$

So, as an example, given a set of layers from 1 to n, the equation relating the incident and reflected amplitudes on one side of the set to the other side for S polarization is:

$$S_{n-1,n}\; U_{n-1}\; S_{n-2,n-1}\; \ldots\; U_{i+1}\; S_{i,i+1} \begin{pmatrix} \mathcal{E}_{i,+}(z = 0) \\ \mathcal{E}_{i,-}(z = 0) \end{pmatrix} = \begin{pmatrix} \mathcal{E}_{n,+}(z = \text{out}) \\ \mathcal{E}_{n,-}(z = \text{out}) \end{pmatrix}$$

6.3 Ellipticity Calibrator

The ellipticity calibrator contains a slab of ZnSe through which the laser beam passes prior to entering the detection system. It is the birefringence within this ZnSe slab caused by the placement of a weight which will introduce a complex Faraday angle into the beam. To determine the complex Faraday angle we first calculate the birefringence of the slab [33, 34]:

$$n_{\parallel} - n_{\perp} = -\frac{1}{2} n_0{}^3 (\pi_{11} - \pi_{12}) \sigma$$

where $n_{\parallel}$ and $n_{\perp}$ refer to the indices of refraction for the electric field parallel to and perpendicular to the compressive force, $n_0 = 2.4$ is the unstrained index, σ is the applied stress and is negative for compression, and $\pi_{11} = -1.44 \times 10^{-12}$ Pa and $\pi_{12} = 0.17 \times 10^{-12}$ are the piezo–optical coefficients measured at 6328Å which we will use for 10 microns since here we are only concerned with determining the sign of the Faraday angle.

For a 395 gram weight and a factor of 10 from the leverage arm the applied stress is:

$$\sigma = \frac{395 \text{ grams} \times 980 \text{ cm sec}^{-1}\ 10}{0.6 \times 2.54 \times 0.08 \times 2.54 \text{ cm}^2} = 1.25 \text{ E7 } \frac{\text{dynes}}{\text{cm}^2}$$

Therefore the birefringence caused by the placement of the weight is ~1.39E–5.

Using the multilayer formalism of Appendix 6.2 to include the effect of the etalon we will determine the effect which this birefringence will have upon the input polarization and, hence, the expected readings for data2ω and data3ω. The configuration is

$$\underset{\longrightarrow}{\text{air}} \mid \underset{\longleftrightarrow}{\text{ZnSe}} \mid \underset{\longrightarrow}{\text{air}}$$

Using the notation for the formalism of Appendix 6.2. the transmission matrix for this is

$$t = S_{\text{air, ZnSe}} \cdot U_{\text{ZnSe}} \cdot S_{\text{ZnSe, air}}$$

Therefore, the difference in $\Delta\phi$, the phase difference between the parallel and perpendicular polarizations, is

$$\Delta\phi = \mathrm{Arg}\left(\frac{1}{(t_{\parallel})_{2,2}}\right) - \mathrm{Arg}\left(\frac{1}{(t_{\perp})_{2,2}}\right)$$

This phase difference, which is plotted below against the effective slab thickness which results from rotating the calibrator about the axis of its mounting post . Figure 35 shows two dashed curves. The upper curve corresponds to the above birefringence value of $1.11\,E - 12\,\mathrm{cm}^2$ / dynes, while the bottom dashed curve corresponds to another, different, published result for the birefringence [35]. Figure 35 clearly shows that either value for $\Delta\phi$ has its maximum coincident with the transmission maximum which corresponds the solid curve.

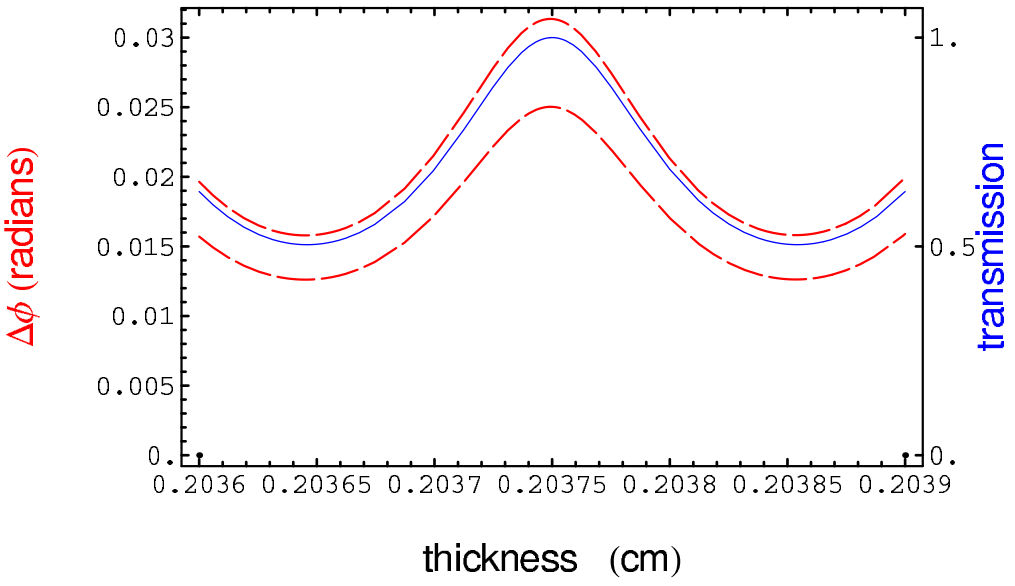

FIG. 35 The phase difference $\Delta\phi$ and field transmission coefficient versus slab thickness for ZnSe. The phase difference $\Delta\phi$ is shown as two red, dashed curves which result from two different reported values for the stress-optic coefficient. The field transmission coefficient resulting from the etalon effect is shown as the solid blue curve. Note that the peaks are essentially coincident.

The formalism of Appendix 6.2 can provide a calculated value for the Faraday angle produced by the placement of the weight of the calibrator. The matrix representation of the effect of the device is

$$\mathrm{LC}\cdot\mathrm{CRC}[\theta]\cdot\mathrm{CL}\cdot\begin{pmatrix} e^{i\Delta\phi} & 0 \\ 0 & 1 \end{pmatrix}\cdot\mathrm{LC}\cdot\mathrm{CRC}^{\dagger}[\theta]\cdot\mathrm{CL}\cdot\begin{pmatrix} x_{\mathrm{in}} \\ y_{\mathrm{in}} \end{pmatrix} = \begin{pmatrix} x_{\mathrm{out}} \\ y_{\mathrm{out}} \end{pmatrix}$$

where $\Delta\phi$ is the phase difference between the parallel and perpendicular polarizations as discussed above. Comparing the effect upon the beam for the weight both on and off the arm with the values calculated above establishes the sign to be applied to data3ω. This sign is in fact, determined to be negative for the arrangement of the current experiment. However, lack of agreement in the literature as to the stress–optic coefficient at present prevents its use for anything but determining the sign.

6.4 Signal Background

Measurements of the complex Faraday angle θ_F of a single wedged BaF substrate placed within the laser beam inside the magnet provide the background signal which must be removed from the total θ_F of the BSSCO/Baf combination. This background includes the effect of the ZnSe magnet windows as well as any other extraneous contributions arising from, for example, the mechanical distortion from induced magnetic dipole forces and hysteresis. Because all of the contributions to θ_F as well is θ_F itself are much less than 1, only a first order correction is required. This amounts to a direct subtraction from the BSSCO/BaF data.

The measurements of the background demonstrate no discernible temperature dependence nor any contribution to the imaginary Faraday angle θ_d. Figure 36 depicts the background contribution to the real Faraday angle θ_f versus the square of the laser frequency. The dots represent the actual data of which there are four points for each of three frequencies. The blue line is a fit to the data assuming only an intercept term and a frequency squared term:

$$\theta_f = -0.0000113525 + 1.05565 \times 10^{-10}\, \omega^2 . \tag{65}$$

This squared frequency dependence emerges from a perturbed solution [36] of the time-dependent Schrödinger equation for a crystal:

$$\theta_f \propto \sum_{k,k} \frac{|\Pi_{k',k}{}^{+}|^2 - |\Pi_{k',k}{}^{-}|^2}{\omega_{k',k}{}^2 - \omega^2} \tag{66}$$

where $\Pi_{k',k}{}^{\pm}$ are the momentum matrix elements for positive or negative helicity

$$\begin{aligned} \Pi_{k',k}{}^{i} &= \mathrm{m} V_{k',k}{}^{i} \left(= i m \omega_{k',k}\, r_{k',k}{}^{i} \right) \\ &= p_{k',k}{}^{i} + \frac{e}{c} A_{k',k}{}^{i} \end{aligned}$$

The lowest value for $\omega_{k',k}$ is the band gap energy which for BaF is ~9eV and for ZnSe is ~2.7eV. Because ω, the laser photon energy, is only 1/8 eV, the denominator of equation (66) can be expanded about ω. After rearranging the sum, only the ω^2 term survives.

The lack of a contribution to θ_d follows from the lack of free carriers and the large band gap of BaF as can be seen from the expression for the transverse conductivity [36]

$$\sigma_{xy} \propto \sum_{k,k} \frac{1}{\omega_{k',k}} [\, \Pi_{k',k}{}^{x}\, \Pi_{k',k}{}^{y}\, \delta(\omega + \omega_{k',k}) + \Pi_{k',k}{}^{y}\, \Pi_{k',k}{}^{x}\, \delta(\omega - \omega_{k',k})]. \tag{67}$$

The delta functions, even though broadened by mechanisms like scattering, essentially prohibit any transitions by the low energy photons of the laser.

From Fig. (36) the residual contributions manifest as a frequency independent term evident in the intercept of the ordinate axis.

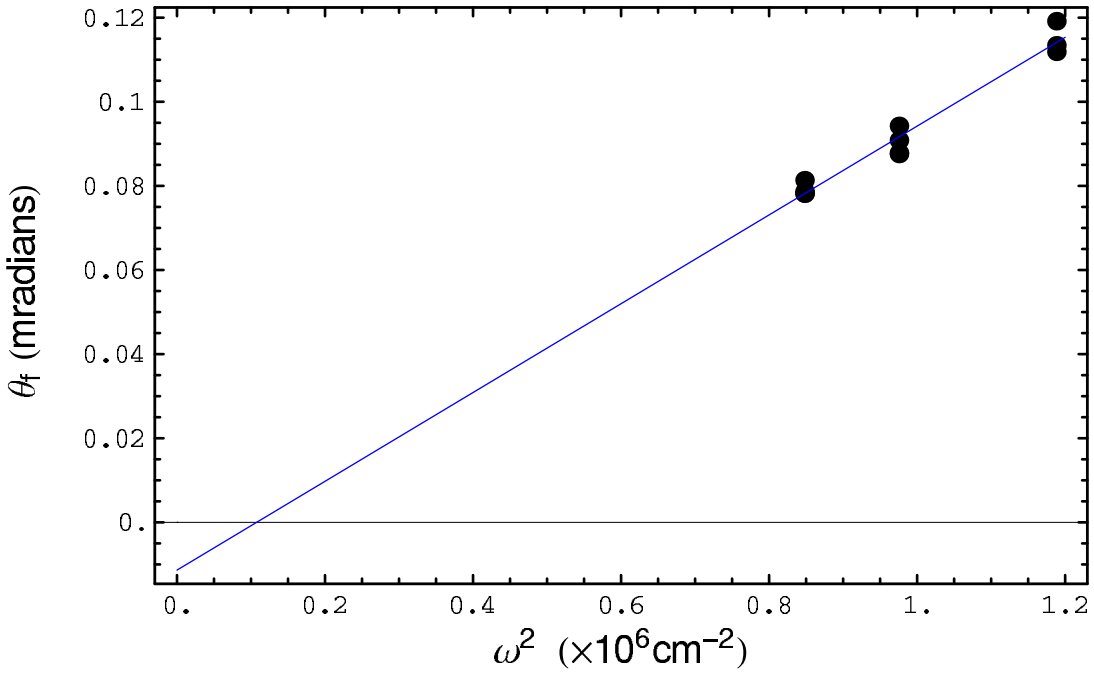

FIG. 36 The plot of the background contribution to θ_f. The dots represent data. There are actually four data points for each of the three frequencies above. The blue line is a fit to the data assuming only an intercept term and a frequency squared term.

The potential statistical error in the slope of equation (65) is $\pm 2\times 10^{-12}$ radians/cm^{-2}. This introduces a potential error to the frequency dependence of θ_f for BSCCO of

$$\frac{d\theta}{d\omega} = 2\omega \,\text{error}$$
$$= 4\times 10^{-9} \text{ radians/cm}^{-1}$$

which is not significant.

6.5 Resonant Drude in Magnetic Field

Below we shall derive the Hall response for a simple Lorentzian resonance but using a purely classical approach. We first desire an expression for the conductivity tensor, $\vec{\vec{\sigma}}$, defined as:

$$\vec{\vec{\sigma}}\,\vec{E} = \vec{J}$$
$$= \rho\,\vec{v} \qquad (68)$$

where E is the electric field

J is the current density

ρ is the charge density

and v is the velocity of a charge element.

To eliminate $\vec{v}$ we appeal to Newton's law with the Lorentz force and a restoring spring force, which creates the resonance:

$$q\vec{E} + \frac{q}{c}\vec{v}\times\vec{B} - \frac{m}{\tau}\vec{v} - k\,x = m\,\frac{d\vec{v}}{dt} \tag{69}$$

where q is the carrier charge

m is the carrier mass

τ is the mean time between collisions.

and k is the spring constant of the resonance.

Next, we assume a sinusoidal time dependency for everything.

$$x = x_0\, e^{-i\omega t}$$

$$v = -i\,\omega\, x_0\, e^{-i\omega t}$$

$$= -i\,\omega\, x$$

This, when enforced in equation 69, produces:

$$\vec{E} = -\frac{1}{c}\vec{v}\times\vec{B} + \frac{m}{\tau q}\vec{v} - \frac{m\,i\,\omega}{q}\vec{v} + \frac{k}{q}\vec{x}$$

or

$$E_i = \left[\frac{1}{c\,q\,n}\,\epsilon_{i\,j\,k}\,B_j + \delta_{ik}\left(\frac{m}{n\,q^2\,\tau} - \frac{i\,m\,\omega}{n\,q^2}\right)\right] n\,q\,v_k + \frac{k}{q}\,x_i$$

$$= \left[\frac{1}{c\,q\,n}\,\epsilon_{i\,j\,k}\,B_j + \delta_{ik}\left(\frac{m}{n\,q^2\,\tau} - \frac{i\,m\,\omega}{n\,q^2} + \frac{i\,k}{n\,q^2\,\omega}\right)\right] n\,q\,v_k$$

Comparison of equation 68 with 1 reveals:

$$\left[\frac{1}{c\,q\,n}\,\epsilon_{i,j,k}\,B_j + \delta_{ik}\left(\frac{m}{n\,q^2\,\tau} - \frac{i\,m\,\omega}{n\,q^2} + \frac{i\,k}{n\,q^2\,\omega}\right)\right] = (\overleftrightarrow{\sigma}^{-1})_{i,k}$$

or assuming that the B field is in the positive z direction then for cartesian coordinates:

$$(\overleftrightarrow{\sigma}^{-1})_{i,k} = \overleftrightarrow{\rho} = \frac{m}{n q^2}\begin{pmatrix} \frac{1}{\tau} - i\omega + \frac{ik}{m\omega} & -\omega_c \\ \omega_c & \frac{1}{\tau} - i\omega + \frac{ik}{m\omega} \end{pmatrix}$$

$$= \frac{m}{n q^2}\begin{pmatrix} \frac{1}{\tau} - i\omega + \frac{i}{\omega}\omega_0{}^2 & -\omega_c \\ \omega_c & \frac{1}{\tau} - i\omega + \frac{i}{\omega}\omega_0{}^2 \end{pmatrix}$$

where $\omega_c = qB/cm$ is the cyclotron frequency and $\omega_0 = \sqrt{k/m}$ is the frequency of the interposed resonance. Inverting the matrix produces the following expressions for the longitudinal and transverse conductivity

$$\sigma_{xx} = \sigma_{yy} = \frac{\omega_p{}^2}{4\pi} \frac{\omega\left(\frac{\omega}{\tau} - i(\omega^2 - \omega_0{}^2)\right)}{\left(\frac{\omega}{\tau} - i(\omega^2 - \omega_0{}^2)\right)^2 + \omega^2\,\omega_c{}^2} \tag{70}$$

and

$$\sigma_{xy} = -\sigma_{yx} = \frac{\omega_p{}^2}{4\pi} \frac{\omega^2\,\omega_c}{\left(\frac{\omega}{\tau} - i(\omega^2 - \omega_0{}^2)\right)^2 + \omega^2\,\omega_c{}^2}. \tag{71}$$

For a resonance at zero frequency and a cyclotron resonance smaller than the scattering rate these reduce to the equations of the standard Drude model:

$$\sigma_{xx} = \sigma_{yy} \approx \frac{\omega_p{}^2}{4\pi} \frac{1}{\frac{1}{\tau} - i\omega} \tag{72}$$

and

$$\sigma_{xy} = -\sigma_{yx} = \frac{\omega_p{}^2}{4\pi} \frac{\omega_c}{\left(\frac{1}{\tau} - i\omega\right)^2} \tag{73}$$

REFERENCES

[1] J. C. Bednorz and K. A. Müller, Z. Phys. B **64**, 189 (1986).

[2] M. Gurvitch and A. T. Fiory, Phys. Rev. Lett. **59**, 1337 (1987).

[3] S. Tajima *et al.*, Jpn. J. Appl. Phys. **26**, L432 (1987).

[4] J. Orenstein et al., Phys. Rev. B 36, 729 (1987)

[5] M. A. Quijada, Ph.D. thesis, University of Florida, 1994.

[6] J. J. Tu *et al.*, cond–mat/0104208 (unpublished)

[7] D. B. Romero et al, Phys. Rev. Lett. **69**, 1590 (1992).

[8] N. W. Ashcroft and N. D. Mermin, *Solid State Physics* (Ausnders College Publishing, USA, 1976), Chap. 17.

[9] E. H. Putley, *The Hall Effect and Related Phenomema*, (Butterwotrths, London, 1960).

[10] N. P. Ong, *et al.*, Phys. Rev. B **35**, 8807(1987).

[11] T. R. Chien, Z. Z. Wang, and N. P. Ong, Phys. Rev. Lett. **67**, 2088(1991).

[12] J. M. Harris, Y. F. Yan, and N.P. Ong, Phys. Rev, B **46**, 14293 (1992).

[13] Z. Konstantinovic, Z. Z. Li, and H. Raffy, Phys. Rev. B **62**, 11989(2000).

[14] S, G, Kaplan *et al.*, Phys. Rev. Lett. **76**, 696 (1996).

[15] J. Cerne *et al.*, Phys. Rev. Lett. **84**, 3418 (2000).

[16] J. Cerne *et al.*, Phys. Rev. B **61**, 8133 (2000).

[17] M. Grayson, L. B. Rigal, D. C. Schmadel, H. D. Drew, and P. J. Kung, cond–mat/0108553 (unpublished)

[18] C. M. Varma and Elihu Abrahms, Phys. Rev. Lett. **86**, 4652 (2001) and errata Phys. Rev. Lett. **88**, 39903 (2001)

[19] T. Valla *et al.*, Phys. Rev. Lett. **85**, 828 (2000).

[20] T. Valla *et al.*, Science **285**, 2110 (1999).

[21] P. V. Bodanov *et al.*, Phys. Rev. Lett. **85**, 2581 (2000).

[22] Z. X. Shen *et al.*, cond–mat/0108381(2001)(unpublished).

[23] P. W. Anderson, Phys. Rev. Lett. **67**, 2092 (1991).

[24] A.T. Zheleznyak, V. M. Yakovenko, and H. D. Drew, Phys. Rev. B **5**7, 3089 (1998)

[25] L. B. Ioffe and A. J. Millis, Phys. Rev. B **58**, 11631 (1998)

[26] from presentation at Augsberg by Matthias Opel, Walther–Meissner Institute for Low Temperature Reasearch of the Bavarian Academy of Sciences 2000

[27] R. Burdett, Perkin Elmer Instruments, 4/12/00Application Note 1003.

[28] Infrared conductivity data from measurments performed by J. J. Tu of the Department of Physics, Brookhaven National Laboratory, Upton, NY. This work was performed under support from the Department of Energy under contract number DE-AC02-98CH10886 (unpublished).

[29] E. Lange and G. Kotliar, Phys. Rev. Lett. **82**, 1317 (1999).

[30] A. J. Millis, Optical Conductivity and Correlated Electron Physics (unpublished)

[31] A. J. Millis, On the Relation between Angle Resolved Photoemission and Optical Conductivity (unpublished)

[32] H. D. Drew and P. Coleman, Phys. Rev. Lett. **78**, 1572 (1997).

[33] C. A. Klein (private communicaiton).

[34] J. F, Nye, *Physical Properties of Crystals* (Oxford Univeriversity Press, Oxford, Great Britain, 1979), Chap. XIII.

[35] A. Feldman, D. Horowitz, R. M. Waxler, and M. J. Sodge, NBS Technical Note 993 (U.S. GPO, Washington D.C., Feb. 1979).

[36] I. G. Mavroides, Optical Properties of Solids, edited by F. Abelés (North–Holland, Amsterdam, 1972).